INCORPORATING SEEPAGE PROCESSES INTO BANK STABILITY ANALYSES

By

MA. LIBRADA CHU-AGOR

Bachelor of Science in Civil Engineering
Western Institute of Technology
Iloilo City, Philippines
1989

Master of Arts in College Teaching (Civil Engineering)
University of Mindanao
Davao City, Philippines
1996

Master of Science in Hydrology and Water Resources
UNESCO-IHE Institute for Water Education
Delft, The Netherlands
2003

Submitted to the Faculty of the
Graduate College of the
Oklahoma State University
in partial fulfillment of
the requirements for
the Degree of
DOCTOR OF PHILOSOPHY
July, 2009

INCORPORATING SEEPAGE PROCESSES INTO

BANK STABILITY ANALYSES

Dissertation Approved:

Dr. Garey A. Fox

Dissertation Adviser

Dr. Glenn O. Brown

Dr. Rifat Bulut

Dr. Michael D. Smolen

Dr. A. Gordon Emslie

Dean of the Graduate College

ACKNOWLEDGMENTS

This scientific work was made possible by the selfless support and contribution of the following persons and institutions:

I am deeply indebted to my advisor Dr. Garey A. Fox for giving me the opportunity of lifetime in undertaking this research, for supervising me throughout the whole process, and for his patient but meticulous review of my writing making it a better piece of work every time. His support in both my personal and professional journey is invaluable.

Dr. Glenn V. Wilson was a great help in reviewing my papers and in sharing his knowledge and expertise in this study. The same goes to Dr. Andrew Simon and Dr. Eddy Langendoen of USDA-ARS in Oxford Mississippi.

I am grateful to Dr. Glenn Brown, Dr. Rifat Bulut, and Dr. Michael Smolen for serving as my committee and for critiquing my work. Dr. Brown and Dr. Bulut were most obliging in teaching us soil testing protocols.

I owe the soil and water research team of BAE-OSU a special thanks; Rachel Cancienne for helping me with the soil block experiments and for being an efficient lab partner, Onur Akay and John Fuchs for hauling our much needed soil for the experiments, and Amanda Fox for painstakingly reading and editing our papers.

Furthermore, I acknowledge the financial support of the Cooperative State Research, Education, and Extension Service, U.S. Department of Agriculture, National Research Initiative.

I also want to express my appreciation to the faculty and staff of Biosystems and Agricultural Engineering Department at OSU who have helped and supported me during my study. Mr. Wayne Kiner was very helpful in solving our laboratory malfunctions.

Finally, I am grateful to my family and friends for their moral support and for believing in me. Thank you to RA and RB for their love, understanding and sacrifices, and to Jorge for the patience, encouragement, unconditional love, and support.

Ma. Librada Chu-Agor
Oklahoma State University
Summer 2009

ABSTRACT

Streambank instability and failure have been widely known to result in increased sediment load to streams, loss of riparian properties and livelihood, and damage to hydraulic structures. One cause of streambank instability is seepage processes. Subsurface flow or seepage can cause instability and failure by reducing soil strength, exerting seepage forces, and creating seepage erosion undercutting at the point where water exists the bank. However, seepage driven erosion and failure have not been fully studied or modeled, despite its potential role in streambank instability.

Some of the complexity regarding seepage stems from the unavailability of seepage field measurements, the heterogeneity and variability of the porous media, the three-dimensional nature of the seepage erosion undercut, and the lack of understanding of the different bank failure mechanisms. In addition to this, discrete element models that can effectively simulate seepage particle mobilization, undercutting, and the corresponding mass wasting are unavailable and thus slope stability models do not include the dynamic effects of ground water or seepage in their analyses. This study incorporated seepage processes in bank stability analyses in an attempt to predict streambank failure. It is divided into four independent but interrelated sections:

- A procedure for incorporating seepage erosion undercutting into bank stability models was developed to address the question of whether seepage particle mobilization can lead to distances of undercutting that are a significant cause of bank instability. A numerical finite element model, SEEP/W, and a general limit

equilibrium bank stability model, SLOPE/W, were used to simulate flow and stability, respectively, of a two-dimensional prototype streambank. Results showed that stability decreased between 42 and 91% as the depth of undercutting increased, dependent upon the initial stability of the bank. The probability of failure reached 100% when the depth of the undercutting reached approximately 30 to 50 mm under the two-dimensional lysimeter conditions.

- The hydraulic conditions producing seepage failure mechanisms were investigated using a three-dimensional soil box. A 25-cm tall, 50-cm wide, and 20-cm long soil block with a focused inflow reservoir was constructed to investigate seepage gradient forces and the three-dimensional nature of seepage particle mobilization (i.e., seepage erosion) and undercutting. Two soils were used in the experiments (sand and loamy sand) packed in the block at different bulk densities (1.30 to 1.70 Mg m^{-3}) and with an outflow face at various angles (90, 75, and 60 degrees). Constant heads of 15 cm, 25 cm, and 35 cm were imposed on the soil to induce flow. Seepage erosion undercutting was monitored in time using a three-dimensional digital laser scanner. The bulk density of the two different soil types controlled which seepage failure mechanism occurred: (1) tension or "pop-out" failures due to the seepage force exceeding the soil shear strength, (2) particle mobilization and undercutting when the initial seepage force gradient was less than the resistance of the soil block. For cases experiencing particle mobilization and undercutting, seepage erosion initiated as unimodal (i.e., concentrated at one point) or as multimodal (i.e., initiating at several locations across the bank face), and this result was largely controlled by the bank angle.

The shape of the seepage undercut can be represented by a five parameter Gaussian function. This function can be used to predict the dimensions of the seepage erosion undercut.

- An empirical sediment transport function that can predict seepage erosion and undercutting with time was developed based on the three-dimensional soil block experiments covering a wide range of hydraulic, soil type, slope and bulk density combinations. The transport function was represented by an excess gradient equation (R^2 = 0.54), where the critical gradient was predicted by the soil cohesion based on laboratory experiments. The geometric relationships between the maximum distance and lateral and vertical dimensions of the undercut were then derived using a three-dimensional Gaussian function. The proposed empirical relationships were able to predict the observed time at which a given amount of undercut developed (R^2 = 0.79). Using the flow gradient and the seepage layer's cohesion, the proposed sediment transport function can predict the dimension of the seepage erosion undercut. These dimensions can then be used to predict the impact of seepage erosion undercutting on streambank stability.
- Seepage processes (i.e., seepage gradient forces and seepage erosion undercutting) were incorporated into the Bank Stability and Toe Erosion Model (BSTEM) and their importance on bank stability was evaluated. The effects of the seepage force were incorporated into BSTEM by modifying the force balance. Seepage erosion undercutting was simulated using a recently proposed sediment transport function. The modified BSTEM was then used to evaluate the stability of a streambank along Little Topashaw Creek under different scenarios: (1)

without seepage forces and undercutting, (2) with seepage forces only, (3) with seepage undercutting only, and (4) with both seepage forces and undercutting. Stability was evaluated by computing the factor of safety, *FS*. For a condition where the bank was fully saturated, the FS decreased by as much as 66% from that of a dry condition due to the decrease in the frictional strength of the soil as the pore-water pressure increased. Incorporating the effects of the seepage force resulted in an average decrease in *FS* of approximately 30 to 50% for all water table depths. Seepage erosion undercutting reduced the FS by approximately 6% for a 5 cm undercut (i.e., 2% of *BH*) and 11% for a 10 cm undercut (i.e., 3.3% of *BH*) due to the loss of supporting material in the conductive layer. Seepage erosion undercutting required 15 to 20 cm of seepage undercut to become the dominant failure mechanism over seepage forces and pore-water pressure effects. The cumulative effects of seepage reduced this streambank's *FS* by up to 63% when the water table reached the entire bank height.

Incorporating seepage processes in bank stability analyses was necessary in order to better understand site-specific failure mechanisms. The results of this study are indispensable when assessing the stability of streambanks for design purposes (hydraulic structures), river restoration, and sediment transport studies. Primary research remaining to be investigated include investigating the link between fluvial erosion and seepage processes, improving the proposed sediment transport function, and evaluating the effect of seepage on soil cohesion.

TABLE OF CONTENTS

ACKNOWLEDGMENTS III

ABSTRACT V

LIST OF TABLES XI

LIST OF FIGURES XIII

CHAPTER 1 1

Numerical Modeling of Bank Instability by Seepage Erosion Undercutting of Layered Streambank 1

1.1 Abstract 1

1.2 Introduction 2

1.3 Materials and Methods 7

1.4 Results and Discussion 18

1.5 Summary and Conclusions 32

CHAPTER 2 35

Seepage Caused Tension Failures and Erosion Undercutting of Hillslopes 35

2.1 Abstract 35

2.2 Introduction 36

2.3 Materials and Methods 40

2.4 Results and Discussion 51

2.5 Summary and Conclusions 67

CHAPTER 3 70
Sediment Transport Function Predicting Seepage Erosion Undercutting for Bank Failure Prediction 70
3.1 Abstract 70
3.2 Introduction 71
3.3 Materials and Methods 80
3.4 Results and Discussion 91
3.5 Summary and Conclusions 99
CHAPTER 4 101
Incorporating Seepage Processes to Streambank Stability Model 101
4.1 Abstract 101
4.2 Introduction 102
4.3 Materials and Methods 105
4.4 Results and Discussion 112
4.5 Summary and conclusion 117
CHAPTER 5 119
Summary and Conclusion of Dissertation 119
5.1 Specific Conclusions in Regard to Each Dissertation Chapter 120
5.2 Future Research 125
CHAPTER 6 126
References 126

LIST OF TABLES

Table 1.1 Boundary conditions for the two-dimensional seepage erosion lysimeter experiments simulated using SEEP/W and SLOPE/W..... 8

Table 1.2 Soil strength parameters of Little Topashaw Creek (LTC) streambank based on measurements at two sites where seepage erosion was observed. Values for cohesion and angle of internal friction are average values used in the SLOPE/W model. Parameter values in parentheses are values from each site..... 15

Table 1.3 Field measured hydraulic conductivity, K_s, and soil-water retention parameters of Little Topashaw Creek streambank sediment and comparison to calibrated LS layer K_s, for lysimeter experiments; SEEP/W model was most sensitive to this parameter, therefore all other parameters were not part of model calibration. 20

Table 1.4 Root mean square error (RMSE) of measured and SEEP/W simulated soil-water pressure for tensiometers in each lysimeter experiment before calibration and after calibration on K_s of LS layer. 21

Table 1.5 Regression between measured and SEEP/W simulated cumulative discharge in each lysimeter experiment prior to calibration and after calibration on K_s of LS layer. 22

Table 1.6 Comparison of observed versus SLOPE/W predicted volume of bank collapse. 26

Table 2.1 Particle size distribution and mean particle size (d_{50}, mm) for the two soils used in the soil block experiments..... 51

Table 2.2 Soil water retention curves estimated using RETC based on pressure plate experiments for the sand and loamy sand soils at the bulk densities used in the soil block experiments..... 52

Table 2.3 Saturated hydraulic conductivity (K_s) measured using constant-head permeameter test for varying bulk densities of the sand and loamy sand soils..... 52

Table 2.4 Geotechnical properties (effective cohesion, and internal angle of friction) of the sand and loamy sand soils. 53

Table 2.5 Observed seepage erosion volume (V_{SE}), volume (V_{BF}) of soil loss by bank failure, and depth or maximum distance of undercutting (d_u) prior to bank collapse, relative to experimental soil block conditions (α' = bank angle, H = inflow water reservoir head, and ρ_b = soil bulk density). 54

Table 2.6 Factor of safety (FS) for the sand (S) and loamy sand (LS) banks computed at two different locations in the flow domain. Close to the inlet, the seepage vector is directed at $90 \leq \lambda \leq 180$ and the valid failure plane is *y-y* (see Figure 2.4). 61

Table 3.1 Geotechnical properties (effective cohesion, c', and internal angle of friction, ϕ') and critical gradient (i_{cr}) necessary to propagate an undercut of the two soils used in the laboratory soil column experiments. 84

Table 3.2 Soil, hydrologic, and bank characteristics of function development data sets (i.e., approximately two-thirds of the soil block experiments). 88

Table 3.3 Soil, hydrologic, and bank characteristics of function evaluation data sets (i.e., approximately one-third of the soil block experiments). 89

Table 4.1 Soil hydraulic properties of LTC (after Wilson et al., 2007)..... 112

LIST OF FIGURES

Figure 1.1 Example of seepage erosion particle mobilization and undercutting on the Little Topashaw Creek streambank in northern Mississippi 6

Figure 1.2 Lysimeter set-up showing the location of the tensiometers and the hydraulic controls of the experiment 8

Figure 1.3 Examples of undercutting by seepage particle mobilization, tension crack formation, and bank collapse observed during the lysimeter experiments. 9

Figure 1.4 Free-body diagram of a vertical slice within a potential sliding mass and definition of the critical variables. 12

Figure 1.5 (a) Change in the geometry in the SLOPE/W modeling of the loamy sand (LS) layer experiencing undercutting by seepage erosion and (b) null region used in place of the seepage undercut in the SLOPE/W model. Figures shown are for experiment with H = 0.6 m, BH = 0.8 m, and S = 0%. 17

Figure 1.6 Observed versus SEEP/W predicted cumulative discharge for six lysimeter experiments after calibration on K_s. and soil-water retention parameters (θ_s, a, and n) were not calibrated for other soil layers. 19

Figure 1.7 Mean factor of safety (Fs) versus time as predicted by SLOPE/W Monte Carlo analysis for lysimeter experiments (a) without considering seepage undercutting and (b) with seepage undercutting. 24

Figure 1.8 Simulated probability of failure (PF, %) of lysimeter experiments with BH = 0.8 m, S = 0%, and (a) H = 0.3 m, and (b) H = 0.6 m with and without seepage undercutting. 25

Figure 1.9 Comparison of the actual bank collapse (solid line) and the SLOPE/W predicted critical slip surface (dotted line) generated for the constant head, *H* = 0.3 m, bank height, *BH* = 0.8 m, and slope, *S* = 0%, lysimeter experiment. The observed bank collapse was 0.12 m^3 while the SLOPE/W predicted bank collapse was 0.14 m^3. Note that the inflow reservoir is on the opposite side to that indicated in Figures 1.2 and 1.5 27

Figure 1.10 Factor of safety (*Fs*) versus depth of undercutting for two experiments with same bank height (*BH* = 0.8 m) and slope (*S* = 0%) but different constant heads (*H* = 0.3 m and 0.6 m). Error bars represent minimum and maximum *Fs* from 2000 Monte Carlo simulations 28

Figure 1.11 Factor of safety (*Fs*) versus depth of undercutting for two experiments with same constant head (*H* = 0.3 m) and slope (S = 0%) but different bank heights (*BH* = 0.4 m and 0.8 m). Error bars represent minimum and maximum Fs from 2000 Monte Carlo simulations. 29

Figure 1.12 Factor of safety (*Fs*) versus depth of undercutting for experiments with same constant head (*H* = 0.6 m) and (a) same bank height (*BH* = 0.8 m) but different slopes (*S* = 0 and 10%) and (b) same bank height (*BH* = 0.5 m) but different slopes (*S* = 5 and 10%). Error bars represent minimum and maximum *Fs* from 2000 Monte Carlo simulations. 31

Figure 1.13 Depth of undercutting, *d*, versus mean factor of safety, *Fs*, of all six lysimeter experiments modeled with SLOPE/W. 32

Figure 2.1 Three-dimensional soil block used to simulate seepage instability of single-layer, repacked soil banks. The inflow reservoir is capable of producing seepage heads up to 100 cm. 42

Figure 2.2 Example of the eroded surface by seepage particle mobilization captured using the three-dimensional laser scanner. Each scan represents a different time during the experiment: (a) original bank face, (b) and (c) illustrate the start of the seepage particle mobilization and undercutting, (d) and (e) illustrate continued undercut growth, and (f) illustrates the bank after small-scale sapping failure on the bank slope. 43

Figure 2.3 Seepage vectors as simulated by SEEP/W for a 90 degree sand bank with an inflow reservoir head of 15 cm and a bulk density, ρ_b, of 1.30 Mg m^{-3}. 45

Figure 2.4 Free-body diagram of a soil element subjected to seepage gradient forces considering two possible failure planes, *yy* and *xx*. *W* is the weight of the soil element; σ' is the effective normal force; τ is the shear stress; f_s is the seepage force on the element; α' the bank angle; λ is the direction of the seepage vector measured clockwise from the inward normal to the bank slope; *z* is the width of the failure block; and *b* is the height of the failure block. 46

Figure 2.5 Relationship between maximum depth of undercutting, d_u, required for a bank failure and the bulk density (ρ_b) nondimensionalized by the particle density (ρ_s) of the soil. The symbols represent the averages relative to varying bank slope and water head for each soil type. 56

Figure 2.6 Typical time sequence of seepage erosion undercut formation. Note that the *x*-*y* plane is the bank face. Example shown is for the case of a 90 degree sand bank, 35 cm water head with ρ_b = 1.60 Mg m^{-3}. (a) t = 108 s after flow arrival, (b) Gaussian fit for t = 108 s (R^2 = 0.80), (c) t = 125 s after flow arrival, (d) Gaussian fit for t = 125 s (R^2 = 0.77), (e) t = 149 s after flow arrival, and (f) Gaussian fit for t = 149 s (R^2 = 0.78). 63

Figure 2.7 Example of (a) unimodal and (b) multimodal seepage erosion undercuts. Note that the x-y plane is the bank face. The unimodal figure is for the case of loamy sand with 90 degree bank, 35 cm head, and 1.60 Mg m^{-3} bulk density. The bimodal figure is for the loamy sand with 75 degree bank, 15 cm head, and 1.70 Mg m^{-3} bulk density. 64

Figure 2.8 Time required for multimodal seepage particle mobilization undercuts for (a) sand and (b) loamy sand soils to reach unimodal undercut, nondimensionalized by the saturated hydraulic conductivity, K_s, and the water inflow reservoir head, *H*. 65

Figure 2.9 Observed relationship between the depth (d_u) of the undercut and the (a) height as quantified by the spread (i.e., σ_y) and (b) width of the undercut (σ_x) for the sand and loamy sand soils. Note that the regression lines shown for σ_x versus d_u are for d_u less than 4 cm. 66

Figure 3.1 Photograph of a seepage erosion undercut on a streambank face along Goodwin Creek in northern Mississippi. This seepage

erosion undercut is one of the largest undercuts observed during field experiments reported by Fox et al. (2007) and Wilson et al. (2007). 72

Figure 3.2 Force balance on a particle on a bank inclined at an angle α'. The particle makes an angle β with another particle and is subjected to a seepage force (*Fs*) exiting the bank at an angle ψ, a tractive force due to surface runoff (*Fw*), and gravity (*Fg*) (after Howard and McLane, 1988). 75

Figure 3.3 Free-body diagram of a soil element subjected to seepage force considering two possible failure planes, *yy* and *xx*. The soil element has dimensions *z* and *b* and is subjected to seepage (f_s) and gravity (*W*) forces. 78

Figure 3.4 Three-dimensional soil block set-up used to simulate seepage erosion of single-layer, repacked soil banks. 81

Figure 3.5 Scanned image of the bank face of the three-dimensional soil block at different times during an experiment. Images shown are for a 90-degree sand bank, 15 cm water head with ρ_b = 1.60 Mg m^{-3}. 83

Figure 3.6 Dimensions of the undercut: the maximum undercut distance, d_u, the height at the bank face, h_{bf}, and the width at the bank face, w_{bf}. The h_{bf} and w_{bf} are functions of the vertical and horizontal spreads (σ_y and σ_x), respectively. 83

Figure 3.7 Initiation of seepage undercutting for sand at ρ_b = 1.6 Mg m^{-3} with an imposed gradient of 0.30. The imposed gradient was capable of propagating an undercut. 87

Figure 3.8 Relationship between the critical gradient, i_{cr}, and effective cohesion, *c'*. The critical gradient was computed by dividing the critical head, H_{cr}, which was measured in the laboratory, by the length of the soil block. This relationship applies to sand and loamy sand at different bulk densities. 92

Figure 3.9 Relationship between seepage erosion rate (E_{rs}) and excess gradient (i-i_{cr}) using data from function development studies consisting of data from both soil types (coarse sand and loamy sand) and across a range of several different bulk densities (1.3 to 1.7 Mg m^{-3}), heads (15 to 35 cm), and bank angles (60 to 90 degrees). The inner band is the 95% confidence interval while the outer band is the 95% prediction interval. 93

Figure 3.10 Relationship between seepage erosion maximum distance of undercut, d_u, and volume per unit area (V_u/A_u) using data from function development studies consisting of data from both soil types (coarse sand and loamy sand) and across a range of several different bulk densities (1.3 to 1.7 Mg m^{-3}), heads (15 to 35 cm), and bank angles (60 to 90 degrees). 95

Figure 3.11 Linear regression between predicted time (t_p) and observed time (t_{obs}) calculated using the seepage erosion sediment transport function and geometrical undercut relationships to obtain the observed maximum distance of undercut (d_u) for the function evaluation studies..... 96

Figure 3.12 Observed relationship between the maximum distance (d_u) of the undercut and the height as quantified by the spread (σ_y) for the sand and loamy sand soils within the function development data sets. 97

Figure 3.13 Linear regression analysis between the measured and computed undercut height (h_{bf}) for the function evaluation data set. 98

Figure 4.1 Streambank seepage and erosion due to infiltrating water (after Fox et al., 2006) and example of seepage erosion undercutting along Goodwin Creek in northern Mississippi. 103

Figure 4.2 Free body diagram of the failure plane in the modified BSTEM. The forces (and their components) acting on the failure mass are: (1) the weight of the soil mass, *W*, (2) the confining pressure, *P*, (3) the pore-water pressure, *U*, (4) the soil shear strength, τ, and (5) the seepage force, *SF* at an angle γ with the horizontal. Angles β and α' are the shear plane and bank angles, respectively. 106

Figure 4.3 Example of the seepage erosion rate, E_{rs}, distributed in time, *t*. For example, if a user was interested in determining stability between $t = 0$ and $t = t_6$, the cumulative positive E_{rs} between $t = 0$ and $t = t_6$ (shaded area) would be used to determine the total eroded mass, *M*. 109

Figure 4.4 Bank profile of LTC used in SEEP/W. The domain was divided into 0.10 m^2 finite elements. A constant head was maintained at the left boundary and free drainage at the bank face (right boundary). No confining pressure from the stream was considered. 111

Figure 4.5 Factor of safety, *FS*, with and without the seepage force, *SF*, and the corresponding decrease in *FS*. Percentages inside the circle are the decrease in *FS* due the rise in the water table elevation without

SF. Percentages inside the rectangle are the decrease in *FS* due to the rise in the water table elevation with *SF*. No seepage erosion undercutting, *SE*, was considered. 113

Figure 4.6 Factor of safety, *FS*, due to seepage erosion, *SE*. The presence of the seepage undercut did not affect the decrease in *FS* due to the rise of the water table elevation. No seepage force, *SF*, was considered 116

Figure 4.7 Factor of safety, *FS*, due to seepage erosion, *SE* and seepage force *SF*. Percentages inside the rectangle are the decrease in *FS* due to the rise in the water table elevation with both *SE* and *SF*. 117

CHAPTER 1

Numerical Modeling of Bank Instability by Seepage Erosion Undercutting of Layered Streambank[1]

1.1 ABSTRACT

Undercutting, primarily considered due to fluvial mechanisms, has been reported to have a major impact on slope failure. Predicting bank collapse specifically due to seepage erosion undercutting by particle mobilization on layered streambanks has not been fully studied or modeled, even though its role in streambank erosion may be important. The limitation originates from limited field measurements and laboratory experiments, as well as the unavailability of discrete element models that can effectively simulate seepage particle mobilization, undercutting, and the corresponding mass wasting. The objective of this research was to demonstrate a procedure for incorporating seepage undercutting into bank stability models and to investigate the role of seepage undercutting on bank instability. The specific question to be addressed is whether seepage particle mobilization can lead to distances of undercutting that are a significant cause of bank instability. A numerical finite element model, SEEP/W, was used to model soil-water pressure variations during seepage observed in laboratory experiments with two-dimensional soil lysimeters. Flow parameters were calibrated using measured soil-

[1] Published in *Journal of Hydrologic Engineering*, 2008
Chu-Agor, M.L., G.V. Wilson, G.A. Fox, 2008. Numerical Modeling of Bank Instability by Seepage Erosion. *J. Hydrol. Eng.* 13(12), 1133-1145

water pressure and cumulative discharge. A general limit equilibrium bank stability model (SLOPE/W) was used to simulate bank stability with and without seepage erosion undercutting by comparing the computed factor of safety, *Fs*, at different stages of the seepage erosion process with regard to input parameter uncertainty using Monte Carlo analysis. The percentage decrease in the mean *Fs* ranged between 42 and 91% as the depth of undercutting increased, dependent upon the initial stability of the bank. A stable bank (i.e., $Fs>1$) can quickly become unstable (i.e., $Fs<1$) when seepage undercutting is considered. For stable banks, the probability of failure reached 100% when the depth of the undercutting reached approximately 30 to 50 mm under these experimental conditions. The results derived are specific to the streambank simulated but are expected to be comparable for similar layered streambank lithologies reported to occur in numerous geographical locations. This research also highlights the need to incorporate the dynamic process of seepage erosion undercutting into integrated subsurface flow and streambank stability models.

1.2 INTRODUCTION

Streambanks are one of the most vulnerable geologic structures on earth. Riverbank erosion and associated sedimentation and land loss hazards are a resource management problem of global significance (Darby et al., 2000). Issues such as streambank stability and sediment load to streams have been major concerns for decades and billions of dollars have been spent on streambank protection and restoration. Aside from being one of the major sources of fine sediment loads to streams (i.e., 75.9 m^3 annual yield in the Bush River, UK which drains an area of 340 km^2 and runs a distance of 60 km as reported by Evans et al., 2006), bank erosion and deposition processes lie at

the center of understanding fluvial geomorphological processes (Lawler, 2005). Bank erosion is one of the fundamental processes involved in channel migration and formation of flood plains (Hooke, 1979). This is because the most important mechanisms in fluvial geomorphology are the hydraulic forces exerted by the flow (Hardy, 2006).

The erosion of sediment from streambanks can be overwhelmingly dominated by mass wasting (Simon and Darby, 1997). Subsurface erosion is often regarded as a process of limited importance confined to certain soils and streambank stratigraphies (Bryan and Jones, 1997). The effect of seepage or subsurface flow is usually considered to be limited to the production of surface runoff and the reduction of the soil shear strength, thereby underestimating the potential effects of seepage on erosion (Owoputi and Stolte, 2001). Due to the lack of knowledge and the general opinion that seepage effects are small, especially compared to other processes and forces involved, seepage effects are generally neglected in stream channel designs (Burgi and Karaki, 1971). The significance of seepage erosion has not been widely recognized or understood despite the documentation of its occurrence in numerous geographical locations (Hagerty, 1991; Wilson et al., 2007; Fox et al., 2007).

It is widely recognized that seepage reduces the cohesive strength and thus the bank stability by increasing soil-water pressure (Abam, 1993; Darby and Thorne, 1996; Crosta and Prisco, 1999; Rinaldi and Casagli, 1999; Simon et al., 1999). Burgi and Karaki (1971) developed an empirical relationship between the seepage forces acting on the side slope of a channel and the stability of the channel with various flow conditions. They confirmed that side slopes with seepage were less stable than channels without seepage. Crosta and di Prisco (1999) studied seepage erosion causing liquefaction and

rapid slope failures by comparing observed field failure mechanisms and the evolution of the saturated domain using a numerical model. They reported that failure was induced by the three dimensional development of the saturated domain from a localized source. Hagerty et al. (1981) investigated bank erosion in the Ohio River and concluded that one of the principal erosion mechanisms is internal erosion of bank materials by discharge following floods. Kusakabe et al. (1987) carried out a series of centrifuge model tests to study river bank failures due to seepage flow and found that clay and silt content of river bank material have significant effect on the importance of seepage flow. Dapporto et al. (2003) investigated the mechanisms of failure and retreat of Arno River in Italy using numerical models to predict changes in soil-water pressure and to analyze the stability of the banks due to variation in the river stage. They demonstrated that the complex interaction between soil-water pressure and the stabilizing confining pressures of river stage plays the primary role in triggering mass failures. However, none of these studies included particle mobilization and undercutting of banks due to seepage erosion.

According to Rockwell (2002), the greatest weakness of both seepage and soil-water pressure studies has been the lack of direct, local and precise instrumentation. Quantitative data are not available at the point of erosion, and quantitative existence of seepage is only known indirectly. This limitation could be due to the difficulty of conducting field studies during wet periods when seepage is active (Huang and Laflen, 1996; Wilson et al. 2007). Study of failure due to seepage flow requires accumulated data of close observations on the phenomena in the field as well as laboratory reproduction of these phenomena. This is necessary to understand such physical events and deduce

physical models and analytical methods to predict the risk of failure (Kusakabe et al., 1987).

A few studies in the literature have begun to study seepage erosion in the laboratory and field with the detail suggested by Rockwell (2002). Lourenco et al. (2006) examined the relation between soil-water pressure and the failure mode at the interface of two soil layers of different permeability. Although their experiments did not show any clear relation between soil-water pressure and the failure mode, it demonstrated that seepage strongly controlled the failure mechanisms. Fox et al. (2006) and Wilson et al. (2007) conducted lysimeter experiments of the undercutting of streambanks by seepage flow indicating that seepage undercutting, independent of the loss of negative soil-water pressure, could result in bank collapse. Wilson et al. (2007) documented the first in-situ detailed measurements of seepage flow, erosion, and bank undercutting and demonstrated that streambank stratigraphy and layering were important factors of seepage erosion (Figure 1.1). Fox et al. (2007) demonstrated that undercutting occurs not only due to seepage through a conductive, noncohesive streambank layer as observed by Wilson et al. (2007), but can also occur when seepage erosion undercuts less cohesive layers underneath the conductive layer.

While studies quantifying the effects of seepage erosion on bank stability are improving, bank stability analysis has not been developed to address the effects of bank undercutting brought about by seepage erosion particle mobilization. Seepage forces have been incorporated into slope stability analyses for homogenous, isotropic banks to predict cantilever or “pop-out” failures (Budhu and Gobin, 1996), but no slope stability analyses have attempted to incorporate particle mobilization by seepage gradients leading

to undercutting on layered bank profiles. Few, if any, studies on seepage have attempted to incorporate bank instability by the combined forces of increased soil-water pressure and seepage undercutting. Wilson et al. (2007) acknowledged the need to incorporate a subsurface flow model with a streambank stability model and suggested that the dynamic process of seepage erosion and undercutting needs to be included in the combined models. Undercutting, primarily considered at this time due to fluvial mechanisms, has been reported as a major impact on slope failure. What is not known is whether seepage undercutting can lead to distances of undercutting that are a significant cause of instability. This research attempts to answer this question for these experimental conditions to determine if future work should be aimed at incorporating this instability mechanism into streambank stability models.

Figure 1.1 Example of seepage erosion particle mobilization and undercutting on the Little Topashaw Creek streambank in northern Mississippi

The objective of this research was to develop a procedure that will quantify the effects of seepage undercutting on bank stability. The two-dimensional lysimeter

experiments of Fox et al. (2006) and Wilson et al. (2007) were simulated using a variably saturated flow model integrated with a geotechnical bank stability model. The variably saturated flow model was calibrated based on measured cumulative discharge and soil pore-water pressure. Field measured geotechnical parameters were used without calibration as estimates of lysimeter parameters in the bank stability model. Seepage erosion was simulated by manually changing the geometry of the LS layer based on available data for the dimensions and shape of the undercutting. Therefore, a priori information on undercutting was used in the model (i.e., no particle dynamics model was used to estimate the headcut formation). This research evaluates bank stability driven by dynamic changes in the streambank face geometry due to seepage undercutting. Undercutting by seepage particle mobilization is analogous to gully erosion processes in that headcuts cause headward migration of internal gullies from the bank face.

1.3 MATERIALS AND METHODS

1.3.1 Lysimeter Experiments

Fourteen lysimeter experiments (1.0 m long, 0.15 m wide and either 0.5 m or 1.0 m tall) were performed by Fox et al. (2006) and Wilson et al. (2007) to simulate seepage erosion at Little Topashaw Creek (LTC) in northern Mississippi. The simulated LTC streambanks consisted of a silt loam (SiL) top soil of varying bank height, a 0.10 m conductive loamy sand (LS) layer, and a 0.05 m clay loam (CL) restrictive layer at the bottom (Figure 1.2). Flow through the lysimeter was controlled using constant heads of 0.3 and 0.6 m. The base of the lysimeter was tilted to simulate banks with 0%, 5%, and 10% slopes. Of the 14 lysimeter experiments perfomed, six were selected so that the modeling included various bank heights (*BH*), heads in the water inflow reservoir (*H*),

and bank slope (*S*): *BH* from 0.3 to 0.8 m, *H* from 0.3 to 0.6 m, and *S* from 0 to 10% (Table 1.1). The simulations also included an experiment where bank failure did not occur despite significant seepage undercutting (*H* = 0.3 m, *BH* = 0.4 m, and *S* = 0%).

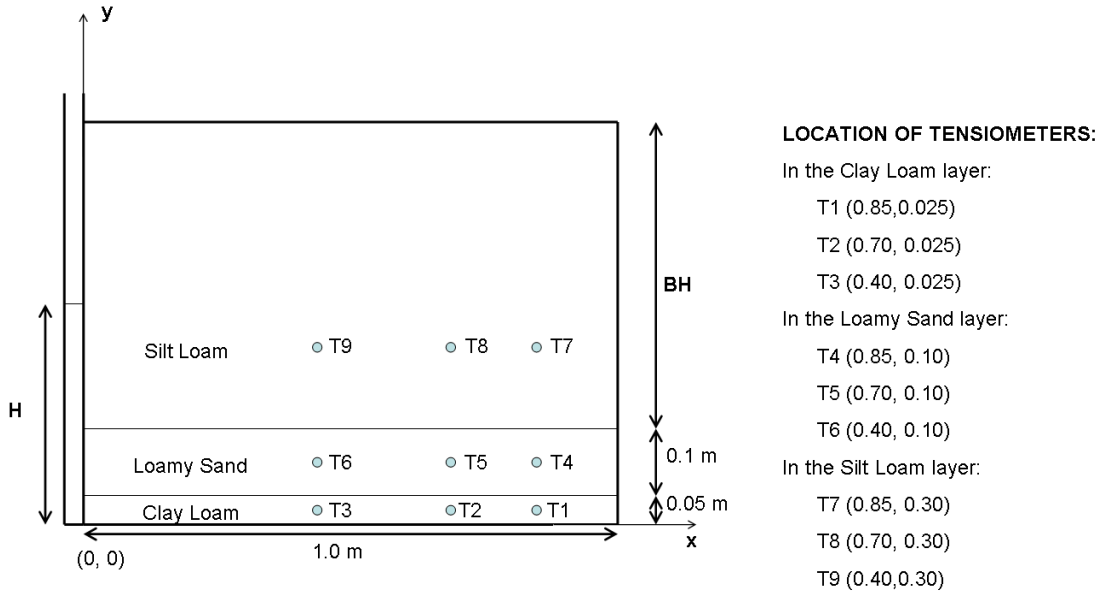

Figure 1.2 Lysimeter set-up showing the location of the tensiometers and the hydraulic controls of the experiment

Table 1.1 Boundary conditions for the two-dimensional seepage erosion lysimeter experiments simulated using SEEP/W and SLOPE/W.

H (m)	*BH* (m)	*S* (%)
0.3	0.4	0
0.3	0.8	0
0.6	0.8	0
0.6	0.5	5
0.6	0.5	10
0.6	0.8	10

Data from the lysimeter experiments included soil-water pressure measured by nine tensiometers (Figure 1.2) within the three streambank layers and cumulative

discharge measurements at specific times (Periketi, 2005; Wilson et al., 2007). During the lysimeter experiments, the depth of seepage undercutting, referred to as the horizontal distance from the drainage face of the lysimeter into the bank, was measured. These measurements were used to simulate seepage undercutting in the bank stability model. Examples of the undercutting by seepage particle mobilization and resulting bank collapses are shown in Figure 1.3.

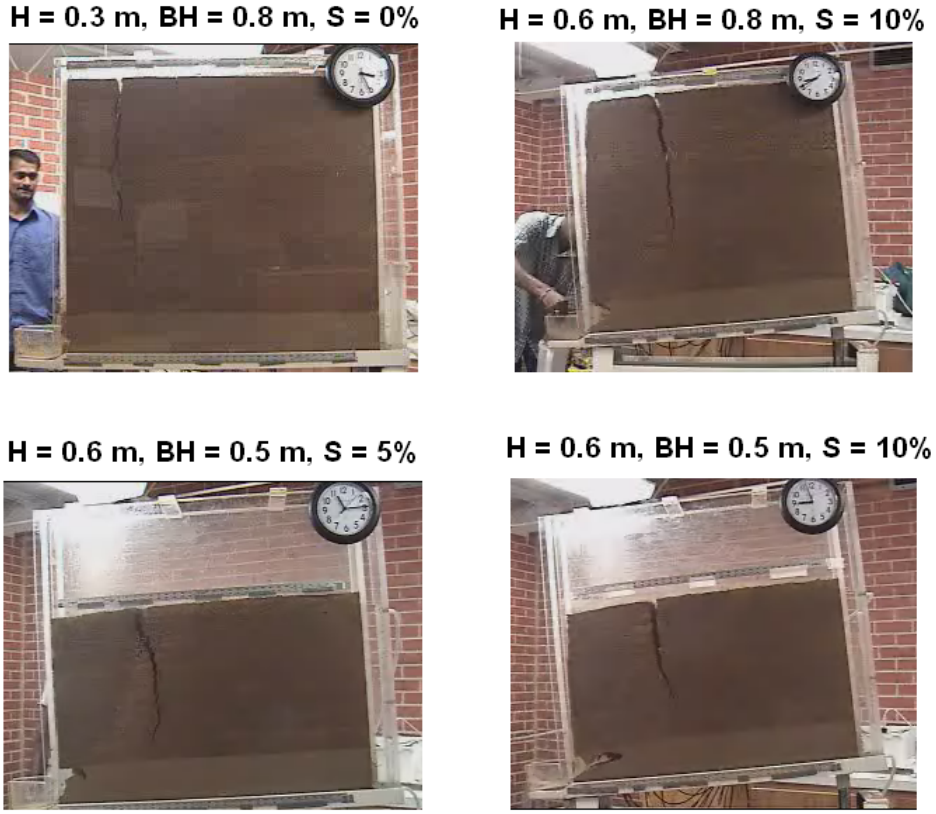

Figure 1.3 Examples of undercutting by seepage particle mobilization, tension crack formation, and bank collapse observed during the lysimeter experiments.

1.3.2 Variably Saturated Flow Modeling

The lysimeter experiment was modeled using SEEP/W to simulate the variations in the soil-water pressure and cumulative discharge. SEEP/W is a finite element model of Richards' equation for two-dimensional variably saturated flow (Krahn, 2004a). The flow

domain was constructed to represent the geometry of the lysimeter with five or six internal material regions. The CL layer was considered as one region, the SiL another region and the conductive LS layer was divided into three or four regions to facilitate the change in the flow domain geometry to account for seepage erosion undercutting the streambank. The regions were then discretized into 25 by 25 mm elements.

Specifying and assigning material properties in SEEP/W involves defining the water retention function, $\theta(h)$, and the hydraulic conductivity function, $K(h)$, where h is the soil-water pressure (Krahn, 2004a). It is a common practice to use an estimation method to represent $\theta(h)$and $K(h)$, such as the van Genuchten (1980) model:

$$\theta(h) = \begin{cases} \theta_r + \dfrac{\theta_s - \theta_r}{\left[1 + |\alpha h|^n\right]^m} & h < 0 \\ \theta_s & h \geq 0 \end{cases} \tag{1.1}$$

$$K(h) = K_s S_e \left[1 - (1 - S_e^{1/m})^m\right]^2 \qquad m = 1 - 1/n, \quad n > 1 \tag{1.2}$$

where $S_e = (\theta - \theta_r)/(\theta_s - \theta_r)$ is the effective saturation; α (L^{-1}) and n are empirical parameters; θ_s is the saturated water content; θ_r is the residual water content; and K_s (LT^{-1}) is the saturated hydraulic conductivity.

Laboratory measurements of soil hydraulic properties from undisturbed soil cores were used to define the parameters of the van Genuchten (1980) model. Soil samples were taken from LTC field sites where seepage was occurring through the conductive LS layer with a restrictive layer below (Fox et al., 2006; Wilson et al., 2007). These values were used as default soil hydraulic property values prior to calibration. Calibration of the models was carried out in two ways to match the observed hydrologic response (i.e., cumulative discharge and soil pore-water pressure): (1) by adjusting K_s of the LS layer

(due to the sensitivity of the model relative to this parameter) whereas the van Genuchten parameters (θ_s, θ_r, α, and n) and K_s of other layers were not calibrated and (2) calibration on the K_s and van Genuchten parameters of all soil layers.

SEEP/W uses either Dirichlet or Neuman boundary conditions, in which the hydraulic head or the discharge, respectively, is specified at a boundary. If the discharge is specified, SEEP/W will compute the soil-water pressure to maintain the specified discharge and vice versa. The initial conditions of the models were derived from the initial measured soil-water pressure from the lysimeter experiments. A potential seepage review boundary condition for all the nodes was assigned at the drainage face. In SEEP/W, a potential seepage review boundary condition is used when neither the hydraulic head nor the discharge are known beforehand but instead must be computed by the model (Krahn, 2004a), as in the case of the drainage from the lysimeter or bank face. A hydraulic boundary function was used as the boundary condition at the inflow face and a zero flux boundary condition was specified for the top and bottom boundaries.

The performance of the SEEP/W models was quantified by using an objective function and by visual comparison of the simulated and measured soil-water pressure and cumulative discharge. Differences between the simulated and observed cumulative discharge values were minimized based on linear regression while also minimizing the root mean square error (RMSE) of the simulated and measured soil-water pressure.

1.3.3 Streambank Stability Modeling

SLOPE/W is a numerical slope stability model which uses the theory of limit equilibrium of forces and moments to compute the *Fs* against failure. It involves discretizing a potential sliding mass into vertical slices and applying equations of statics

(Krahn, 2004b). A *Fs* is defined as that factor by which the shear strength of the soil must be reduced in order to bring the mass of soil into a state of limiting equilibrium along a selected slip surface (Figure 1.4). The *Fs* is an index of the relative stability of a slope.

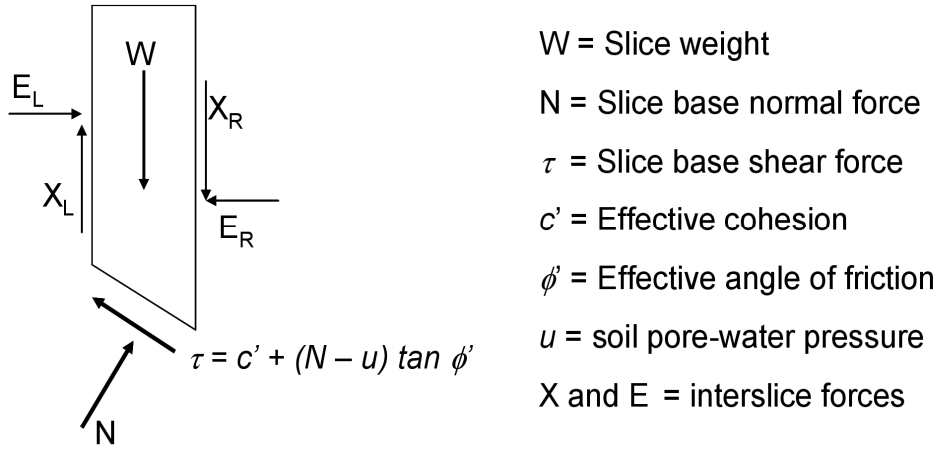

Figure 1.4 Free-body diagram of a vertical slice within a potential sliding mass and definition of the critical variables.

SLOPE/W was used to analyze the stability of the streambank as simulated by the lysimeter experiments. The stability modeling procedure had three components: (1) definition of the geometry and shape of the potential slip surface, (2) definition of the soil strength properties, and (3) definition of the soil-water pressure. SEEP/W and SLOPE/W are integrated codes such that the geometry defined in SEEP/W is used in SLOPE/W. Soil strength parameters in the lysimeter experiment were defined using Coulomb's equation. For an effective stress analysis, the shear strength is defined as:

$$s = c' + (\sigma_n - u)\tan\phi' \qquad (1.3)$$

where *s* is the shear strength, *c'* is the effective cohesion, ϕ' is the effective angle of internal friction, σ_n is the total normal stress, and *u* is the soil-water pressure (Krahn, 2004b).

The Morgenstern-Price (1965) method was selected for computing *Fs*. This method satisfies both the moment and force equilibrium equations and can give accurate results for all practical conditions (Duncan and Wright, 1980; Krahn, 2004b). The general limit equilibrium method uses the relationship proposed by Morgenstern and Price (1965) which is:

$$X = E\lambda f(x) \tag{1.4}$$

where *f(x)* is the specified function, λ is the percentage of the specified function, *E* is the interslice normal force, and X_R and X_L is the interslice shear forces on either side of a slice. The general limit equilibrium method then uses the following equations of statics to solve for the *Fs*, where *W* is the slice weight; *D* is the line load; β, *R*, *x*, *f*, *d*, and ω is the geometric parameters; and α' is the inclination of the base:

The summation of forces in a horizontal direction for each slice is used to compute the interslice normal force, *E* (equation 1.4). This equation is applied in an integration manner across the sliding mass (i.e., from left to right).

The summation of forces in a vertical direction for each slice is used to compute the normal force at the base of the slice, *N*, where *F* is either the moment or force equilibrium factor of safety:

$$N = \frac{W + (X_R - X_L) - \dfrac{c'\beta\sin\alpha' + u\beta\sin\alpha'\tan\phi'}{F}}{\cos\alpha' + \dfrac{\sin\alpha'\tan\phi'}{F}} \tag{1.5}$$

The summation of moments about a common point for all slices can be rearranged and solved for the moment equilibrium factor of safety, F_m.:

$$Fm = \frac{\sum\left(c'\beta R + (N-u)R\tan\phi'\right)}{\sum W - \sum Nf \pm \sum Dd} \tag{1.6}$$

The summation of forces in a horizontal direction for all slices, gives rise to a force equilibrium factor of safety, *Fs*:

$$Fs = \frac{\sum\left((c'\beta\cos\alpha' + (N - u\beta)\tan\phi'\cos\alpha'\right)}{\sum N\sin\alpha' - \sum D\cos\omega} \tag{1.7}$$

where *F* is *Fm* when *N* is substituted into equation (1.6) and *F* is *Fs* when *N* is substituted into equation (1.7). The relationship between the interslice normal force (*E*) and the interslice shear force (*X*) were both considered and the interslice function was derived from a half-sine function.

The soil-water pressure distribution generated from SEEP/W was input into SLOPE/W. The model was then run using the soil-water pressure at every time step to determine the effect of the changes on the stability of the slip surface. The auto-search option was chosen for defining the potential slip surface. In this method, SLOPE/W generated 1000 trial slip surfaces to find the most probable minimum slip surface based on the problem's geometry by identifying the most probable entry and exit areas of the slip surface. This method can result in unrealistic slip outputs so that comparison of the generated slip surface with the actual appearance of the collapsed bank is necessary.

For each lysimeter experiment, a probabilistic slope stability approach of solving the *Fs* was adopted by considering the variability of the soil strength parameters of the SiL and LS layers. SLOPE/W can perform a probabilistic slope stability analysis which allows for the consideration of variability in input parameters (Krahn, 2004b). The user can assign a probability density function (pdf) to input parameters (Caviness et al., 2006). Using the specified pdf, SLOPE/W derives the cumulative distribution function by integrating the area under the pdf. The cumulative distribution function is then inverted to produce the sampling function. Each time a random number is generated from Monte

Carlo method, the parameter is "sampled" using this function. The randomly generated parameter is then fed into the deterministic model to compute the *Fs*.

Field measurements of cohesion, angle of internal friction, and total unit weight from the LTC streambank site where the lysimeter soil was sampled were carried out using a borehole shear test at two field locations. Average soil strength values (Table 1.2), were used to define the material properties of the layers for the slope stability model. The variability in these soil strength parameters was assumed to follow a normal probability density function similar to most geotechnical engineering material properties (Krahn, 2004b). A standard deviation equal to 2.0 was chosen and 2000 Monte Carlo trials were simulated as suggested by Krahn (2004b).

Table 1.2 Soil strength parameters of Little Topashaw Creek (LTC) streambank based on measurements at two sites where seepage erosion was observed. Values for cohesion and angle of internal friction are average values used in the SLOPE/W model. Parameter values in parentheses are values from each site.

Layer	Depth (m)	Cohesion (kPa)	Angle of Internal Friction (^{o})	Total Unit weight (kN/m^3)
Silt loam (SiL)	0.5	7.5 (5.0, 10.0)	30.0 (25.0, 35.0)	16.0
Loamy sand (LS)	1.5	1.0 (1.0, 1.0)	25.5 (22.0, 29.0)	19.0
Clay Loam (CL)	2.0	15.0 -15.0	35.0 -35.0	21.0

The unavailability of models to simulate undercutting, which modifies the flow domain with time, makes it difficult to quantify the importance of seepage erosion in slope stability analysis. SEEP/W uses a finite element method which requires the elements to be connected at the corners by nodes which is not representative of an undercutting process where the elements tend to "break-away" from the adjacent elements. SLOPE/W on the other hand, being a limit equilibrium program, cannot model over hanging walls or undercut slopes where the base of some slices are exposed to the air. This is the case of undercutting brought about by seepage erosion. In order to overcome these limitations, a procedure was developed to incorporate the effects of undercutting into the variably saturated flow stability models.

For the lysimeter experiments, seepage erosion was simulated by manually changing the geometry of the LS layer based on available data for the dimensions and shape of the undercutting. The shape, dimensions and timing of undercutting were measured during the lysimeter experiment as reported by Periketi (2005) and Wilson et al. (2007). From this information, seepage erosion was modeled by dividing the LS layer into segments. Changes in the geometry of the domain to reflect the shape and location of the undercutting (e.g., Figure 1.5) was accomplished by changing the material properties of segments. SLOPE/W's limitation regarding undercutting was addressed by covering the cut with a null region without specifying any soil strength properties. In SEEP/W, this region was treated as a void in the flow domain by not assigning a material property (Figure 1.5). This will exclude the weight of the null region in the analysis. The performance of the SLOPE/W models in predicting the shape of the critical slip surface

was evaluated by comparing the measured dimensions of the collapsed bank against the critical slip surface generated by the model.

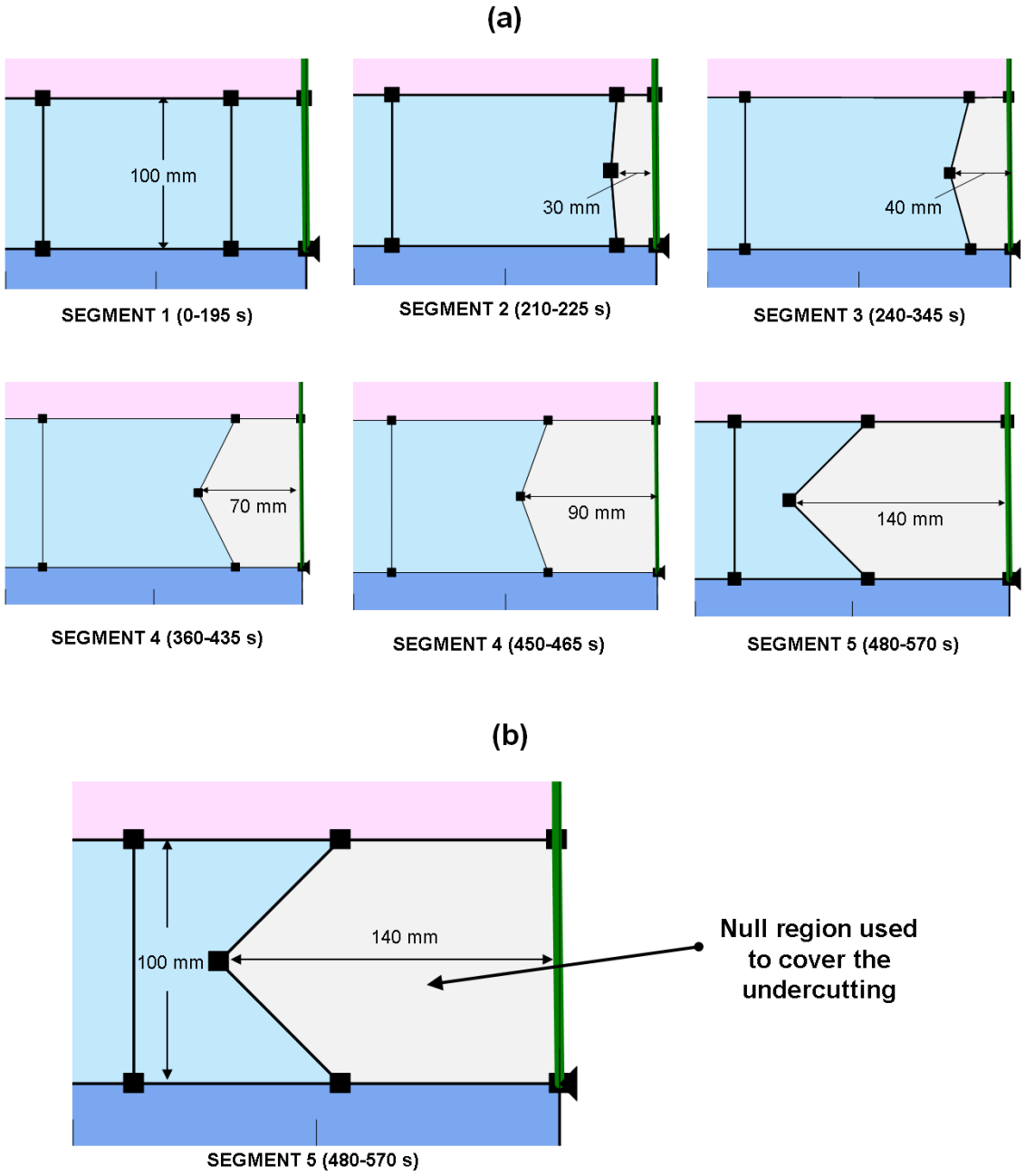

Figure 1.5 (a) Change in the geometry in the SLOPE/W modeling of the loamy sand (LS) layer experiencing undercutting by seepage erosion and (b) null region used in place of the seepage undercut in the SLOPE/W model. Figures shown are for experiment with H = 0.6 m, BH = 0.8 m, and S = 0%.

1.4 RESULTS AND DISCUSSION

Calibrated values of LS layer K_s (i.e., 180.0 to 632.0 cm/d) in each SEEP/W lysimeter model varied from the field-measured average value (i.e., 1453.1 cm/d) reported by Fox et al. (2006) and Wilson et al. (2007) (Table 1.3). RMSEs between observed and predicted soil-water pressure are outlined in Table 1.4 and results of the linear regression between predicted and measured cumulative discharge are outlined in Table 1.5 for two cases: (1) prior to calibration and (2) after calibration on the LS K_s. Tensiometer 8 in the SiL layer of the 0.8 m *BH*, 0% *S*, and 0.3 and 0.6 m *H* experiments did not operate properly during the experiments and was not considered in the calibration process. Simply calibrating on the LS K_s provided a reasonable fit (i.e., maximum RMSE of 0.13) in terms of soil pore-water pressure compared to calibration on K_s and water retention parameters of all soil layers (i.e., maximum RMSE of 0.11). It is this pore-water pressure distribution which is critical for the SLOPE/W stability software. The benefit of calibration on the K_s of other layers and water retention parameters was in regard to prediction of cumulative discharge as quantified through the slope and R^2 of the linear regression (Table 1.5, Figure 1.6). However, this improved fit required the use of unrealistic values for the van Genuchten parameters in the LS layer.

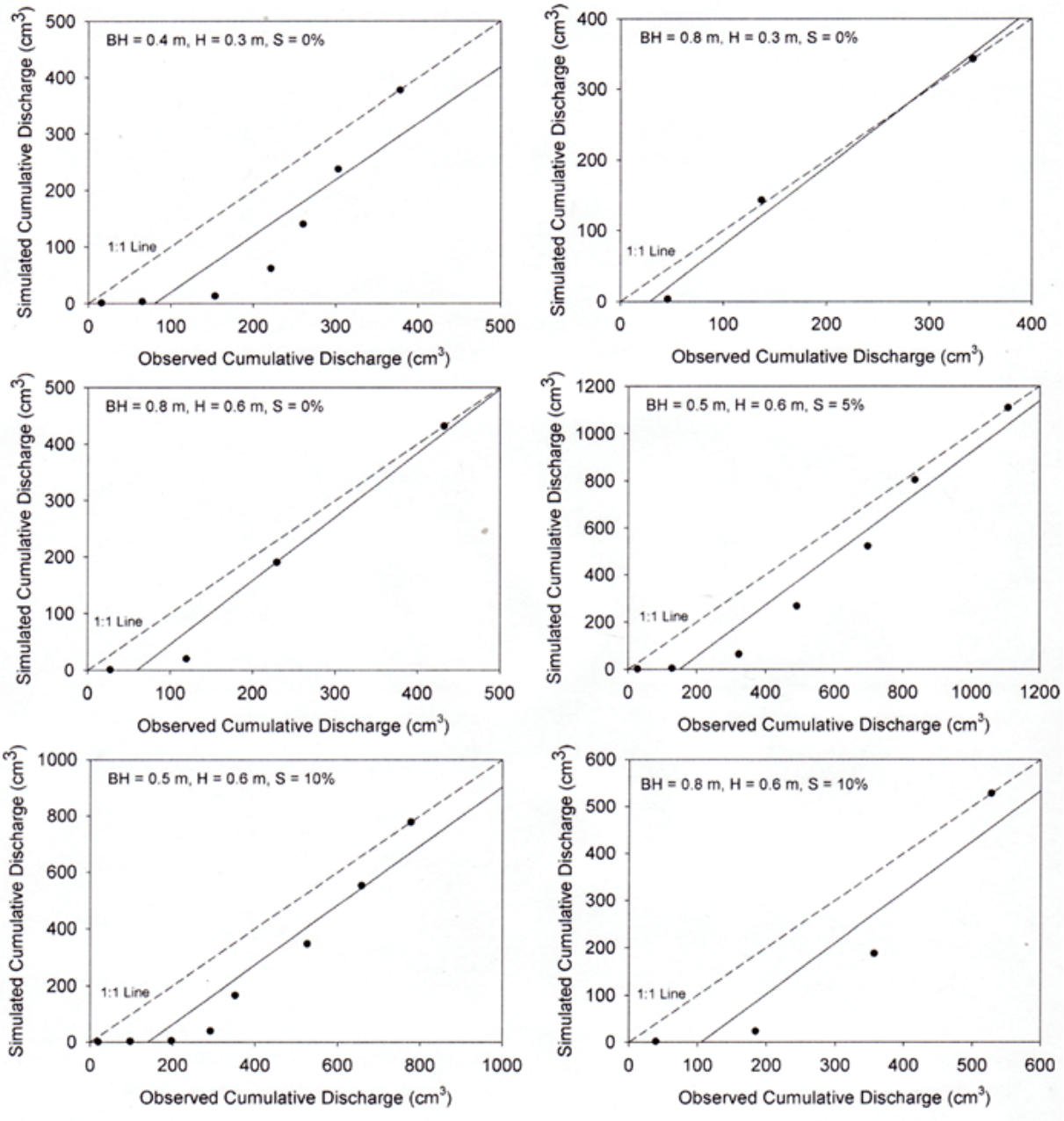

Figure 1.6 Observed versus SEEP/W predicted cumulative discharge for six lysimeter experiments after calibration on K_s. and soil-water retention parameters (θ_s, a, and n) were not calibrated for other soil layers.

Table 1.3 Field measured hydraulic conductivity, K_s, and soil-water retention parameters of Little Topashaw Creek streambank sediment and comparison to calibrated LS layer K_s, for lysimeter experiments; SEEP/W model was most sensitive to this parameter, therefore all other parameters were not part of model calibration.

	Soil Layer	K_s (cm/day)	θ_s (cm^3 cm^{-3})	α (kPa)	*n*
Field Measured Parameters					
	SiL	63.9	0.39	4.9	3.5
	LS	1453.1	0.40	2.5	3.0
	CL	5.4	0.44	9.8	1.7
Calibrated Parameters for Lysimeter Experiments					
H=0.3 m, BH=0.4 m, S=0%	LS	180.0	---	---	---
H=0.3 m, BH=0.8 m, S=0%	LS	628.0	---	---	---
H=0.6 m, BH=0.8 m, S=0%	LS	632.0	---	---	---
H=0.6 m, BH=0.5 m, S=5%	LS	556.0	---	---	---
H=0.6 m, BH=0.5 m, S=10%	LS	363.0	---	---	---
H=0.6 m, BH=0.8 m, S=10%	LS	603.0	---	---	---

Note: θ_s = Saturated water content; and α and *n* are emprical parameters.

Table 1.4 Root mean square error (RMSE) of measured and SEEP/W simulated soil-water pressure for tensiometers in each lysimeter experiment before calibration and after calibration on K_s of LS layer.

Lysimeter Experiment			Tensiometers								
H (m)	*BH* (m)	*S* (%)	1	2	3	4	5	6	7	8	9
(a) Prior to calibration											
0.3	0.4	0	0.17	0.08	0.08	0.07	0.08	0.11	0.08	0.06	0.01
0.3	0.8	0	0.06	0.06	0.07	0.01	0.01	0.04	0.03	---	0.04
0.6	0.8	0	0.11	0.07	0.21	0.02	0.02	0.06	0.05	---	0.09
0.6	0.5	5	0.04	0.06	0.21	0.04	0.04	0.04	0.03	0.06	0.08
0.6	0.5	10	0.03	0.01	0.21	0.06	0.06	0.05	0.05	0.08	0.10
0.6	0.8	10	0.03	0.01	0.15	0.04	0.06	0.06	0.04	0.09	0.09
(b) Calibration on K_s of LS											
0.3	0.4	0	0.04	0.02	0.03	0.06	0.02	0.10	0.03	0.02	0.03
0.3	0.8	0	0.04	0.03	0.04	0.03	0.04	0.03	0.03	---	0.06
0.6	0.8	0	0.07	0.01	0.13	0.04	0.07	0.05	0.04	---	0.11
0.6	0.5	5	0.03	0.02	0.10	0.05	0.10	0.10	0.02	0.06	0.08
0.6	0.5	10	0.03	0.03	0.05	0.06	0.10	0.11	0.02	0.03	0.08
0.6	0.8	10	0.03	0.03	0.04	0.05	0.11	0.12	0.03	0.05	0.07

Note: The location of tensiometers Nos. 1-9 is depicted in Figure 1.1

Table 1.5 Regression between measured and SEEP/W simulated cumulative discharge in each lysimeter experiment prior to calibration and after calibration on K_s of LS layer.

H (m)	*BH* (m)	*S* (%)	Regression Line Slope	Regression Line Intercept (m^3)	R^2
(a) Prior to calibration					
0.3	0.4	0	25.02	1.11E-03	0.98
0.3	0.8	0	5.17	2.17E-04	0.91
0.6	0.8	0	5.52	1.07E-04	0.97
0.6	0.5	5	5.02	3.13E-04	0.99
0.6	0.5	10	9.92	3.88E-04	0.99
0.6	0.8	10	5.51	1.23E-04	0.99
(b) Calibration on K_s of LS					
0.3	0.4	0	1.00	-8.01E-05	0.82
0.3	0.8	0	1.12	-3.21E-05	0.99
0.6	0.8	0	1.13	-6.72E-05	0.97
0.6	0.5	5	1.08	-1.62E-04	0.95
0.6	0.5	10	1.05	-1.46E-04	0.91
0.6	0.8	10	1.08	-1.13E-04	0.88

Soil-water pressure generated from SEEP/W at specific time steps were used to define the input soil-water pressure in SLOPE/W. The predicted, mean Fs when undercutting was not considered, Figure 1.7, did not significantly change during any of the lysimeter simulations. Changes in soil-water pressure did not sufficiently affect soil strength in these experiments and therefore did not reduce the stability of the bank. Yet it is the impact of soil-water pressure on soil strength that is most often attributed to bank failure (e.g., Burgi and Karaki, 1971; Edil and Vallejo, 1980; Darby and Thorne, 1996; Abam, 1993; Crosta and Prisco, 1999; Rinaldi and Casagli, 1999; Simon et al., 1999; Dapporto et al., 2003). In contrast to the impact of soil-water pressure, the *Fs* decreased approximately 42% (from a mean value of 1.06 to 0.62) and 55% (from a mean value of 1.05 to 0.47) for experiments with 0.3 and 0.6 m *H* (0.8 m *BH* and 0% *S*), respectively,

when seepage particle mobilization and undercutting was considered (Figure 1.7). This resulted in an unstable bank (i.e., *Fs*<1.0) at the end of the simulation. Experiments with greater than 0% slope were predicted to be unstable at the beginning of the simulation based on the mean *Fs* (*Fs*<1.0). The *Fs* for these experiments decreased 50 to 91% between simulations when seepage undercutting was included.

For stable banks with sufficient undercutting measurements (i.e., 0.8 m *BH*, 0% S), the change in the probability of failure, or risk of instability, predicted by the modeling, increased from 35.2% to 100% for H = 0.3 m, and from 36.5% to 100% for H = 0.6 m when seepage undercutting became active (Figure 1.8). The probability of failure is determined by counting the number of *Fs* values less than 1.0 with respect to the total number of converged slip surfaces. It is equivalent to the percentage of slopes that would fail if a slope were to be constructed repeatedly. A probability of failure equal to 100% was reached when the depth of undercutting reached approximately 30 to 50 mm into the bank for this specific streambank profile. Since the parameters used in the simulation with and without seepage erosion were the same, the increase in the probability of failure and decrease in the *Fs* can be attributed to the change in the geometry of the LS layer due to simulated undercutting by seepage erosion. The results also show that a stable bank (i.e., *Fs*>1.0) can become significantly unstable when seepage erosion is considered.

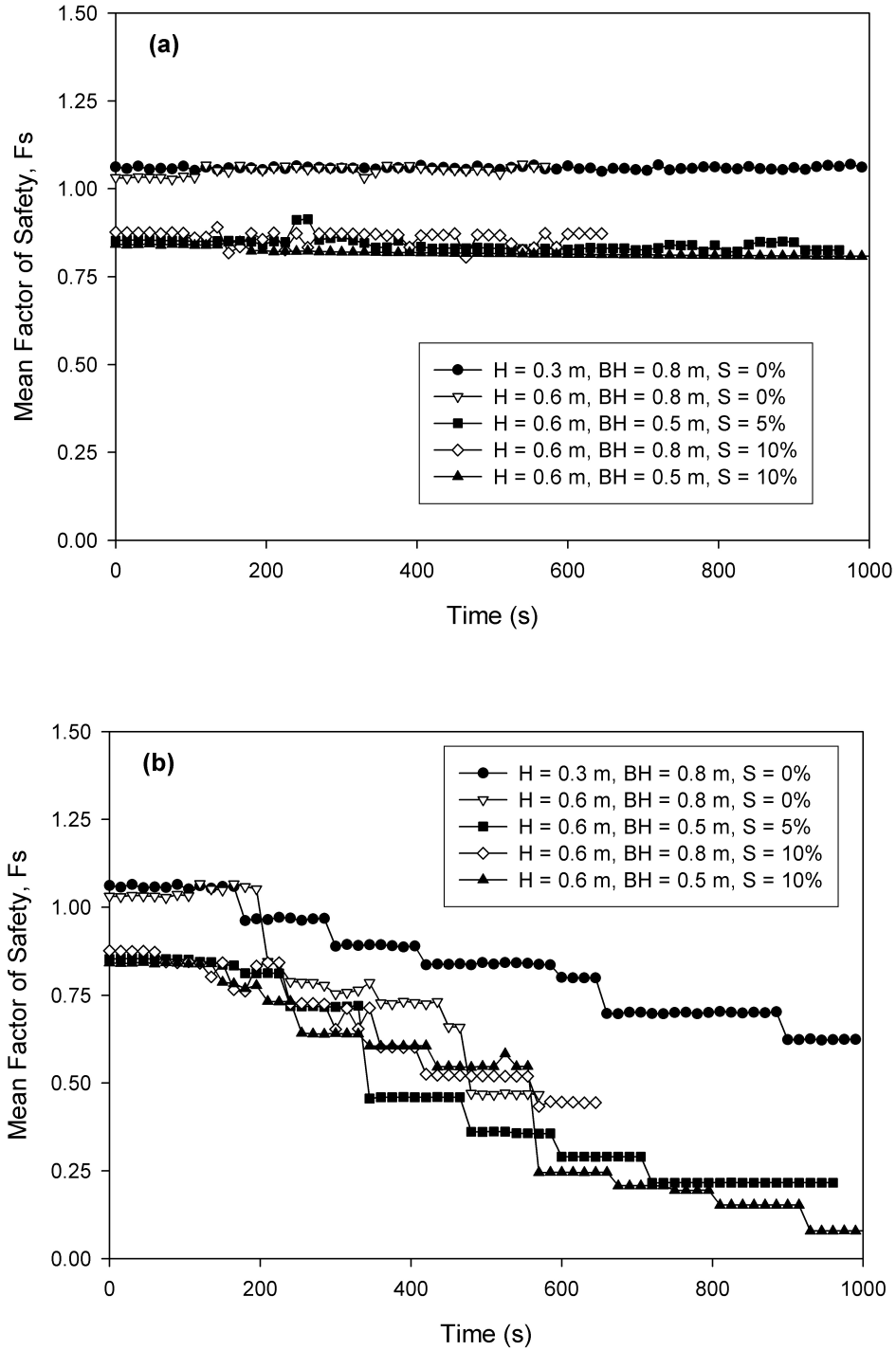

Figure 1.7 Mean factor of safety (*Fs*) versus time as predicted by SLOPE/W Monte Carlo analysis for lysimeter experiments (a) without considering seepage undercutting and (b) with seepage undercutting.

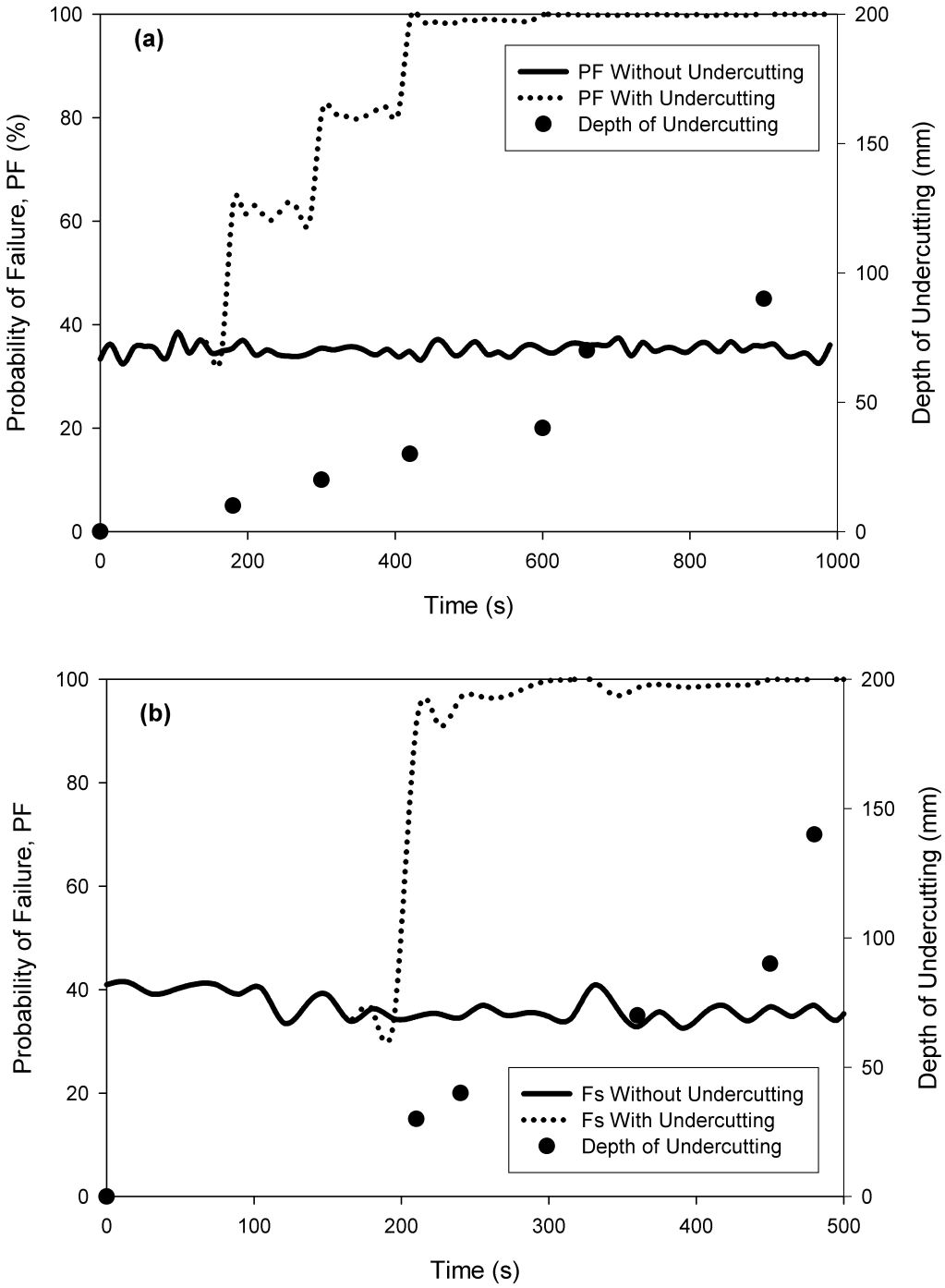

Figure 1.8 Simulated probability of failure (*PF*, %) of lysimeter experiments with *BH* = 0.8 m, *S* = 0%, and (a) *H* = 0.3 m, and (b) *H* = 0.6 m with and without seepage undercutting.

The SLOPE/W model consistently predicted failure ahead of the observed bank collapse (i.e., a 100% probability of failure was reached before the actual collapse observed during the lysimeter experiments). For example, SLOPE/W predicted collapse approximately 300 to 500 s before actual bank collapse for the lysimeter experiments with 0.3 and 0.6 *H* (0.8 m *BH* and 0% *S*). For the experiment where bank failure did not occur due to seepage undercutting (*H* = 0.3 m, *BH* = 0.4 m, and *S* = 0%), the model predicted a bank collapse of 0.05 m^3. This is an indication that the lysimeter setup is more stable than the bank simulated by the model. This condition can be due to three factors. First, the geotechnical parameters were simulated using field measurements as opposed to soil testing of the repacked lysimeter soil. Second, the walls of the lysimeter (only separated by 15 cm) may have induced compressive forces to counteract stresses produced by the soil weight. Also, uniform packing of disturbed soil samples can add extra strength to the bank relative to natural field heterogeneity. Even with these experimental conditions, the model predictions of bank collapses were generally within 33% of the measured volume of bank collapse (Table 1.6, Figure 1.9).

Table 1.6 Comparison of observed versus SLOPE/W predicted volume of bank collapse.

H	*BH*	*S*	Volume of Collapsed Bank (m^3)		Percent Under/Over
(m)	(m)	(%)	Measured	Simulated	Estimated
0.3	0.4	0	0.00	0.05	---
0.3	0.8	0	0.12	0.14	15.2
0.6	0.8	0	0.17	0.17	4.3
0.6	0.5	5	0.16	0.11	-33.2
0.6	0.5	10	0.17	0.17	1.1
0.6	0.8	10	0.26	0.18	-33.8

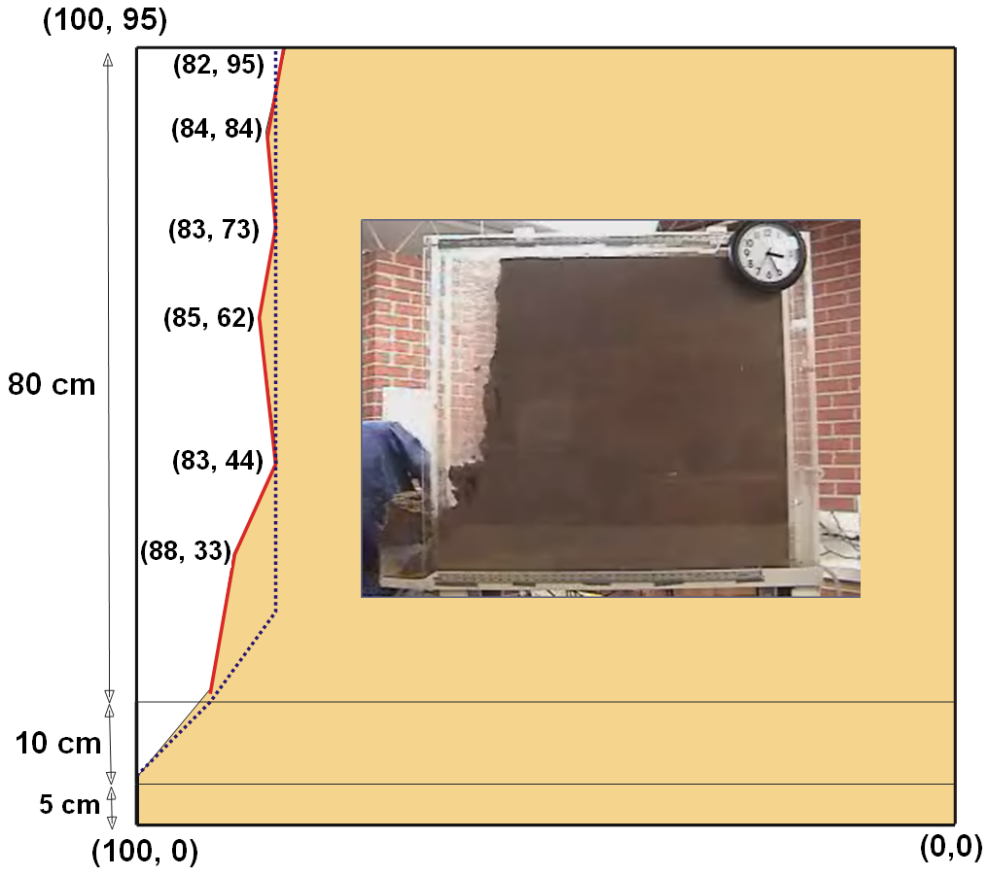

Figure 1.9 Comparison of the actual bank collapse (solid line) and the SLOPE/W predicted critical slip surface (dotted line) generated for the constant head, H = 0.3 m, bank height, BH = 0.8 m, and slope, S = 0%, lysimeter experiment. The observed bank collapse was 0.12 m^3 while the SLOPE/W predicted bank collapse was 0.14 m^3. Note that the inflow reservoir is on the opposite side to that indicated in Figures 1.2 and 1.5.

The depth of undercutting and the corresponding mean *Fs* were evaluated by grouping the six experiments into four categories. The minimum and maximum values of the *Fs* were also determined. The first category consists of experiments with the same *BH* and *S* but different *H*. As theoretically expected, these experiments possess the same initial stability. However, as time increased, the bank with higher *H* had lower *Fs* at a

given time due to the higher *H* resulted in more rapid undercutting of the bank by seepage erosion. However, the same depth of undercutting resulted in approximately the same bank stability or mean *Fs* (Figure 1.10).

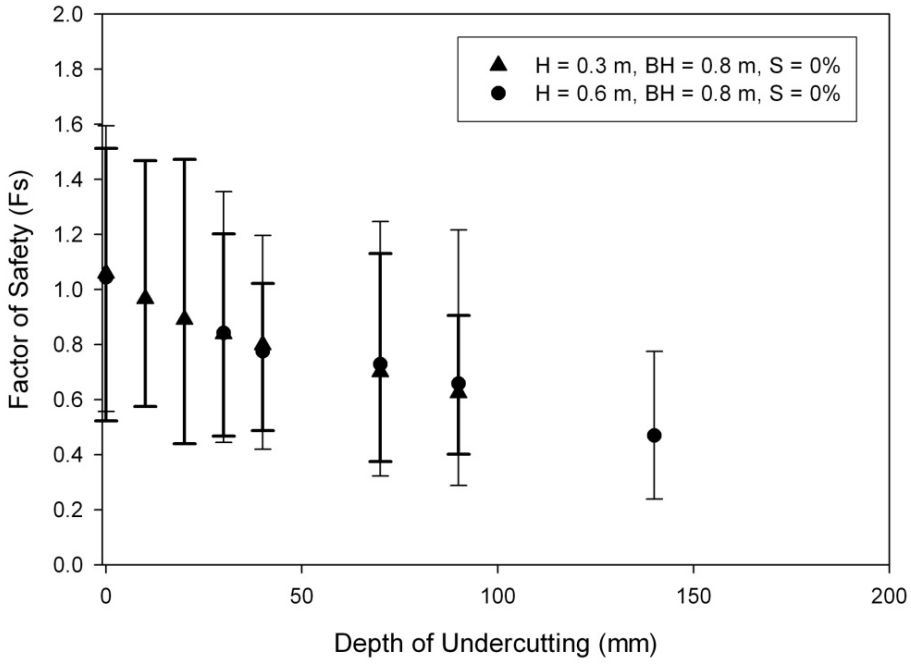

Figure 1.10 Factor of safety (*Fs*) versus depth of undercutting for two experiments with same bank height (*BH* = 0.8 m) and slope (*S* = 0%) but different constant heads (*H* = 0.3 m and 0.6 m). Error bars represent minimum and maximum *Fs* from 2000 Monte Carlo simulations

The second category consists of experiments with the same *H* and *S* but different *BH*, which possess different initial bank stabilities: the bank with *BH* = 0.4 m was initially 39% more stable than *BH* = 0.8 m. As undercutting progressed, the stability of both banks converged to approximately the same range, followed by the lower bank (*BH* = 0.4 m) being less stable than the higher bank (*BH* = 0.8 m) for undercutting depths greater than 50 cm (Figure 1.11). This crossover in the *Fs* was hypothesized to be due to

the difference in initial conditions between the *BH* = 0.4 m (i.e., initially lower soil water content) and *BH* = 0.8 m (i.e., initially at field capacity) experiments. Flow arrival at the bank face was delayed for the *BH* = 0.4 m experiment as compared to the *BH* = 0.8 m experiment and the experiment duration was greater (i.e., 2500 s as opposed to 1000 s), as demonstrated in Figure 1.6. A longer experimental duration corresponded to greater soil water movement into the upper topsoil layer (i.e., SiL) for the *BH* = 0.4 m experiment, which reduced the *Fs* more quickly than in the *BH* = 0.8 m experiment relative to the depth of undercutting.

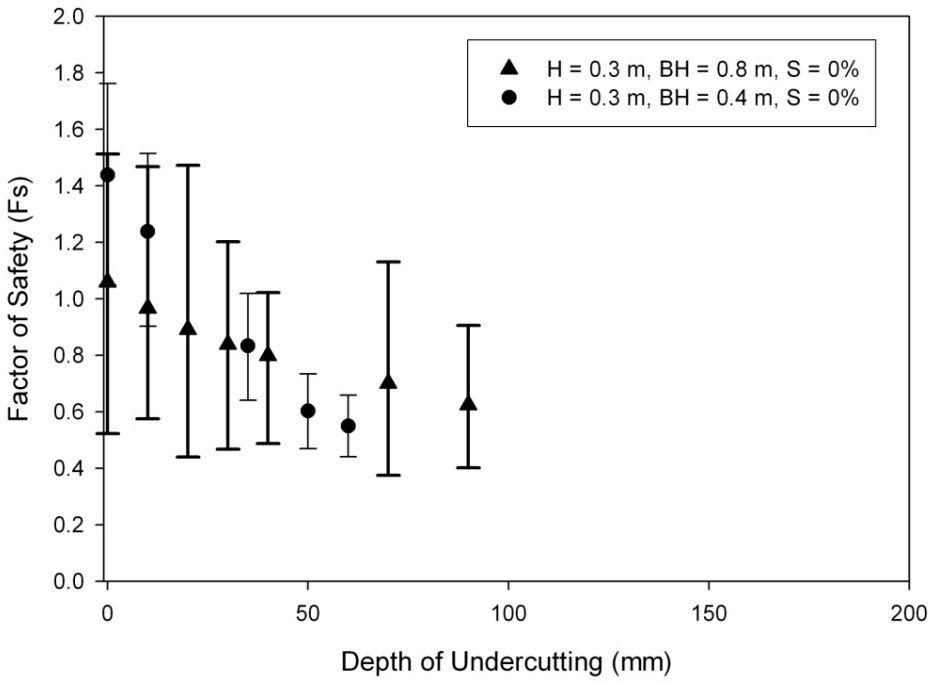

Figure 1.11 Factor of safety (*Fs*) versus depth of undercutting for two experiments with same constant head (*H* = 0.3 m) and slope (S = 0%) but different bank heights (*BH* = 0.4 m and 0.8 m). Error bars represent minimum and maximum Fs from 2000 Monte Carlo simulations.

The third and fourth categories consist of experiments with the same *H* and *BH* but different *S*, with the differences in *S* affecting the initial stability of the banks. Banks with a 5% and 10% *S* were initially unstable (*Fs*<1.0). The difference in the mean *Fs* was approximately the same for all depths of undercutting. However, the difference between the minimum and maximum values tended to decrease as the slope increased (Figure 1.12).

Comparison of the different hydraulic controls of the lysimeter experiments showed that the initial stability of the bank was controlled by the *BH* and the *S* of the bank. This reflects the basis of the equations used for limit equilibrium; i.e., bank stability when undercutting is not considered is a function of the geometry of the bank and the soil strength parameters. The size of undercutting and the change in the mean *Fs* resulting from seepage was controlled by *H*. Regardless of the initial stability of the bank, stability quickly converged as undercutting progressed. This convergence made it possible to fit a curve to the model predicted *Fs* for all six lysimeter experiments that suggested an exponential relationship between the depth of undercutting and the mean factor of safety (Figure 1.13). The regression parameters are specific to these lysimeter streambank profiles; however, the observed exponential relationship is hypothesized to occur for comparable streambank profiles influenced by seepage undercutting: the *Fs* decreases exponentially with distance of undercutting by seepage particle mobilization.

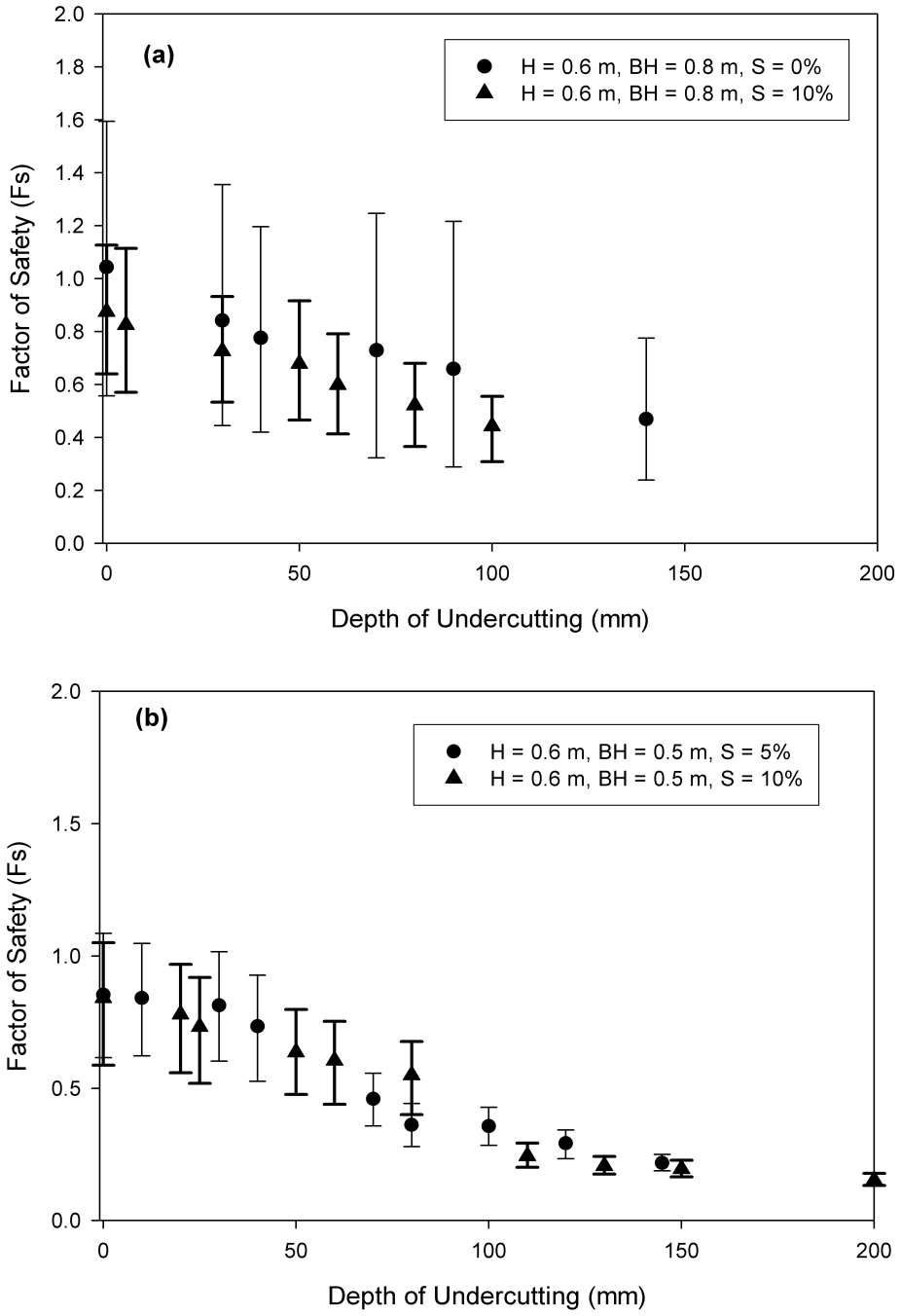

Figure 1.12 Factor of safety (*Fs*) versus depth of undercutting for experiments with same constant head (*H* = 0.6 m) and (a) same bank height (*BH* = 0.8 m) but different slopes (*S* = 0 and 10%) and (b) same bank height (*BH* = 0.5 m) but different slopes (*S* = 5 and 10%). Error bars represent minimum and maximum *Fs* from 2000 Monte Carlo simulations.

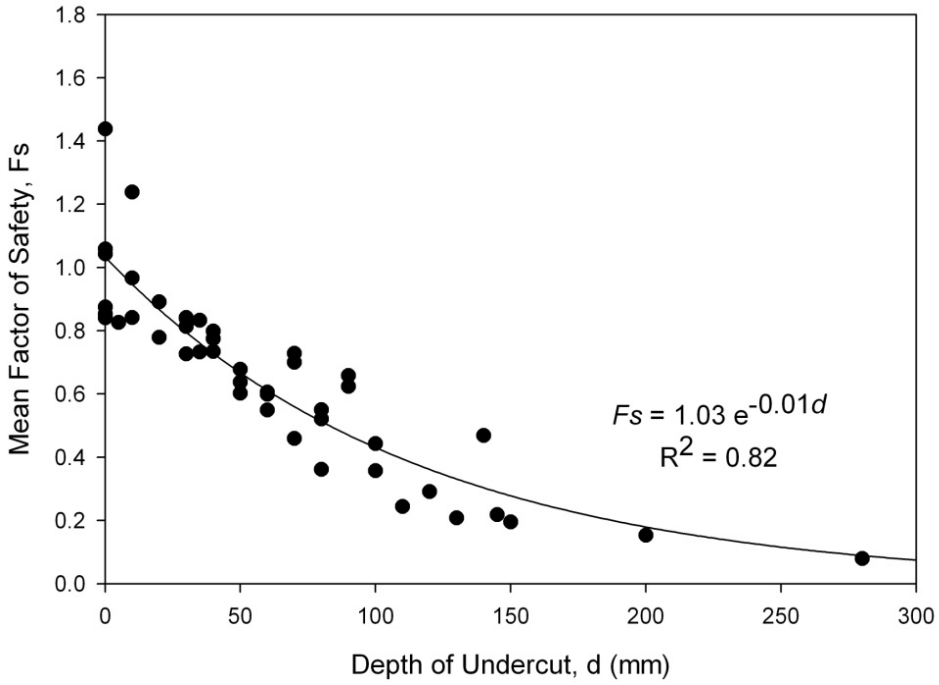

Figure 1.13 Depth of undercutting, *d*, versus mean factor of safety, *Fs*, of all six lysimeter experiments modeled with SLOPE/W.

1.5 SUMMARY AND CONCLUSIONS

This research demonstrated a procedure for incorporating seepage particle mobilization and undercutting into bank stability models using data from two-dimensional soil lysimeter experiments of layered streambanks. Changes in soil-water pressure were simulated using SEEP/W, a variably saturated numerical flow model, while bank stability was analyzed using SLOPE/W based on limit equilibrium. Undercutting was mimicked by manually changing the geometry of the flow domain for the conductive layer based on the measured dimensions, shape and timing of the undercutting due to seepage erosion. The mean *Fs* was used as an index of bank stability for all experiments.

Changes in soil strength, in response to soil-water pressure changes during seepage, were not sufficient to contribute to bank instability, yet the mean *Fs* decreased significantly as the depth of undercutting increased. The decrease in the mean *Fs* due to undercutting was in the range of 42 to 91% depending on the initial stability of the bank. Regardless of the initial stability of the bank, instability converged as undercutting progressed. This means that a stable bank can quickly become unstable when seepage undercutting is considered. For stable banks, the probability of failure reached 100% when the depth of the undercutting reached approximately 30 to 50 mm for these experimental conditions. Bank height and bank slope controlled the initial stability of the bank, while the established constant head controlled the depth of undercutting and the mean *Fs* as undercutting progressed. Based on the results of the lysimeter experiments, the mean *Fs* is exponentially related to the depth of undercutting.

Prior to this work, undercutting was primarily considered from a fluvial process perspective. In situ measurements of seepage erosion documented that undercutting occurs by seepage erosion independent of fluvial process. These findings, along with measurements of streambank physical properties, guided laboratory experiments of seepage erosion for a range of hydrologic conditions. This work is unique in that these experiments were used to calibrate a variably saturated flow model integrated with a geotechnical slope stability model that simulated undercutting due to seepage erosion based upon field measurements of the geotechnical properties without calibration but with stochastic sampling of the properties probability density function. The numerical modeling showed that seepage erosion can lead to distances of undercutting that are a significant cause of bank instability. The loss of supporting material brought about by

seepage particle mobilization and undercutting can be a major cause of slope instability and may be of equal or greater importance than the impact of increased soil-water pressure on soil strength for such streambank conditions.

Future work should be aimed at incorporating this instability mechanism into streambank stability models. The difficulty with current models is the need to know a priori the distance of seepage undercutting. Future work should establish relationships between the volume and shape of undercutting with seepage flow velocity under a variety of hydrologic conditions and soil properties such that a sediment transport equation can be added into the bank stability model to provide predictive capabilities without a priori knowledge of the undercutting.

CHAPTER 2

Seepage Caused Tension Failures and Erosion Undercutting of Hillslopes[2]

2.1 ABSTRACT

Seepage has been suggested as an important factor in gully and river bank erosion. This study investigated the underlying mechanisms of instability by seepage in laboratory studies. A 25-cm tall, 50-cm wide, and 20-cm long soil block with a focused inflow reservoir was constructed to investigate seepage gradient forces and the three-dimensional nature of seepage particle mobilization (i.e., seepage erosion) and undercutting. Experiments included sand and loamy sand soil blocks packed at prescribed bulk densities (1.30 to 1.70 Mg m^{-3}) and with an outflow face at various angles (90, 75, and 60 degrees). Constant heads of 15 cm, 25 cm, and 35 cm were imposed on the soil to induce flow. A laser scanner was utilized to obtain the three-dimensional coordinates of the bank and undercut surfaces at approximately 15 to 30 s intervals. The bulk density of the two soils controlled which seepage failure mechanism occurred: (1) tension or "pop-out" failures due to the seepage force exceeding the soil shear strength that was being concurrently reduced by increased soil pore-water pressure, or (2) particle entrainment in the seepage flow, particle mobilization, bank undercutting, and bank collapse when the

[2] Published in *Journal of Hydrology*, 2008
Chu-Agor, M.L., G.A. Fox, R. Cancienne, G.V. Wilson. 2008. Seepage Caused Tension Failures and Erosion Undercutting of Hillslopes, *J. Hydrol*. 359, 247-259.

initial seepage force gradient was less than the resistance of the soil block. For cases experiencing particle mobilization and undercutting, seepage erosion initiated as unimodal (i.e., concentrated at one point) or as multimodal (i.e., initiating at several locations across the bank face), and this result was largely controlled by the bank angle. A five parameter Gaussian function was fitted to the measured three-dimensional undercut shapes to derive parameters for the maximum depth of undercutting, position of the center of the peak, and the vertical and lateral spreads of the undercut. The parameters of this distribution can be useful in the development of improved sediment transport functions and the incorporation of this failure mechanism into hillslope stability models.

2.2 INTRODUCTION

Seepage has been suggested to potentially play a prominent role in gully and streambank erosion (Abam, 1993; Darby and Thorne, 1996; Crosta and Prisco, 1999; Rinaldi and Casagli, 1999; Simon et al., 1999). Seepage is now accepted, especially in Europe, as a critically important process in rill and gully development (Faulkner, 2006; Sultan et al, 2003). This research, and its corresponding literature review, are placed in the context of streambank failure but is equally applicable to hillslope failure and gully development in its assessment of seepage mechanisms.

The complex interaction between seepage and other bank stability and instability mechanisms (i.e., fluvial erosion, confining pressure, and vegetation) makes it difficult to fully understand the role of seepage on bank instability. According to Crosta and Prisco (1999), in order to understand the onset of streambank instability due to seepage, it is important to point out that the collapse is the final result of a complex chain of events

taking place during a certain time period. They added that analysis is complex because of the partial saturation of the materials, the three-dimensional geometry of the problem, and the heterogeneity of materials. Hooke (1978) suggested that more detailed work is needed on the effects of soil moisture, the pattern of forces on the bank and the changes in shear strength of the bank material. The ASCE Task Committee on Hydraulics, Bank Mechanics, and Modeling of River Adjustments (1998) suggested that methods capable of predicting the stability of streambanks with respect to a range of possible failure mechanisms must be developed.

Some of the complexity regarding seepage stems from the fact that seepage can cause hillslope instability through three different but interrelated mechanisms: (1) increased soil pore-water pressure reducing the shear strength of the soil, (2) seepage gradient forces, and (3) seepage particle mobilization and undercutting. Most research to date has focused specifically on one of these three mechanisms.

2.2.1 Increased Soil Pore-Water Pressure

Soil strength or the resisting force which is responsible for bank stability is usually defined using Mohr-Coulomb's equation:

$$s = c' + (\sigma_n - u_w)\tan\phi' \tag{2.1}$$

where s is the shear strength, c' is the effective cohesion, ϕ' is the effective angle of internal friction, σ_n is the total normal stress, and u_w is the soil pore-water pressure (Whitlow, 1983; Fredlund and Rahardjo, 1993). In unsaturated soils, decreasing matric suction has the effect of increasing the apparent cohesion of the soil, as described by Fredlund and Rahardjo (1993):

$$s = c' + (\sigma_n - u_w)\tan\phi' + (u_a - u_w)\tan\phi^b \tag{2.2}$$

where u_a is the soil pore-air pressure and ϕ^b is the angle indicating the rate of increase in the shear strength relative to matric suction and is generally between 10 and 20 degrees (Fredlund and Rahardjo, 1993; Simon et al., 1999). Therefore, an increase in pore-water pressure decreases the effective stress of the soil which in turn decreases the shear strength.

Sultan et al. (2003) analyzed the different slope failure events from the COSTA (Continental Slope Stability) target areas (Adriatic margin, Western Mediterranean margin, and Northeast Atlantic margin). Their study identified the relation between triggering mechanisms and causal factors (e.g. slope angle) on one hand and the stress state and geotechnical parameters on the other hand. They concluded that excess pore water pressure was a key parameter for the assessment of slope stability. Rinaldi et al. (2003) monitored and modeled the pore water pressure changes and river bank stability during flow in the Sieve River in Italy. Simulations showed that the development of relatively limited pore water pressure and the disappearance of apparent cohesion were sufficient conditions to trigger a mass failure in a streambank composed predominantly of fine-grained, weakly cohesive soil (silt and sand). Lourenco et al. (2006) investigated the influence of permeability variations on slope behavior by experimental means. Their results revealed no clear link between the failure mode and recorded pore water pressure. Failure was not confined to a single failure mode, but ranged instead from retrogressive slides and lateral spreads.

2.2.2 Seepage Gradient Forces and Tension Failures

Seepage forces act on grains of sediment and are proportional to the hydraulic gradient $\frac{\partial \psi}{\partial y}$, where ψ is the matric suction and y is a distance:

$$\tau_s = \rho g d \frac{\partial \psi}{\partial y} \tag{2.3}$$

where τ_s is the seepage stress, ρ is the density of the fluid, g is gravity, and d is the grain diameter (Lobkovsky et al., 2004). Budhu and Gobin (1996) studied cohesionless slope instability due to ground-water seepage in order to provide bounds on the seepage direction that provoked slope failures, referred to in this research as tension or "pop-out" failures. They concluded that slope failures resulting from seepage forces were progressive and the minimum stable seepage direction was reached when seepage was parallel to the cohesionless bank slopes. They also showed that the seepage direction that initiates static liquefaction depends on the slope angle and the soil unit weight.

2.2.3 Seepage Particle Mobilization and Undercutting (Seepage Erosion)

Despite the research conducted on bank instability by increased soil pore-water pressure and tension or "pop-out" failure by seepage forces, our ability to predict bank failure due to seepage particle mobilization (i.e., entrainment in the seepage flow or seepage erosion) remains limited. Although seepage erosion has been observed to occur before massive bank slumping (Bradford and Piest, 1977), it is not until recently that it has been highlighted as a potential failure mechanism of streambanks particularly on the recession limb of the streamflow hydrographs (Fox et al., 2007a; Wilson et al., 2007).

On banks with enough resistance to overcome seepage forces, the seepage gradient can cause particle mobilization when the velocity of water exiting the bank exceeds the critical shear stress leading to bank undercutting. Several studies have incorporated the seepage force given by equation (2.3) into equations for particle mobilization, such as Lobkovsky et al. (2004) who modified the Shields number to include this seepage force and Fox et al. (2006) who derived a seepage erosion sediment

transport function with an excess critical discharge formulation. Seepage particle mobilization and undercutting was studied by Fox et al. (2006, 2007a, 2007b) and Wilson et al. (2007) in their two-dimensional lysimeter experiments and bank stability modeling. Wilson et al. (2007) and Chu-Agor et al. (2008) performed step-wise dynamic analysis of the effect of changes in the hillslope geometry due to undercutting on stability. Their work demonstrated that bank stability decreased exponentially as undercutting increased. However, a fully integrated variably saturated flow model with a dynamic geometric and geotechnical model to predict hillslope failure is still lacking. Knowledge on the three-dimensional structure of seepage entrainment and undercutting is needed for this dynamic hydraulic and geotechnical modeling.

2.2.4 Objectives

In this study, the hydraulic conditions producing seepage failure mechanisms (i.e., reduced soil shear strength, seepage gradient forces, and seepage particle mobilization and undercutting) were evaluated. We established the limiting conditions for tension or "pop-out" failures by seepage gradient forces as well as investigated the three-dimensional nature of seepage particle mobilization and undercutting. Therefore, this study was one of the first studies to consider multiple seepage mechanisms simultaneously.

2.3 MATERIALS AND METHODS

2.3.1 Experimental Setup and Data Collection

A three-dimensional soil block was constructed in a Plexiglas box (Figure 2.1). The box had two compartments: (1) a focused water reservoir (10 cm high by 10 cm wide centered at the bottom of the back face of the soil block) where a constant water head was

maintained and (2) the soil compartment which simulated a single layered hillslope, gully sidewall, or streambank with varying bank angles, α'. Two different soil textures were used for these experiments: sand and loamy sand. Each soil type was packed in the box at various bulk densities (ρ_b): 1.30, 1.45, and 1.60 Mg m^{-3} for the sand and 1.30, 1.45, 1.50, 1.60, and 1.70 Mg m^{-3} for the loamy sand. Dimensions of the soil block in all experiments were 25 cm high, 50 cm wide and 20 cm long. Also, all experiments were run in duplicate. This research did not evaluate differences in regard to bank height because Chu-Agor et al. (2008b) demonstrated that bank height only impacts initial stability of the bank, not the seepage mechanisms. The bottom of the soil block was lined with a 2.5 cm densely packed clay layer to serve as a restrictive layer. The rest of the block was packed with soil to the desired ρ_b in 2.5 cm lifts. All soil was packed when the soil had reached near residual soil moisture content (i.e., 0.05 to 0.10 g water per g soil). The soil was then cut to simulate various bank angles, α' (90, 75, and 60 degrees) such that the horizontal centerline for each bank remained 20 cm away from the water inlet. For the experiments, hydraulic heads (H) of 15, 25, or 35 cm were maintained in the inflow reservoir using a Marriott-type infiltrometer.

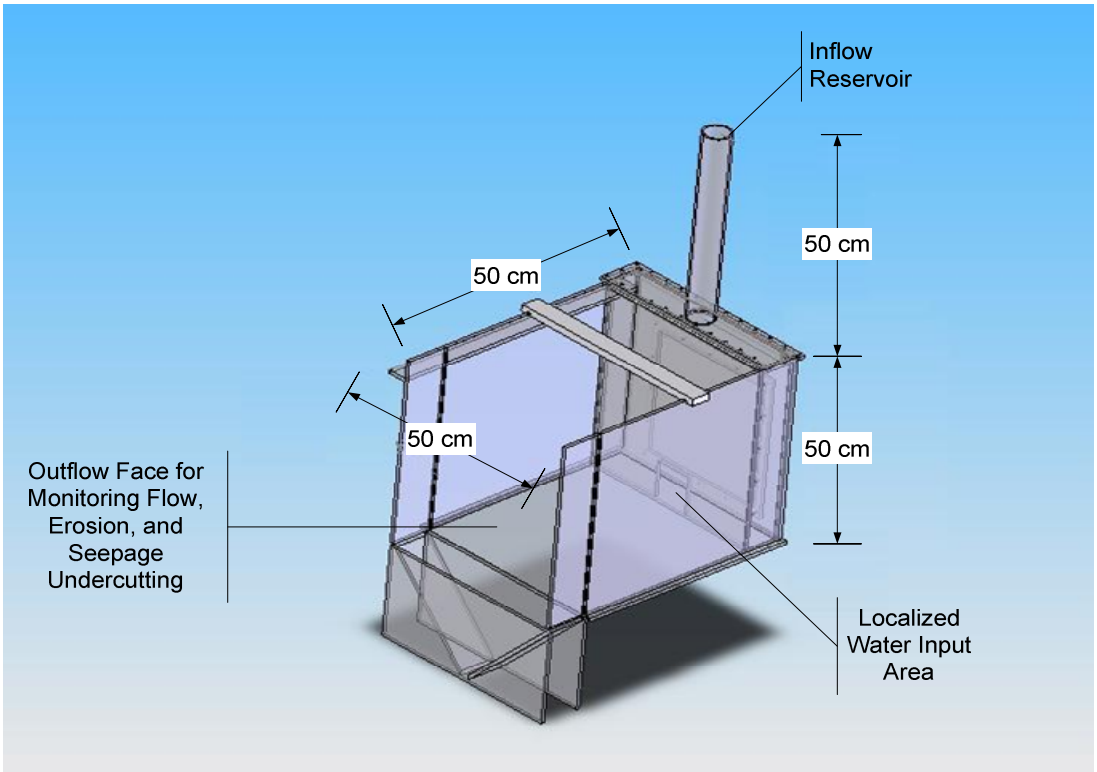

Figure 2.1 Three-dimensional soil block used to simulate seepage instability of single-layer, repacked soil banks. The inflow reservoir is capable of producing seepage heads up to 100 cm.

Data collected during the experiments included the flow arrival time at the bank face, the time of seepage erosion initiation, seepage erosion as a function of time, and the volume of bank collapse. During the experiment, seepage erosion particle mobilization and undercutting was monitored over time using a three-dimensional laser scanner (3D Digital Corporation, Sandy Hook, CT). This laser scanner was a medium range scanning instrument with resolutions of 135 μm at a scanning distance of 300 mm or 210 μm at a scanning distance of 650 mm. The point density of the scan was 255 by 1000. For the laboratory experiments, all scans were captured within 650 mm of the bank face. Data from the 3-D scanner were used to characterize the hydraulic controls producing a given

seepage mechanism. Scanned images were exported to an ASCII file in terms of the XYZ coordinates of the point cloud. The XYZ coordinates were then used to create 2.0 mm square grids using the inverse to distance power algorithm. A program was developed to compute the eroded volume by subtracting the scanned surface at a given time from the scanned surface of the initial time. An example of the eroded surface by seepage particle mobilization is shown in Figure 2.2.

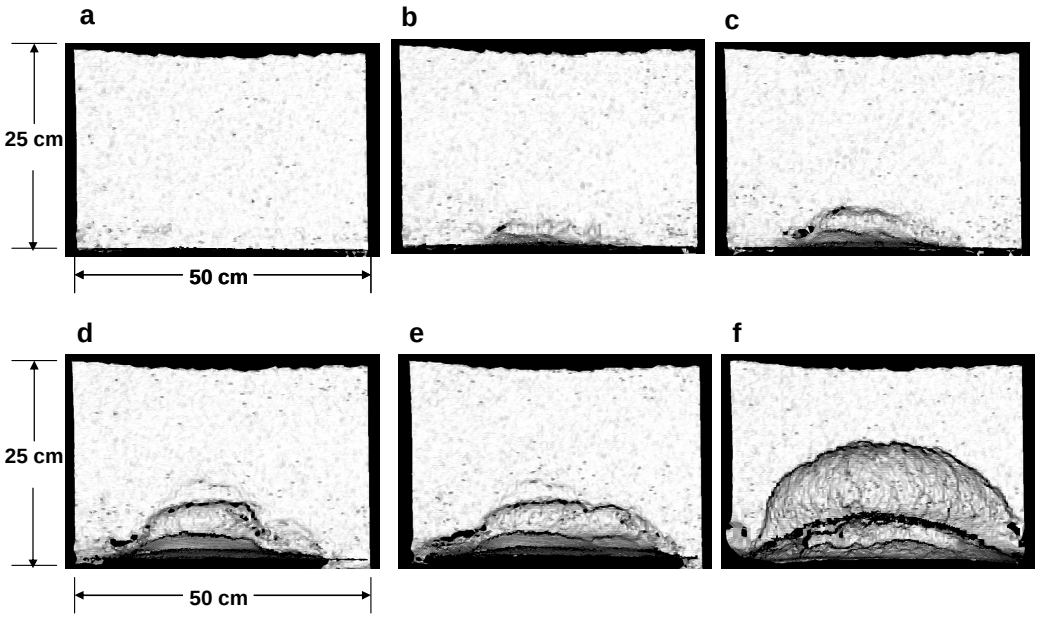

Figure 2.2 Example of the eroded surface by seepage particle mobilization captured using the three-dimensional laser scanner. Each scan represents a different time during the experiment: (a) original bank face, (b) and (c) illustrate the start of the seepage particle mobilization and undercutting, (d) and (e) illustrate continued undercut growth, and (f) illustrates the bank after small-scale sapping failure on the bank slope.

2.3.2 Analysis of Stability with Seepage Gradient Forces

Tension or "pop-out" failures, where the driving static forces exceed the resisting static forces resulting in a block failure with tension crack formation, have been analyzed

by various researchers (i.e., Budhu and Gobin, 1996), primarily by assuming the sediment was non-cohesive. The factor of safety (*FS*) for a cohesionless slope under a steady-state regime was derived by Budhu and Gobin (1996) as:

$$FS = \frac{\left[\left(\frac{\gamma'}{\gamma_w}\right)\cos\alpha' - \sin\alpha'\cot\lambda\right]\tan\phi'}{\left(\frac{\gamma'}{\gamma_w}+1\right)\sin\alpha'} \tag{2.4}$$

where γ' is the submerged unit weight of the soil, γ_w the unit weight of water, α' the bank angle, ϕ' the friction angle, and λ the direction of the seepage vector measured clockwise from the inward normal to the bank slope. The failure plane considered in this equation is parallel to the bank slope. This equation was used to investigate the tension or "pop-out" failure by seepage gradient forces observed in the three-dimensional soil block experiments. Since the direction of the seepage vector was needed in the equation, an uncalibrated two-dimensional seepage model (SEEP/W) was used to predict the direction of the vector within the flow domain using laboratory measured soil hydraulic parameters as functions of the soil ρ_b. The two-dimensional model was assigned a constant head boundary at the inlet and utilized the soil parameters for each experimental setup discussed later.

In general, the simulation showed two possible directions of the steady-state seepage vector: $90 \le \lambda \le 180$ at the inlet and $180 \le \lambda \le 270$ at the drainage face (Figure 2.3). The *FS* was computed using these ranges of λ for the loamy sand and sand with ρ_b equal to 1.50 Mg m^{-3} and 1.30 Mg m^{-3}, respectively. Equation (2.4) consistently predicted failure (i.e., *FS* < 1.0) for $90 \le \lambda \le 180$ (at inlet); however, for $180 \le \lambda \le 270$ at the drainage face, it yielded negative *FS* values which indicated that for cohesionless soil

with $30 \le \alpha' \le 90$ and $180 \le \lambda \le 270$, this equation did not apply; i.e., the failure plane was not parallel to the slope as assumed for these conditions.

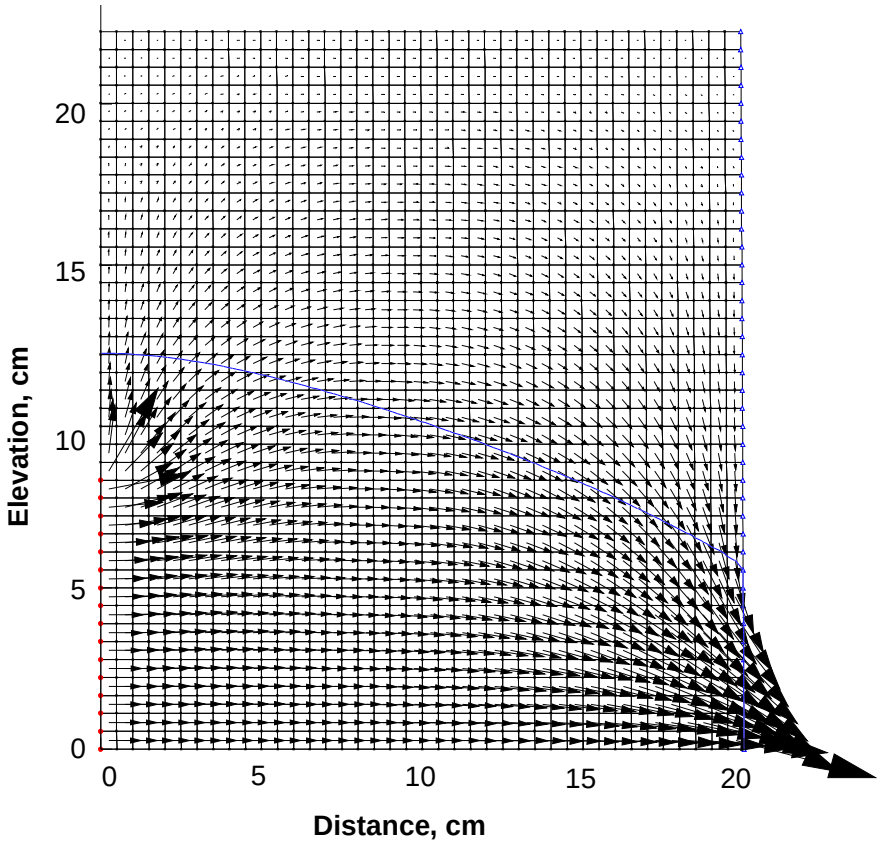

Figure 2.3 Seepage vectors as simulated by SEEP/W for a 90 degree sand bank with an inflow reservoir head of 15 cm and a bulk density, ρ_b, of 1.30 Mg m^{-3}.

For cohesionless dry soil, the maximum stable slope with no external load is its angle of internal friction (Budhu and Gobin, 1996). In the laboratory experiments, the soil block was able to hold the 90 degree slope because of its increased cohesion due to packing, thereby acting as a cohesive soil mass. In order to consider the effects of cohesion, a new FS equation was derived for failure planes perpendicular and parallel to the bank slope to take into account the two possible directions of the seepage vector.

The *FS* is generally defined as the ratio of the resisting forces to the driving forces. The driving forces were the vector components of the seepage force and weight perpendicular to the failure plane, while the resisting forces were equal to the shear strength of the soil defined by Mohr-Coulomb equation. Consider a soil element (Figure 2.4) with unit width.

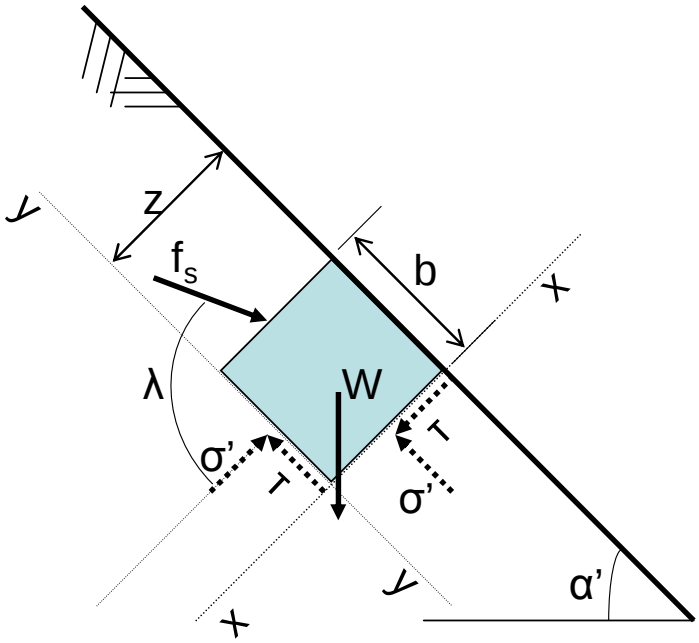

Figure 2.4 Free-body diagram of a soil element subjected to seepage gradient forces considering two possible failure planes, *yy* and *xx*. *W* is the weight of the soil element; σ' is the effective normal force; τ is the shear stress; f_s is the seepage force on the element; α' the bank angle; λ is the direction of the seepage vector measured clockwise from the inward normal to the bank slope; *z* is the width of the failure block; and *b* is the height of the failure block.

At failure plane *y-y*, the *FS* can be written as the ratio of the shear strength of the soil ($c' A_s + \sigma' \tan\phi'$) divided by the sum of the weight and seepage forces parallel to the failure plane (*y-y)*, i.e., $W \sin\alpha' + f_s \sin\lambda$:

$$FS = \frac{c' A_s + \sigma' \tan\phi'}{W \sin\alpha' + f_s \sin\lambda} \tag{2.5}$$

where *c'* is the cohesion, A_s is the sheared area, σ' is the effective normal force which is the resultant of the forces acting perpendicular to the failure plane (*y-y)*, *W* is the weight of the soil element and f_s is the seepage force on the element. For plane *y-y*, the effective normal force is

$$\sigma' = W \cos\alpha' - f_s \cos\lambda \tag{2.6}$$

where *W* and f_s are given by:

$$W = \gamma' V \tag{2.7}$$

$$f_s = i\gamma_w V \tag{2.8}$$

where *i* is the magnitude of the hydraulic gradient (i.e., $\sin\alpha' / \sin\lambda$) and *V* is the volume of the soil element. Substituting equations (2.6), (2.7), and (2.8) into equation (2.5) results in the following:

$$FS = \frac{c' A_s + \left(\gamma' V \cos\alpha' - i\gamma_w V \cos\lambda\right)\tan\phi'}{\gamma' V \sin\alpha' + i\gamma_w V \sin\lambda} \tag{2.9}$$

Dividing through by *V* and γ_w, the *FS* equation along failure plane *y-y* is given by:

$$FS = \frac{\dfrac{c'}{z\gamma_w} + \left(\dfrac{\gamma'}{\gamma_w}\cos\alpha' - \sin\alpha'\cot\lambda\right)\tan\phi'}{\left(\dfrac{\gamma'}{\gamma_w} + 1\right)\sin\alpha'} \tag{2.10}$$

where A_s in a two-dimensional model is represented by the linear distance *z*, which corresponds to the distance from the bank face to the failure plane. Similarly, the factor of safety along failure plane *x*-*x* can be written as:

$$FS = \frac{c' A_s + \sigma' \tan \phi'}{f_s \cos \lambda - W \cos \alpha'} \tag{2.11}$$

where $\sigma' = W \sin \alpha' + f_s \sin \lambda$. The *FS* can then be written as:

$$FS = \frac{\dfrac{c'}{b\gamma_w} + \left(\dfrac{\gamma'}{\gamma_w} + 1 \right) \sin \alpha' \tan \phi'}{\sin \alpha' \cot \lambda - \dfrac{\gamma'}{\gamma_w} \cos \alpha'} \tag{2.12}$$

where A_s in a two-dimensional model is represented by the linear distance *b*, which corresponds to the height of the bank.

Equations (2.10) and (2.12) were used to compute the *FS* at two sections in the flow domain: close to the inlet where $90 \le \lambda \le 180$ and near the drainage face where $180 \le \lambda \le 270$. For equation (2.10), *z* was assumed to be 0.20 m because tension cracks were observed to form at that section of the soil block when tension or "pop-out" failure occurred. For equation (2.12), *b* was assumed equal to 0.20 m, which was where the maximum seepage vector emerged from the bank. The *FS* was also computed for the same hydraulic conditions (i.e. same *H* and α') but different ρ_b in order to explain the occurrence of tension or "pop-out" failure.

2.3.3 Trends in Seepage Erosion and Undercutting

For cases with seepage particle mobilization and undercutting, the shape of the eroded surface was investigated for each of the seepage undercut. A five parameter Gaussian function was fitted to the data:

$$z(x,y) = d_u \exp\left[-\left\{\left(\frac{x-x_o}{\sigma_x}\right)^2 + \left(\frac{y-y_o}{\sigma_y}\right)^2\right\}\right] \quad (2.13)$$

where $z(x,y)$ is the measured seepage undercut from the original bank face, d_u is the depth or maximum distance of seepage erosion, x_o and y_o is the center of the depth, and σ_x and σ_y are spreads of the seepage undercut. The variables σ_x and σ_y are related to the full width at half-maximum ($FWHM_j$) of the Gaussian function:

$$FWHM_j = 2\sqrt{2\ln(2)}\sigma_j \quad (2.14)$$

where j is either x or y (Weisstein, 1999). This function was selected because the five parameters could be estimated from measurable characteristics of the undercut.

Each image generated from the scanner was used to identify the initial mode of erosion: unimodal or multimodal. Unimodal erosion represents undercutting that is focused at a single point on the bank face whereas multimodal represents erosion that initiated at more than one location. With this data, trends were investigated between the depth and width of undercutting as functions of soil type, ρ_b, α', and H.

2.3.4 Soil Property Analysis

For the two soils investigated in this research, samples extracted from the soil block setup (sampled in triplicate) were analyzed in the laboratory to determine particle size distribution and soil hydraulic properties (saturated hydraulic conductivity, K_s, and the soil water retention curve parameters) relative to ρ_b. Particle size analysis was determined by sieve analysis for particles larger than 0.075 mm and the hydrometer method for particles less than 0.075 mm (*ASTM Standards* D422-63).

The saturated hydraulic conductivity, K_s, was determined on extracted soil cores with bulk densities of 1.30, 1.45, and 1.60 Mg m^{-3} for the sand and 1.50, 1.60, and 1.70

Mg^{-3} for the loamy sand using a falling head permeameter. The K_s was computed by fitting the measured head loss at time t to the following equation (McWhorter and Sunada, 1977):

$$K_s = \frac{a_p L}{A_{sc} t} \ln \frac{\Delta h_0}{\Delta h(t)} \tag{2.15}$$

where L is the length of the sample, A_{sc} is the horizontal area of the soil column, a_p the horizontal area of the piezometer, Δh_0 is the initial head (at $t = 0$), and $\Delta h(t)$ is the head at time t.

Water retention was determined on the extracted soil cores using standard test methods (*ASTM Standards* D3152 and D2325). Water retention data were modeled with RETention Curve (RETC) with the van Genuchten equation using the Mualem assumption (van Genuchten *et al.*, 1991):

$$\theta(h) = \begin{cases} \theta_r + \dfrac{\theta_s - \theta_r}{\left[1 + |ah|^n\right]^m} & h < 0 \\ \theta_s & h \geq 0 \end{cases} \tag{2.16}$$

$$K(h) = K_s S_e \left[1 - (1 - S_e^{1/m})^m\right]^2 \tag{2.17}$$

where S_e is the effective saturation; a (L^{-1}) and n are empirical parameters; $m = 1\text{-}1/n$; θ_s is the saturated water content; θ_r is the residual water content; and h the pressure head. These soil hydraulic parameters were used in the SEEP/W modeling for deriving the seepage vector direction.

Samples were also analyzed to determine geotechnical properties: effective cohesion (c') and internal angle of friction (ϕ'). The strength properties of the soil used in the experiments were determined using a direct shear test (*ASTM Standards* D3080-98). The shear strength was measured under unsaturated moisture conditions mimicking

the condition of the packed soil block. Samples were prepared by compacting the soil to a given ρ_b. Three test specimens for each soil type and ρ_b were tested under different normal loads (4.0 kg, 6.0 kg, and 10.0 kg). For a given normal force, the maximum shear stress was determined from the peak of shear stress versus horizontal deformation curve. The soil strength parameters (c' and ϕ') were derived from Mohr's failure envelope.

2.4 RESULTS AND DISCUSSION

2.4.1 Soil Physical, Hydraulic, and Geotechnical Characterization

Hydraulic and geotechnical characteristics are documented in Tables 2.1-2.3 for both the sand and loamy sand soils at the various ρ_b investigated in this research. The entry pressure head, a, for the loamy sand was less than a for the sand (Table 2.2) and the loamy sand soil possessed a one order of magnitude lower K_s than the sand (Table 2.3). The van-Genuchten curve fit parameters a, n, and θ_r appeared independent of ρ_b, while θ_s and K_s increased with decreased ρ_b (Tables 2.2 and 2.3). For example, the K_s for the sand soil at ρ_b = 1.60 Mg m^{-3} was almost four times less than K_s at ρ_b = 1.30 Mg m^{-3} (Table 2.3). The c' and ϕ' were both functions of the soil ρ_b: both c' and ϕ' linearly increased with increased ρ_b (Table 2.4). In fact, the "best-fit" linear trend lines between c' and ρ_b for the sand and loamy sand soils had an R^2 = 0.80 and 0.85, respectively.

Table 2.1 Particle size distribution and mean particle size (d_{50}, mm) for the two soils used in the soil block experiments.

Soil Texture	% Sand	% Silt	% Clay	d_{50}, mm
Sand	99.3	0.7	0.0	0.33
Loamy Sand	84.5	13.4	2.1	0.24

Table 2.2 Soil water retention curves estimated using RETC based on pressure plate experiments for the sand and loamy sand soils at the bulk densities used in the soil block experiments.

Soil Type	ρ_b (Mg m^{-3})	θ_r (cm^3 cm^{-3})	θ_s (cm^3 cm^{-3})	α (cm^{-1})	n	R^2
Sand	1.60	0.05 (0.01)	0.40 (0.00)	0.031 (0.010)	1.33 (0.04)	0.94
Sand	1.45	0.05 (0.01)	0.46 (0.00)	0.026 (0.002)	1.28 (0.02)	0.96
Sand	1.30	0.06 (0.03)	0.51 (0.00)	0.048 (0.018)	1.22 (0.03)	0.92
Loamy Sand	1.70	0.06 (0.03)	0.36 (0.00)	0.019 (0.003)	1.33 (0.16)	0.96
Loamy Sand	1.60	0.04 (0.00)	0.40 (0.00)	0.026 (0.012)	1.23 (0.06)	0.94
Loamy Sand	1.50	0.04 (0.00)	0.43 (0.01)	0.017 (0.011)	1.27 (0.05)	0.90

Note: Reported values are averages of three replicates (standard deviations given in (parenthesis)

Table 2.3 Saturated hydraulic conductivity (K_s) measured using constant-head permeameter test for varying bulk densities of the sand and loamy sand soils.

Soil Type	ρ_b (Mg m^{-3})	K_s, (cm s^{-1})
Sand	1.60	0.0077
	1.45	0.0176
	1.30	0.0284
Loamy Sand	1.70	0.0006
	1.60	0.0012
	1.50	0.0034

Table 2.4 Geotechnical properties (effective cohesion, and internal angle of friction) of the sand and loamy sand soils.

Soil Type	ρ_b (Mg m^{-3})	c' (kPa)	φ'
Sand	1.60	3.4	40.6
	1.45	2.0	38.4
	1.30	0.5	26.5
Loamy Sand	1.70	7.4	41.9
	1.60	4.9	39.1
	1.50	2.5	36.2

2.4.2 Seepage Mechanisms: Erosion and Undercutting versus Tension/"Pop-out" Failures

The ρ_b for the two different soil types (i.e., sand and loamy sand) controlled the primary seepage mechanism of the failure process. Seepage resulted in an eventual bank collapse either through (1) tension or "pop-out" failures when the force of the seepage was greater than the resistance of the soil that further decreased as a result of reduced shear strength from increased soil pore-water pressure, and (2) particle mobilization (i.e., seepage erosion) and bank undercutting when the seepage force gradient was less than the initial resisting force of the soil block with eventual bank collapse due to the combined forces from seepage and the buildup of pore-water pressure (Table 2.5).

Table 2.5 Observed seepage erosion volume (V_{SE}), volume (V_{BF}) of soil loss by bank failure, and depth or maximum distance of undercutting (d_u) prior to bank collapse, relative to experimental soil block conditions (α' = bank angle, H = inflow water reservoir head, and ρ_b = soil bulk density).

		Sand				Loamy sand			
α' (degrees)	H (cm)	ρ_b (Mg m^{-3})	d_u (cm)	V_{SE} (cm^3)	V_{BF} (cm^3)	ρ_b (Mg m^{-3})	d_u (cm)	V_{SE} (cm^3)	V_{BF} (cm^3)
90	15	1.60	4.9	592	6672	1.70	6.1	1448	6145
		1.45	4.9	475	6465	1.60	2.3	130	5235
		1.30	PO	PO	5727	1.50	PO	PO	4811
						1.45	PO	PO	6134
						1.30	PO	PO	4711
90	25	1.60	6.3	781	6354	1.70	3.0	221	3285
		1.45	4.2	252	6560	1.60	3.4	282	2975
90	35	1.60	4.3	183	6609	1.70	1.5	26	3807
		1.45	3.0	141	NA †	1.60	3.1	180	5574
75	15	1.60	6.2	867	4870	1.70	5.2	937	4666
		1.45	2.5	94	4185	1.60	3.4	305	4239
		1.30	PO	PO	NA				
75	25	1.60	6.2	800	5996	1.70	3.5	345	2856
		1.45	2.9	177	3325	1.60	3.6	333	3693
75	35	1.60	5.8	577	5791	1.70	2.8	216	3429
		1.45	2.8	143	2924	1.60	2.6	213	4409
60	15	1.60	6.5	1137	5842	1.70	6.7	1492	5348
		1.45	4.4	437	4713	1.60	6.2	846	4966
60	25	1.60	6.6	814	5082	1.70	3.8	306	3366
		1.45	6.0	744	5034	1.60	5.3	288	4117
60	35	1.60	5.6	508	4422	1.70	5.8	1191	4196
		1.45	7.0	198	5170	1.60	4.4	626	3650

Values are averages of at least duplicate experiments. * PO: Tension or "pop-out" failure due to pore-water pressure gradient without seepage undercutting.
† Data not collected during the experiment.

For these experimental conditions, changes in the ρ_b did not significantly influence the $\frac{\partial \psi}{\partial y}$ in the soil profile and correspondingly the seepage force, as will be discussed below. However, decreasing the ρ_b decreased the resistance of the soil by reducing the total normal stress, *c'* and ϕ' as shown in Table 2.4. This reduction in the resistance of the soil varied based on soil type and along with variability in the driving forces controlled the critical point at which the force of failure became greater than the force of resistance. When the resistive forces are equal to the driving forces without undercutting, pop-out failure occurs. The *x*-intercept in Figure 2.5 corresponded to the ρ_b (therefore the combination of *c'* and ϕ') at which the resistive forces became equal to the driving forces without undercutting. Tension or "pop-out" failures due to seepage gradient forces were observed for all experimental conditions (i.e., *H* of 15, 25, and 35 cm and α' of 90, 75, and 60 degrees) when the ratio of the bulk density to the soil grain density, ρ_b/ρ_s (where ρ_s was assumed to be 2.65 Mg m^{-3} to provide a convenient way to non-dimensionalize the ρ_b), of the sand was less than 0.49. For the loamy sand, the critical ρ_b/ρ_s between the two failure mechanisms was approximately 0.58 (Figure 2.5). Results were consistent among duplicate experiments for each set of experimental conditions. We hypothesize that greater partially saturated weight (i.e., total weight) was present along the failure plane in the loamy sand soil because of the greater residual moisture content at packing, lower K_s, and lower *a* (i.e., higher entry pressure head). This greater partially saturated or total weight in the loamy sand soil led to higher driving forces and less resistive strength as the partial saturation reduced the apparent cohesion. Because the driving force and reduced apparent cohesion were lower for the sand as

compared to the loamy sand, the threshold for observed seepage undercutting was reached earlier in the sand (Figure 2.5).

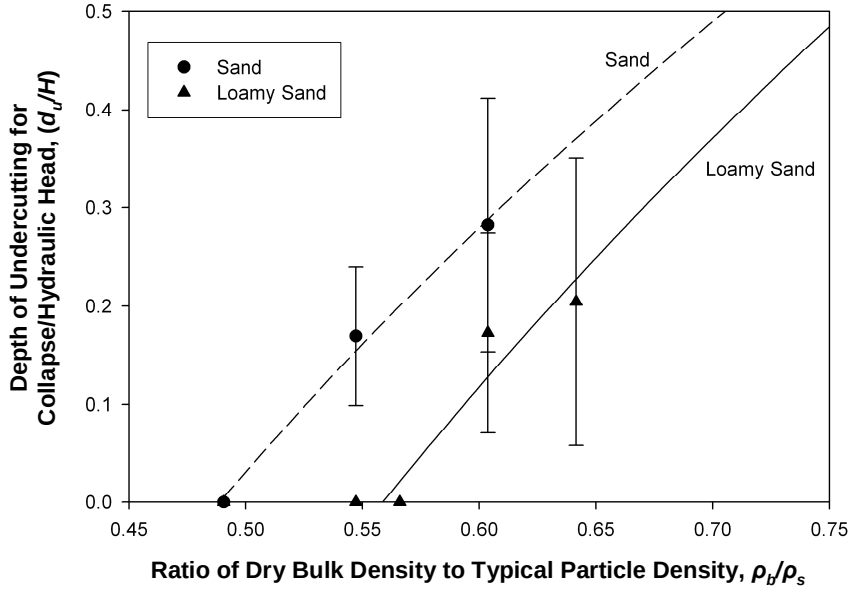

Figure 2.5 Relationship between maximum depth of undercutting, d_u, required for a bank failure and the bulk density (ρ_b) nondimensionalized by the particle density (ρ_s) of the soil. The symbols represent the averages relative to varying bank slope and water head for each soil type.

For higher ρ_b and therefore higher resistive strength beyond this critical ρ_b/ρ_s, the amount of resistive force exceeded the driving force and a stable bank developed. This stable bank did not fail unless undercutting also occurred. Therefore, for these experiments, particle mobilization and undercutting generally occurred under cases of higher ρ_b because of the increased initial bank resistance to the seepage force. Chu-Agor et al. (2008b) demonstrated that seepage undercutting exponentially reduced the bank stability with increased depth, d_u, which in this research eventually led to cantilever failures due to seepage particle mobilization and the induced moment by undercutting. It

is expected that for exceedingly higher H (i.e., greater than 35 cm), pop-out failure would be observed at greater ρ_b because of the overriding affect of seepage gradient forces.

It is hypothesized that the critical ρ_b/ρ_s will increase for soil types with greater clay content and therefore greater c', dependent on changes in the ρ_b relative to soil type. Considering this hypothesis, the occurrence of these immediate collapses, referred to as tension or "pop-out" failures, precludes bank failure by seepage erosion and undercutting being observed in the field. For the noncohesive seepage layers observed in the field by Wilson et al. (2007), the ρ_b for the loamy sand was reported to be 1.50 Mg m^{-3} (i.e., ρ_b/ρ_s = 0.57), which occurred near the boundary of tension or "pop-out" failures observed in this research. They observed seepage undercutting by mobilization of soil particles but did not observe the bank failures in progress in situ. They did observe post-failure evidence of undercutting by seepage erosion in situ. It is possible that these stream banks also experienced tension or "pop-out" failures given the hydraulic gradients imposed on the sediment. The stream restoration project reported by Lindow et al. (2007) was undermined due to bank collapses hypothesized to be due to seepage. Due to the cohesions of the banks (i.e., 10.7 to 17.7 kPa), particle mobilization by seepage flow was probably limited. Instead, Lindow (2007) observed in two-dimensional lysimeter experiments with a repacked bank (10-cm of sand at ρ_b = 1.30 Mg m^{-3} underlying 15-cm of sandy clay loam) that the tension or "pop-out" failures of this underlying layer eventually led to undermining of the entire bank.

For cases where seepage undercutting occurred, the depth of undercutting required for a bank collapse was most dependent on the soil ρ_b as compared to α' or H for these experimental conditions (Figure 2.5). The error bars shown in Figure 2.5

represent variability due to the imposed inflow H and α'. For experiments with the same soil type, α' and H, the required d_u, which generally fell within the range of 2.0 to 7.0 cm, decreased as the ρ_b decreased (Table 2.5) due to the corresponding decrease in the bank's resistive force (i.e., c') (Table 2.4). Correspondingly, the cumulative volume of seepage erosion required to cause bank failure decreased as the ρ_b decreased (Table 2.5). The loamy sand soil generally required equivalent to slightly lower depths of undercutting for bank collapse than the sand experiment based on experiments with the same ρ_b (i.e, 1.60 Mg m^{-3}), α' (90, 75, and 60 degrees), and H (15, 25 and 35 cm). This effect was most likely due to the approximately equivalent c' for the two soils when packed to the same ρ_b (i.e, 1.60 Mg m^{-3}). Therefore, sediment transport models for seepage erosion should include an explicit consideration for the ρ_b of the noncohesive sediment. The sediment transport functions of Howard and McLane (1988) and Fox et al. (2006) include an empirical packing coefficient, along with the K_s, that implicitly account for ρ_b.

As expected due to the lower ρ_b, the time for bank failure in experiments with tension or "pop-out" failures was shorter than the time of failure for experiments with seepage particle mobilization. For experiments on the same soil with equivalent α' and ρ_b, an increase in H generally resulted in less seepage erosion and correspondingly lower amplitudes required for bank failure (Table 2.5). The increased H theoretically resulted in greater soil pore-water pressures in the overlying topsoil which reduced the shear strength of the soil. These results mimic those of Fox et al. (2006, 2007a, 2007b) and Wilson et al. (2007) in that seepage particle mobilization and increased soil pore-water pressure were both important processes leading to bank failures. As α' decreased for a particular ρ_b and

H, the amplitude of the seepage undercut required for bank collapse increased. This result was fundamentally obvious since lower α' resulted in initially more stable banks (higher factor of safety), requiring a greater amplitude of seepage undercut to cause a failure (Chu-Agor et al., 2008b).

No significant differences (significance level of 0.05) were observed between the mass and volumes of collapsed banks for tension or "pop-out" failures as compared to seepage undercutting (Table 2.5). For the sand soil, the average volume of bank collapse by tension or "pop-out" failure (i.e., three experiments with ρ_b equal to 1.30 Mg m^{-3}) was 5727 cm^3 compared to 5373 cm^3 for the seepage undercut banks (P-value = 0.72). The mass of collapsed sand banks by tension or "pop-out" failures was 7.5 kg compared to 8.3 kg for seepage undercut banks (P-value = 0.60). For the loamy sand, the average volume of tension or "pop-out" failures (i.e., four experiments with ρ_b less than 1.50 Mg m^{-3}) was 5092 cm^3 compared to 4220 cm^3 for seepage particle mobilization and undercutting (P-value = 0.11). The average mass of tension or "pop-out" failures was 7.1 kg compared to 7.0 kg for seepage particle mobilization and undercutting (P-value = 0.88).

The phase diagram of Lobkovsky et al. (2004) developed for small α' (i.e., α' < 12 degrees) suggests that α' greater than 12 degrees will always experience slumping. This was also verified by our laboratory experiments. The uniqueness of this research was that the mechanism of the slumping (i.e., particle mobilization and undercutting versus tension or "pop-out" failure) was highlighted relative to the soil characteristics. Existing slope stability equations for Coulomb failure of noncohesive slopes should be able to predict failures by seepage forces if banks truly behave as noncohesive and bank

angles are less than the angle of internal friction. However, bank stability analyses capable of modeling seepage particle mobilization and undercutting due to seepage erosion are limited. Some work has been done on the effect of the change in the geometry of the bank due to undercutting on bank failure such as the static analyses reported by Wilson et al. (2007) and the step-wise dynamic analysis by Chu-Agor et al. (2008b). However, fully integrated variably saturated flow model with a dynamic geometric and geotechnical model to predict bank failure is still lacking.

2.4.3 Analysis of Stability with Seepage Gradient Forces

The theoretical *FS* for non-cohesive and cohesive banks verified the experimental observations in Figure 2.5. Tension or "pop-out" failures occurred when a critical failure plane with $FS < 1.0$ developed within the flow domain. In the soil block experiments, the critical failure plane was located close to the inlet where the seepage force was directed upward. Upward seepage force reduced the effective normal force on the soil, resulting in lower soil shear strength. The magnitude of the seepage force and the reduced cohesion due to lower ρ_b were the reasons for the tension or "pop-out" failure observed in the soil block experiments.

Table 2.6 shows the computed *FS* with and without cohesion at two different locations in the flow domain. When cohesion was not considered, the banks were unstable for most values of λ. However, the soil used in the experiment was cohesive because of packing effects. The measured *c'* and ϕ' were found to be dependent on the ρ_b. Therefore, a cohesionless assumption did not represent the condition of the soil used in this experiment.

Table 2.6 Factor of safety (*FS*) for the sand (S) and loamy sand (LS) banks computed at two different locations in the flow domain. Close to the inlet, the seepage vector is directed at $90 \leq \lambda \leq 180$ and the valid failure plane is *y-y* (see Figure 2.4).

Bank	ρ_b (Mg m^{-3})	α' (^{o})	c' (kPa)	φ' (^{o})	Observed Seepage Mechanism	*FS* at Inlet – Equation (2.10) (Maximum λ, degrees)	*FS* at Outlet – Equation (2.12) (Maximum λ, degrees)
S	1.3	90	0.0	26.5	PO*	0.23 (130)	0.52 (210)
	1.3	75	0.0	26.5	PO	0.38 (140)	0.61 (210)
	1.45	90	0.0	38.4	SU**	0.35 (130)	0.87 (210)
	1.6	90	0.0	40.6	SU	0.36 (130)	0.99 (210)
S	1.3	90	0.5	26.5	PO	0.38 (130)	0.68 (210)
	1.3	75	0.5	26.5	PO	0.52 (140)	0.78 (210)
	1.45	90	2.0	38.4	SU	0.89 (130)	1.47 (210)
	1.6	90	3.4	40.6	SU	1.22 (130)	1.98 (210)
LS	1.5	90	0.0	36.2	PO	0.32 (130)	0.83 (210)
	1.6	90	0.0	39.1	SU	0.34 (140)	0.94 (210)
	1.7	90	0.0	41.9	SU	0.37 (130)	1.06 (210)
LS	1.5	90	2.5	36.2	PO	0.98 (130)	1.56 (210)
	1.6	90	4.9	39.1	SU	1.60 (140)	2.36 (210)
	1.7	90	7.4	41.9	SU	2.20 (130)	3.24 (210)

Close to the drainage face, the seepage vector is at $180 \leq \lambda \leq 270$ and the valid failure plane is *x-x* (see Figure 2.4). Lambda (λ) is approximated from maximum seepage vector simulated by the two-dimensional seepage model (SEEP/W).
* PO = Tension or "pop-out" failure.
** SU = Failure included seepage particle mobilization and undercutting.

When cohesion was considered, sand at ρ_b = 1.30 Mg m^{-3} was unstable close to the inlet but stable close to the drainage face. The instability close to the inlet caused the tension or "pop-out" failures observed during the experiments. The bank collapsed before seepage erosion undercutting could initiate. At ρ_b = 1.45 Mg m^{-3}, there were some values of λ which could also result in tension or "pop-out" failure. However, during the

experiment, the gradient may have been lower than the limiting value of λ for instability, causing the bank to hold until the initiation of seepage erosion.

The loamy sand showed consistent stability at both locations except for ρ_b = 1.50 Mg m^{-3} close to the inlet which could be unstable if $\lambda \leq 130$ degrees. Simulations from the two-dimensional model predicted a λ of approximately 130 degrees for the maximum seepage vector close to the inlet. Banks with ρ_b equal to 1.60 Mg m^{-3} and 1.70 Mg m^{-3} on the other hand were stable at both locations causing the bank to hold until seepage erosion undercutting initiated.

2.4.4 Unimodal versus Multimodal Seepage Erosion Undercuts

For cases in which the seepage process was by seepage erosion and undercutting, it was observed during the experiments that seepage erosion could initiate as a unimodal undercut in which erosion was concentrated at one location on the bank face or as a multimodal undercut in which erosion initiated at different locations on the bank face. Results were consistent among duplicate experiments for each set of experimental conditions. A typical time sequence demonstrating the changes in the seepage undercut as seepage erosion progressed is shown in Figure 2.6 for the case of a unimodal undercut. Also shown is the Gaussian fit for these specific undercuts. The strength of the fit, quantified through calculation of the coefficient of determination, or R^2, was greater in cases where the seepage erosion undercuts initiated at one location on the bank face.

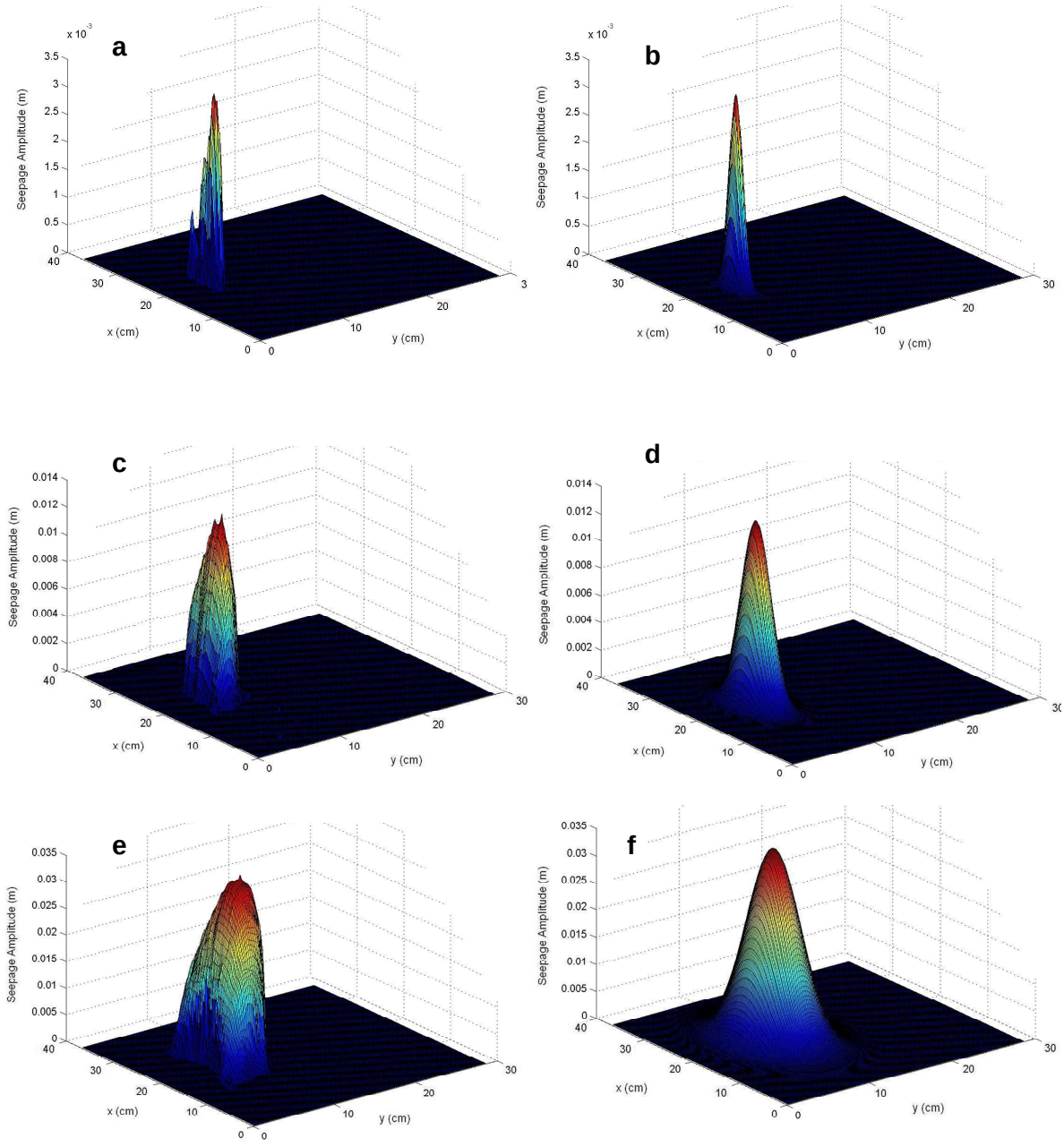

Figure 2.6 Typical time sequence of seepage erosion undercut formation. Note that the *x*-*y* plane is the bank face. Example shown is for the case of a 90 degree sand bank, 35 cm water head with ρ_b = 1.60 Mg m^{-3}. (a) t = 108 s after flow arrival, (b) Gaussian fit for t = 108 s (R^2 = 0.80), (c) t = 125 s after flow arrival, (d) Gaussian fit for t = 125 s (R^2 = 0.77), (e) t = 149 s after flow arrival, and (f) Gaussian fit for t = 149 s (R^2 = 0.78).

It was hypothesized that multimodal undercuts would form in experiments with lower α', lower ρ_b, and lower inflow H. However, for these experimental conditions, the mode of initial seepage erosion undercutting was controlled by α'. A 90 degree bank, regardless of the H, ρ_b, and soil type, started with unimodal erosion while banks with α' of less than 90 degrees (i.e., 75 and 60 degrees) started with multimodal erosion. The 90 degree banks manifested in initial unimodal undercuts horizontally centered along the bank face while the 75 and 60 degree banks started with multimodal undercuts which initiated at random locations within the seepage layer (Figure 2.7), with the locations potentially corresponding to micro-scale preferential flow features created during packing.

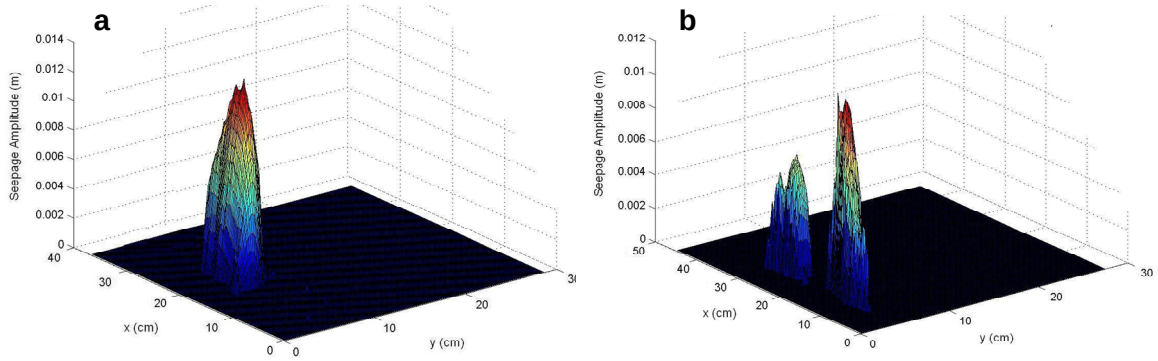

Figure 2.7 Example of (a) unimodal and (b) multimodal seepage erosion undercuts. Note that the x-y plane is the bank face. The unimodal figure is for the case of loamy sand with 90 degree bank, 35 cm head, and 1.60 Mg m^{-3} bulk density. The bimodal figure is for the loamy sand with 75 degree bank, 15 cm head, and 1.70 Mg m^{-3} bulk density.

The multimodal undercuts generally converged into unimodal undercuts, with this convergence time hypothesized to depend on soil type, ρ_b, α', and inflow H. For α' less than 90 degrees, convergence was identified from the scanned images and was verified

using the regression coefficient from the fit of the Gaussian function to the three-dimensional undercut shape. An R^2 of at least 0.70 was used as an identifier for convergence. The time for the multimodal undercuts to converge to a concentrated unimodal erosion undercut was prominently controlled by the inflow *H*. The higher the *H* the less time it took for convergence to occur for both soil types at different ρ_b (Figure 2.8). Contrary to initial hypotheses, convergence time was more dependent on α' than ρ_b for the range of ρ_b investigated in this research. Convergence times as a function of *H* were approximately equivalent for the same soil with different ρ_b but the same α'. Once converged, the resulting unimodal undercut possessed greater lateral spreads (i.e., larger σ_x), sometimes extending the entire width of the bank face

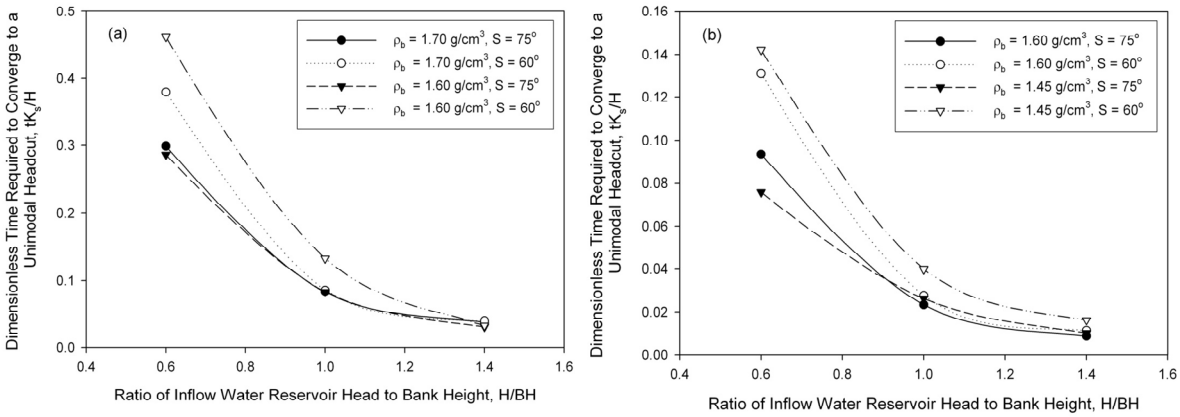

Figure 2.8 Time required for multimodal seepage particle mobilization undercuts for (a) sand and (b) loamy sand soils to reach unimodal undercut, nondimensionalized by the saturated hydraulic conductivity, K_s, and the water inflow reservoir head, *H*.

2.4.5 Trends in Seepage Erosion Undercut Shapes

For a given undercut depth (d_u), the width of the undercut (i.e., σ_x) was approximately an order of magnitude greater than the height (i.e., σ_y) of the undercut

(Figure 2.9). At a given d_u, slightly larger σ_x and σ_y were observed for the loamy sand as compared to the sand soil due to the cohesive strength of the materials. Regression curves through the σ_y- d_u data demonstrated similar power-curve relationships for the sand and loamy sand soils. Statistical tests based on nonlinear analysis of covariance (Hinds and Milliken, 1987) suggested no significant difference between the d_u-σ_y relationships for the two soil types (F-value of 2.00, P-value of 0.16 at a significance level of 0.05).

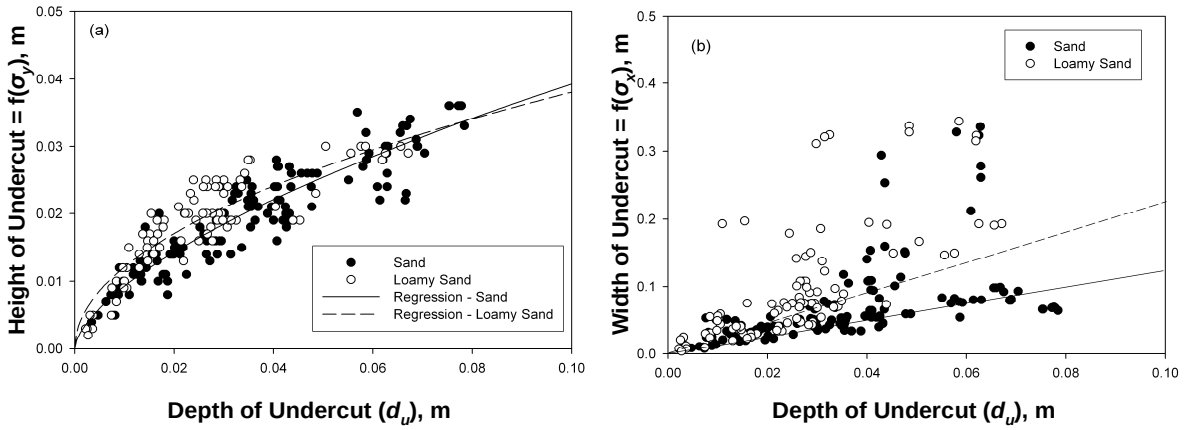

Figure 2.9 Observed relationship between the depth (d_u) of the undercut and the (a) height as quantified by the spread (i.e., σ_y) and (b) width of the undercut (σ_x) for the sand and loamy sand soils. Note that the regression lines shown for σ_x versus d_u are for d_u less than 4 cm.

The σ_x- d_u relationships consisted of greater scatter but still demonstrated a fairly uniform pattern between the two soil types. In fact, the sand soils typically followed a strong linear relationship before experiencing data scatter for d_u > 4 cm. The outliers in σ_x- d_u (Figure 2.9b) corresponded to measurements of large amplitude undercutting just prior to failure during those experiments with greater stability (i.e., higher ρ_b and lower α'). The scatter from a linear trend line started at smaller d_u for the loamy sand soil (i.e.,

d_u > 1 cm). Differences in the d_u -σ_x relationships for the sand and loamy sand soils were less apparent at lower d_u. Statistical tests using analysis of covariance on the d_u-σ_x relationships suggested significant differences between the two soil types (P-value less than 0.001 at significance level of 0.05); however, from a stability perspective, the differences in the predicted widths (i.e., on the order of cm) would not be significant for d_u less than 10 cm.

These common relationships, especially in the σ_y- d_u, were most likely functions of the similar *c*' (i.e., less than 7.5 kPa) and ϕ' (i.e., between 25 and 40 degrees) between the two soils. No apparent dependency of the σ_y- d_u and σ_x- d_u relationships on ρ_b was observed when analyzing the data. These results suggest that it may be possible to use such generalized relationships as a first approximation for inclusion of seepage particle mobilization and undercutting in stability models.

2.5 SUMMARY AND CONCLUSIONS

Seepage mechanisms of hillslope, gully, and streambank instability include: (1) tension or "pop-out" failure and (2) particle mobilization (i.e., entrainment in seepage flow) and bank undercutting. The former occurred when the seepage forces are greater than the soil resistance as well as reduced shear strength from increased soil pore-water pressure. The latter was due to the seepage force gradient being less than the resisting force of the soil block which resulted to bank collapse due to the combined forces from seepage undercutting, seepage forces, and the buildup of pore-water pressure. The first type of failures (tension or "pop-out") have been analyzed from a geotechnical point of view where the driving static forces exceed the resisting static forces resulting in a block failure with tension crack formation, with the necessity of considering cohesion effects

due to packing. The later mechanism occurred when the bank's shear strength was great enough to resist initial tension or "pop-out" failure of the bank. Seepage velocities became greater than critical velocities necessary for particle mobilization leading to particle entrainment in the seepage flow, undercutting and bank collapse. The undercutting acted in conjunction with reduced shear strength due to increased soil pore-water pressure and the seepage force due to the hydraulic gradient. Within a specific soil type, the occurrence of these mechanisms was largely controlled by the soil's bulk density, which directly influenced the hydraulic conductivity, effective cohesion, internal angle of friction, and critical shear stress.

For banks experiencing seepage particle entrainment and undercutting, the slope of the bank predominately influenced the undercutting formation. For these experimental conditions, unimodal undercuts were observed throughout the experiment for banks with 90 degree slopes. On banks with smaller slopes, the undercuts generally initiated as multimodal, eventually converting to a unimodal undercut sometime before bank failure and controlled largely by the hydraulic gradient and the bulk density.

Relationships were developed between the amplitude, width, and height of the undercut for both the sand and loamy sand soils investigated in this research. A power law relationship was observed between amplitude and height with the relationship fairly equivalent for both soils. Differences in soil type were more prevalent in the relationships between amplitude and width. While the differences (i.e., on the order of cm) between soil types were statistically significant, it is hypothesized that they would not be significant from a stability perspective. These generalized relationships could be used to predict the width and height of the undercut based on a priori knowledge of the

amplitude. The fact is important for the eventual incorporation of this seepage mechanism into stability models.

CHAPTER 3

Sediment Transport Function Predicting Seepage Erosion Undercutting for Bank Failure Prediction[3]

3.1 ABSTRACT

Seepage erosion is an important factor in hillslope instability and failure. However, predicting erosion by subsurface flow or seepage and incorporating its effects into stability models remains a challenge. Limitations exist with all existing seepage erosion sediment transport functions, including neglecting the three-dimensional geometry of the seepage undercut and the cohesive nature of soils. The objective was to develop an empirical sediment transport function that can predict seepage erosion and undercutting with time based on three-dimensional soil block experiments covering a wide range of hydraulic, soil type, slope and bulk density combinations. The transport function was represented by an excess gradient equation (R^2 = 0.54). The critical gradient was predicted by the soil cohesion based on laboratory experiments. Using a three-dimensional Gaussian function, the geometric relationships between the maximum distance and lateral and vertical dimensions of the undercut were then derived. The proposed empirical relationships were able to predict the observed time at which a given

[3] Conference paper at the 2009 EWRI Technical Session, Kansas City, Kansas
Chu-Agor, M.L. , G.A. Fox, G.V. and Wilson. 2009. Sediment Transport Function Predicting Seepage Erosion Undercutting for Bank Failure Prediction. *Proceedings of the American Society of Civil Engineers Environmental and Water Resources Congress 2009*, May 17-21, 2009, Kansas City, MO

amount of undercut developed (R^2 = 0.79). The flow gradient can be used with the derived sediment transport function, the first ever relationship proposed for predicting the dimensions and the geometry of the undercut, to predict the impact of seepage erosion undercutting on hillslope stability. Users only need to input the seepage layer's cohesion, bulk density, and the hydraulic gradient over time in the near bank ground water system.

3.2 INTRODUCTION

One process that initiates mass failure of streambanks is seepage erosion of noncohesive sediment by ground water flow, whereby lateral ground water emerges from the bank and undercuts the bank by removing soil particles (Fox et al., 2006; Fox et al., 2007a, 2007b; Wilson et al., 2007). Prediction of streambank undercutting by seepage erosion (Figure 3.1) remains a challenge. The complexity results from the difficulty in quantifying the soil, hydrologic, and geotechnical mechanisms affecting this phenomenon as well as understanding the interaction between them. To start with, measuring subsurface flow and seepage erosion in the field is difficult (Hagerty, 1991; Rockwell, 2002; Fox et al., 2007; Wilson et al., 2007). Furthermore, the variability and heterogeneity of the porous media add uncertainty to seepage flow and erosion estimation (Hagerty, 1991). According to Sidorchuk (2005), the nature of soil erosion is determined by the interaction between water flow and structured soil. He added that this interaction is stochastic in nature due to the complexity and microscopic scale of the geo-mechanical and electro-chemical forces between particles in the soil and of the velocity oscillations in water flow.

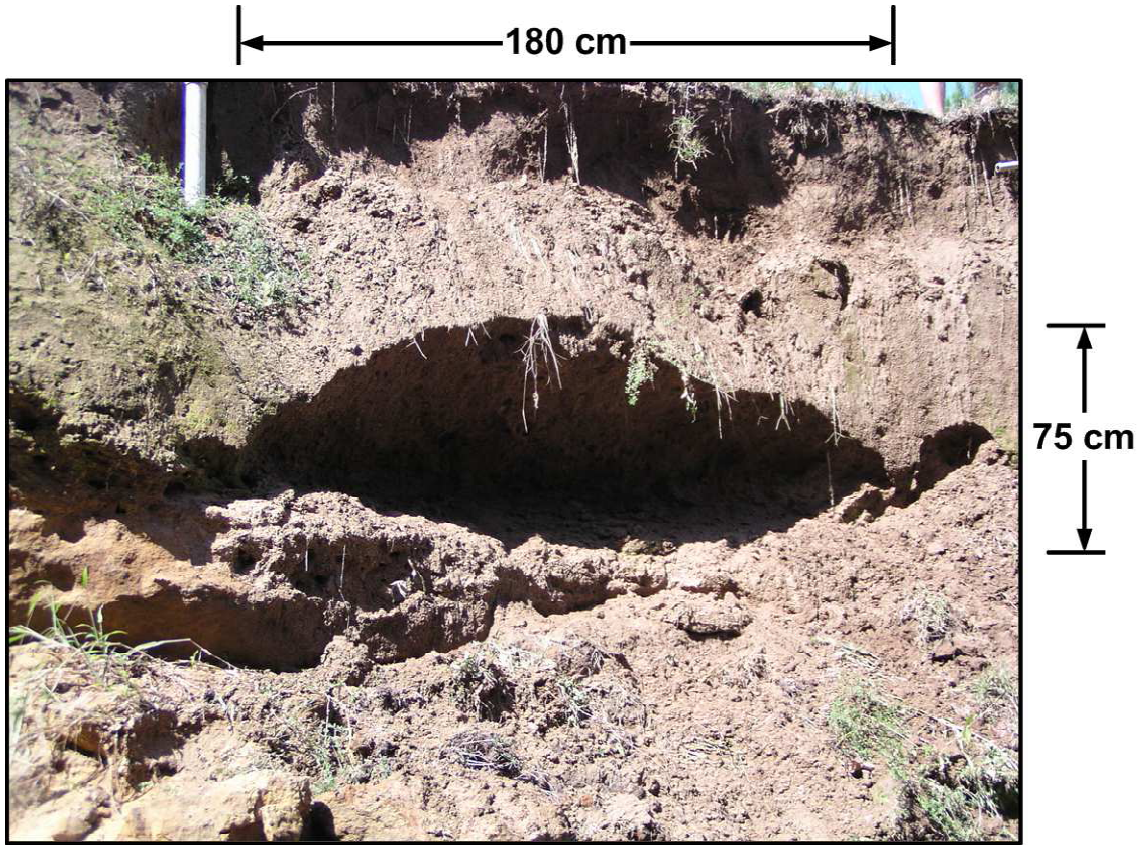

Figure 3.1 Photograph of a seepage erosion undercut on a streambank face along Goodwin Creek in northern Mississippi. This seepage erosion undercut is one of the largest undercuts observed during field experiments reported by Fox et al. (2007) and Wilson et al. (2007).

Another aspect adding to the complexity of seepage erosion analysis is its three-dimensional nature (Crosta and di Prisco, 1999). Since seepage erosion is not uniformly distributed throughout the bank but is commonly isolated to the preferential flow path of the seep (Figure 3.1), the dimensions of the seepage undercut are important in quantifying the amount of sediment eroded. Seepage erosion has not been as extensively studied compared to fluvial erosion other than the seepage influence on the soil pore-

water pressure (Darby and Thorne, 1996; Crosta and di Prisco, 1999; Rinaldi and Casagli, 1999; Simon et al., 1999).

Seepage undercutting has been demonstrated to be an important instability mechanism (Chu-Agor et al., 2008b; Cancienne et al., 2008). Several studies to date have developed relationships that predict sediment transport due to seepage but they neglect the cohesive nature of soils and/or are dependent on empirical coefficients that must be measured in the laboratory for specific soil/packing conditions. Seepage erosion has been analyzed by different researchers as either due to: (1) individual particle mobilization (Lobskovsky et al., 2004; Dunne, 1990; and Howard and McLane, 1988), or (2) small mass failure employing Coulomb's failure mechanism (Chu-Agor et al., 2008a,b; Budhu and Gobin, 1996; and Dunne, 1990), again primarily for noncohesive soils. Sediment transport functions (i.e., Fox et al., 2006 and Howard and McLane, 1988) have also been developed based on laboratory experiments on specific noncohesive soils.

3.2.1 Initiation of Particle Mobilization

Equations for initiation of particle motion attempt to predict the limiting conditions when the seepage force across the grain exceeds the shear strength of the particle resulting in that particle detaching out of its intergranular "pocket" (Dunne, 1990). The mechanics of particle entrainment of noncohesive sediment by seepage was investigated by Howard and McLane (1988). They developed a critical shear stress equation based on the balance of the tractive force due to surface flow, the seepage force and gravity (Figure 3.2). The balance of forces resulted in the following equations:

$$\frac{\tau_c}{(\rho_s-\rho)gd} = C_a \frac{\sin(\beta-\alpha')}{\cos\beta} - C_b \frac{\rho}{\rho_s-\rho}\{1+\tan\beta\tan(\alpha'+\psi)\}\sin\alpha' \qquad (3.1)$$

$$C_a = \frac{2C_3}{3C_1} \tag{3.2}$$

$$C_b = \frac{12C_2}{nC_1} \tag{3.3}$$

where τ_c is the critical shear stress, d is the grain diameter, ρ is the density of the fluid, ρ_s is the density of the sediment, n is the porosity, g is the gravitational acceleration, α' is the bank angle, ψ is the seepage exit angle, β is the angle that the particle makes with another particle, coefficients C_1, C_2, and C_3 are factors which take into account the grain shape and packing effects, and C_a and C_b are constants which can be determined by considering special cases previously analyzed theoretically or experimentally. It is unclear about the typical ranges for these coefficients.

According to Dunne (1990), seepage erosion can occur as fluid particulate transport or mass transport. The former occurs when the fluid stresses cause the particles to lose their frictional strength, and the latter is due to Coulomb failure when the driving forces acting on a soil mass exceed the resisting forces. Dunne used the critical gradient to define the conditions under which each one occurs. For seepage erosion by particle mobilization, he adopted the analysis of Howard and McLane (1988) and others wherein the interaction of surface runoff and exfiltration was evaluated in terms of the balances of forces acting on a single particle (Figure 3.2). The movement for a cohesionless particle occurs when:

$$i > \frac{C_1}{C_2}\frac{(\rho_s - \rho)}{\rho}\frac{\sin(\beta - \alpha')}{\cos(\alpha' + \psi - \beta)} \tag{3.4}$$

where i is the critical gradient.

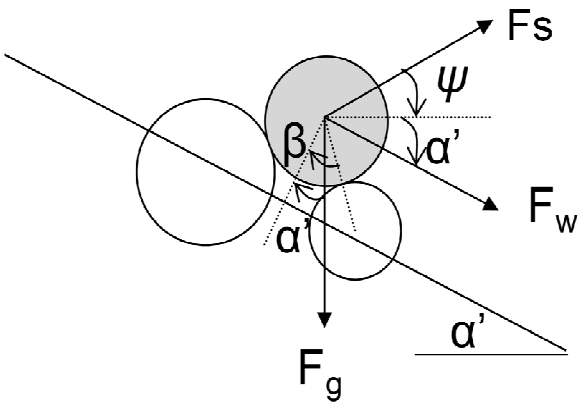

Figure 3.2 Force balance on a particle on a bank inclined at an angle α'. The particle makes an angle β with another particle and is subjected to a seepage force (*Fs*) exiting the bank at an angle ψ, a tractive force due to surface runoff (*Fw*), and gravity (*Fg*) (after Howard and McLane, 1988).

Lobskovsky et al. (2004) studied the threshold phenomena associated with the onset of erosion using noncohesive glass beads. They derived a critical slope equation with the rationale that slopes greater than the critical slope were unstable if there is seepage through it. This critical slope relates to the dimensionless Shield stress (τ_c^*) which was modified to take into account the seepage force:

$$s_c = \frac{\tau_c^* \left(\frac{\rho_s}{\rho} - 1 \right)}{a} \tag{3.5}$$

where s_c is the critical slope, and a is the seepage reduction factor which deals with the fact that grains on the surface experience less seepage force than those several layers deep.

3.2.1 Mass Failure (Coulomb Failure)

Mass failure analysis evaluates the balance of forces acting on a soil element of an infinite slope. It attempts to predict the conditions when the resultant of the driving forces

exceeds the resultant of the stabilizing forces causing small or large masses of soil to fail. For example, an infinite slope approach was used by Budhu and Gobin (1996) to analyze the minimum, stable seepage-slope angle for an infinite, noncohesive slope under a steady-state seepage regime. Their study showed that in order for static liquefaction to occur, the vertical component of the seepage force must be equal to or greater than the weight of the soil. The seepage-slope angle relationship was given as:

$$(\cos\alpha' \quad + \quad \cos\lambda)\frac{\sin\alpha'}{\sin\lambda} = \frac{\gamma'}{\gamma_w} = \frac{G-1}{1+e} = (1-n)(G-1) \tag{3.6}$$

where λ is the direction of the seepage vector measured clockwise from the inward normal to the bank slope, γ' is the saturated weight of the soil, γ_w is the unit weight of water, G is the specific gravity of the soil, and e is the void ratio. Their results showed that for most soils, static liquefaction occurs when the seepage was directed vertically upward.

Seepage erosion by liquefaction was evaluated by Dunne (1990) using balance of forces acting on a volume of soil. For cohesive soils, liquefaction occurs when the cohesive bonds in the soil are weakened considerably by weathering, gravity, or other forces near the seepage face (Dunne, 1990). The balance of forces was given by Dunne (1990) as:

$$i\rho g \geq (\rho_s - \rho)g(1-n) + \frac{c\Delta x\Delta y}{\Delta x\Delta y\Delta z} \tag{3.7}$$

where Δx, Δy, and Δz are the dimensions of the volume of soil undergoing mass failure. Dunne (1990) points out the difficulty in using this equation: if c is large, realistic values of the seepage gradient lead to unrealistically thick failed layers and the seepage gradient

has to become unrealistically large to result in seepage gradients to cause liquefaction at the scale of soil fragments that commonly flow by seepage.

Chu-Agor et al. (2008a) investigated tension or "pop-out" failure due to seepage force exceeding the soil strength by computing the factor of safety of cohesive slopes (Figure 3.3). They derived the factor of safety (*FS*) along the *yy* plane in Figure 3 to be:

$$FS = \frac{\frac{c'}{z\gamma_w} + \left(\frac{\gamma'}{\gamma_w}\cos\alpha' - \sin\alpha'\cot\lambda\right)\tan\phi'}{\left(\frac{\gamma'}{\gamma_w}+1\right)\sin\alpha'} \tag{3.8}$$

Similarly, *FS* along failure plane *xx* was written as

$$FS = \frac{\frac{c'}{b\gamma_w} + \left(\frac{\gamma'}{\gamma_w}+1\right)\sin\alpha'\tan\phi'}{\sin\alpha'\cot\lambda - \frac{\gamma'}{\gamma_w}\cos\alpha'} \tag{3.9}$$

where *c'* is the effective cohesion, *b* and *z* are the dimensions of the soil block, and ϕ' is the effective angle of internal friction. In their experiments conducted on a three-dimensional soil block, tension or "pop-out" failure occurred when the computed *FS* was less than one. They observed seepage particle mobilization and undercutting when the resistive strength of the bank was greater than the seepage gradient and weight forces.

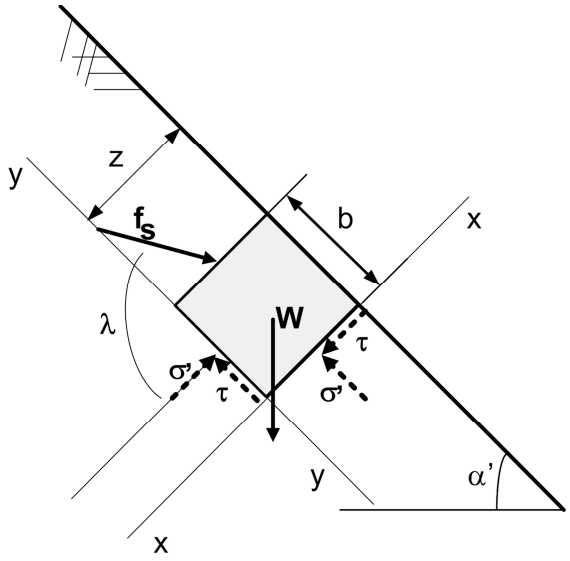

Figure 3.3 Free-body diagram of a soil element subjected to seepage force considering two possible failure planes, *yy* and *xx*. The soil element has dimensions *z* and *b* and is subjected to seepage (f_s) and gravity (W) forces.

3.2.2 Sediment Transport Functions

Sediment transport models for seepage attempt to quantify the amount of sediment eroded, either by individual particle mobilization or mass failure, at a given time. Howard and McLane (1988) derived an average long-term sediment transport function for noncohesive soil. They found that in the sapping zone grains move partly by individual grain motion but mostly by intermittent mass wasting. The amount of seepage-induced mass wasting was assumed to depend on the amount by which the actual slope angle (α') exceeded the critical value (α_c) given by the following equation:

$$q_{sm} = e^{C_r\left[\frac{\alpha'-\alpha'_c}{\alpha'_c}\right]} - 1 \tag{3.10}$$

where q_{sm} is the transport rate due to seepage, C_r is a constant, and α'_c is the critical slope angle given by the quadratic equation:

$$\tan^2 \alpha'_c \left(1+(C_c+1)\frac{\tan\psi}{\tan\beta}\right)+\tan\alpha'_c\left((C_c+1)\left(\tan\psi+\frac{1}{\tan\beta}\right)\right)-C_c=0 \qquad (3.11)$$

where ψ and β are angles defined in Figure 3.2, and C_c is

$$C_c=\frac{C_a(\rho_s-\rho)}{C_b\rho} \qquad (3.12)$$

The biggest challenge in using this sediment transport function is the estimation of the empirical coefficients, C_1, C_2, and C_3, which take into account the packing and particle shape effects.

Fox et al. (2006) derived a sediment transport for seepage erosion of noncohesive streambank sediment based on two-dimensional lysimeter experiments. Their seepage erosion transport function was based on dimensionless sediment discharge and dimensionless seepage flow shear stress. Their study showed a power law relationship between the dimensionless sediment transport rate q_s* and a dimensionless shear stress τ* given as:

$$q_s^* = a\left(\tau^*\right)^b \qquad (3.13)$$

where a = 584 and b = 1.04 for loamy sand soils packed within a small range of bulk densities, ρ_b. Unlike that of Howard and McLane's transport function, this transport function related sediment flux to seepage discharge from the bank. However, they were concerned with the applicability of the proposed sediment erosion function for utilization in natural field conditions because their function was derived using two-dimensional experiments where the width of the bank face was limited. Seepage undercutting in the field (Figure 3.1) has a three-dimensional geometry (Fox et al., 2007).

3.2.3 Objectives

Most studies on seepage erosion have focused their analysis on one failure mechanism, specific soil types, and/or specifically for noncohesive soils limiting their application to the conditions under which they were derived. Furthermore, seepage undercutting in the field has a three-dimensional geometry not addressed in previous studies. In this study, an empirical sediment transport function that can predict sediment mobilization (i.e., seepage erosion and undercutting) over time will be derived and evaluated based on previously reported three-dimensional soil block experiments (Chu-Agor et al., 2008a) covering a wide range of hydraulic, soil type, and packing (i.e., slope and bulk density) combinations. While a mechanistic, process based formulation is favored over empirical approaches, such formulations yield unreasonable results for ground water seepage gradients necessary for particle liquefaction and bank failure (Dunne, 1990).

3.3 MATERIALS AND METHODS

3.3.1 Three-dimensional Soil Block Experiments

Data gathered from the three-dimensional block experiments of Chu-Agor et al. (2008a) were used in this research. The three-dimensional soil block was constructed of Plexiglas with dimensions 50 cm by 50 cm by 50 cm. It had two compartments: a water reservoir at one end where a constant water head was maintained and a soil compartment that simulated a single-layered streambank (Figure 3.4). Water flowed from the water reservoir to the soil compartment through a 10 cm by 10 cm inlet centered at the bottom of the wall dividing the two compartments.

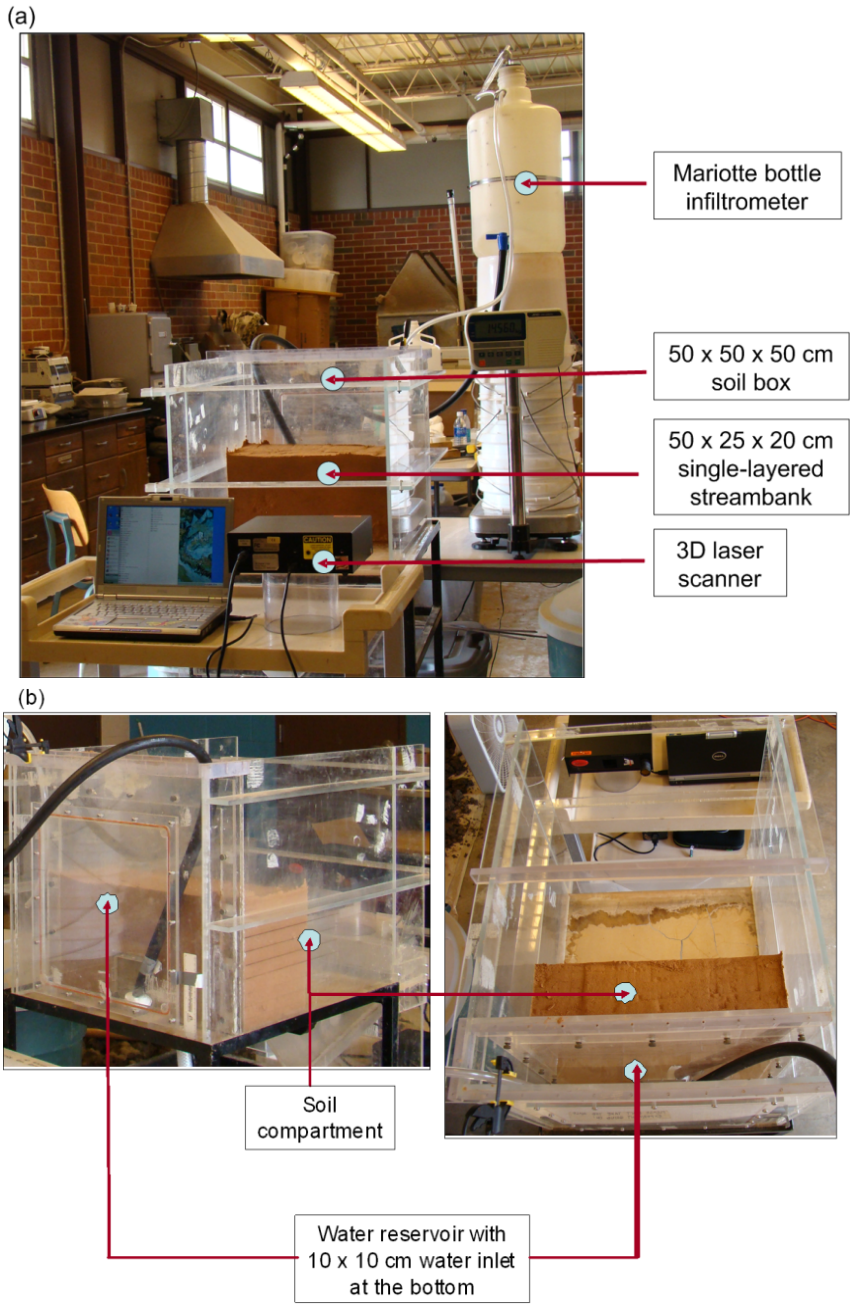

Figure 3.4 Three-dimensional soil block set-up used to simulate seepage erosion of single-layer, repacked soil banks.

Two soil textures were used in the experiments: sand and loamy sand. Each soil type was packed in the box at various ρ_b: 1.30, 1.45, and 1.60 Mg m^{-3} for the sand and 1.30, 1.45, 1.50, 1.60, and 1.70 Mg m^{-3} for the loamy sand. All experiments consisted of

soil blocks with heights of 25 cm, widths of 50 cm, and lengths of 25 cm. The bottom of the soil block was lined with a 2.5 cm densely packed clay layer to serve as a restrictive layer. The rest of the block was packed with soil to the desired ρ_b in 2.5 cm lifts. The soil was then cut to simulate various bank angles, α' (90, 75, and 60 degrees), such that the horizontal centerline for each bank remained 20 cm away from the water inlet. For the experiments, heads (*H*) of 15, 25, or 35 cm were maintained in the inflow reservoir.

During the experiment, a three-dimensional medium-range laser scanner (3D Digital Corporation, Sandy Hook, CT) was used to monitor seepage erosion at the bank face of the soil block (Figure 3.4). Scanned images were taken at regular intervals to capture the change in the bank due to seepage erosion (Figure 3.5). The scanned images were then exported to ASCII files in terms of the xyz coordinates and used to create 2.0 mm square grids. A program was developed to compute the eroded volume by subtracting the scanned surface at a given time from the initial bank. Chu-Agor et al. (2008a) demonstrated that a five-parameter Gaussian function (Weisstein, 1999) fit the typical shape of the seepage undercuts (Figure 3.6), where the function is given as the following:

$$z(x,y) = d_u \exp\left[-\left\{\left(\frac{x-x_o}{\sigma_x}\right)^2 + \left(\frac{y-y_o}{\sigma_y}\right)^2\right\}\right] \tag{3.14}$$

where $z(x,y)$ is the measured seepage undercut from the original bank face, d_u is the maximum distance of seepage erosion undercutting, x_o and y_o is the center of the maximum undercut distance, and σ_x and σ_y are spreads of the seepage undercut in the width and height dimensions, respectively (Figure 3.6). The variables σ_x and σ_y are related to the full width at half-maximum ($FWHM_j$) of the Gaussian function:

$$FWHM_j = 2\sqrt{2\ln(2)}\sigma_j \tag{3.15}$$

where j is either x or y (Weisstein, 1999).

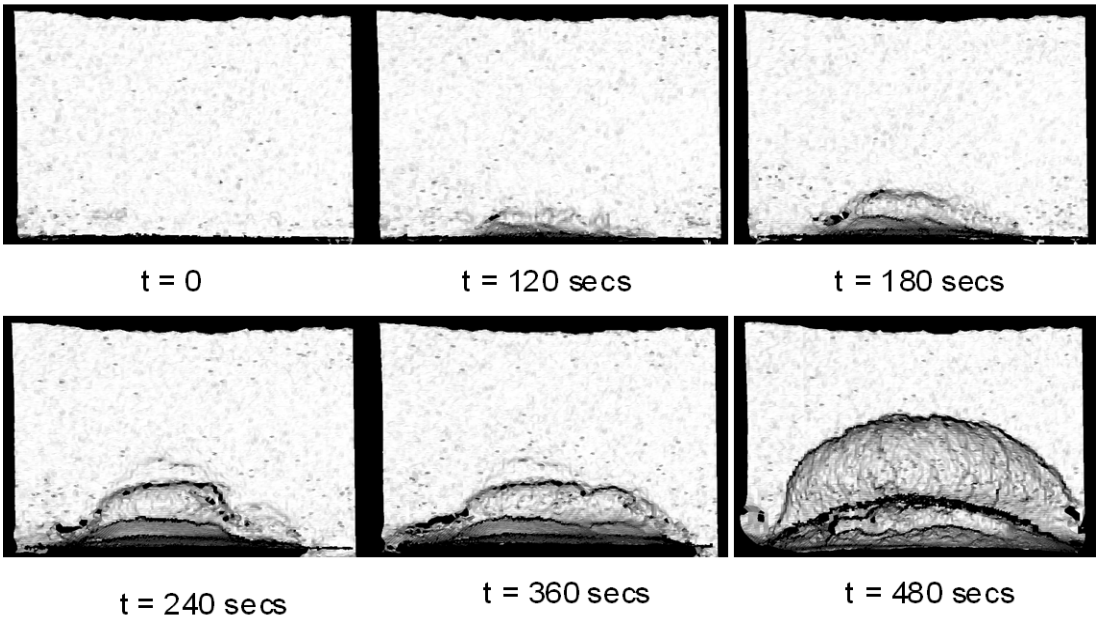

Figure 3.5 Scanned image of the bank face of the three-dimensional soil block at different times during an experiment. Images shown are for a 90-degree sand bank, 15 cm water head with ρ_b = 1.60 Mg m^{-3}.

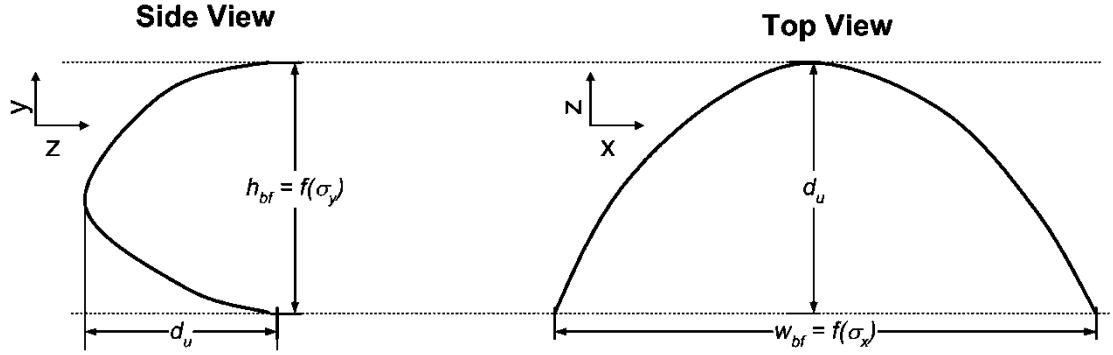

Figure 3.6 Dimensions of the undercut: the maximum undercut distance, d_u, the height at the bank face, h_{bf}, and the width at the bank face, w_{bf}. The h_{bf} and w_{bf} are functions of the vertical and horizontal spreads (σ_y and σ_x), respectively.

The strength properties of the soil used in the experiments were determined using a direct shear test (*ASTM Standards* D3080-98). The test specimens were prepared by compacting the soil to a given ρ_b. Three test specimens for each soil type and ρ_b were tested under different normal loads (4 kg, 6 kg, and 10 kg). For a given normal force, the maximum shear stress was determined from the peak of the shear stress versus horizontal deformation curve. The soil strength parameters (cohesion and angle of internal friction) were derived from Mohr's failure envelope (Table 3.1).

Table 3.1 Geotechnical properties (effective cohesion, *c'*, and internal angle of friction, ϕ') and critical gradient (i_{cr}) necessary to propagate an undercut of the two soils used in the laboratory soil column experiments.

Soil Type	ρ_b (Mg cm^{-3})	*c'* (kPa)	ϕ' (^{o})	Critical Gradient, i_{cr} Minimum	Maximum
Sand	1.45	2.0	32.4	0.20	0.25
	1.60	3.4	40.9	0.30	0.35
Loamy Sand	1.60	4.9	32.7	0.35	0.40
	1.70	7.4	40.1	0.45	0.50

3.3.2 Derivation of a Sediment Transport Function

The sediment transport function was represented by an excess gradient equation, where the flow gradient, *i*, was assumed to be based on the steady-state ground water velocity:

$$E_{rs} = k_{ds}\left(i - i_{cr}\right)^a \tag{3.16}$$

where E_{rs} is the seepage erosion rate (i.e., mass of sediment per bank face area per time, kg/m2/s), k_{ds} is the seepage erodibility coefficient (kg/m^2/s), i_{cr} is the critical gradient, and a is an exponent. This relational form of the sediment transport function was used to avoid the necessity of three-dimensional ground water flow modeling. Furthermore, eventual incorporation into a bank stability model will require such a simplified formulation that does not depend on detailed ground water flow simulations.

The gradient, i was estimated from Darcy's Law with Dupuit-Forcheimmer assumptions:

$$v = \frac{q}{n} = \frac{Ki}{n} = \frac{KH\sin(\alpha')}{nL_{sc}} \tag{3.17}$$

$$i = \frac{H\sin(\alpha')}{L_{sc}} \tag{3.18}$$

where v is the pore water velocity, q is the Darcy velocity, L_{sc} is the length of the soil block, K is the saturated hydraulic conductivity, and H is the hydraulic head. For cases with seepage erosion undercutting, the gradient, i, was estimated from the steady-state flow based on H and corrected for the measured distance of undercutting, $d_u(t)$, such that the path length was L_{sc}-$d_u(t)$:

$$i = \frac{H\sin(\alpha')}{(L_{sc} - d_u(t))} \tag{3.19}$$

Increased $d_u(t)$ increased i by reducing the path length through which ground water must discharge.

3.3.3 Critical Gradient

The critical gradient, i_{cr} is the hydraulic gradient that must be imposed on the sediment before seepage erosion initiates. This critical gradient can be mechanistically

predicted for noncohesive soils; however, Chu-Agor et al. (2008a) demonstrated that cohesion is important for seepage erosion processes in sand and loamy sand soil textures packed at various ρ_b.

As mentioned previously, Dunne (1990) suggests that this critical gradient should be a function of the immersed weight of the grains or aggregates and the cohesion per unit area, as shown in equation (3.7). The difficulty with equation (3.7) is that if c is large, realistic values of the seepage gradient lead to unrealistically thick failed layers. However, the seepage gradient has to become unrealistically large to result in seepage gradients to cause liquefaction at the scale of soil fragments that commonly flow by seepage (Dunne, 1990). Furthermore, for steep bank angles, an additional force created by overburden must be included in the force balance before liquefaction and mobilization can occur.

Because of these difficulties in using mechanistic approaches with cohesive soils, an empirical analysis was performed to derive i_{cr} based on the fundamental properties influencing liquefaction (i.e., c). To derive this relationship, additional soil block experiments were performed. The soil block was packed with sand and loamy sand at various ρ_b. The bank face was maintained at a 90-degree angle. At the start of the experiment, the head in the water reservoir was set at 4 cm (i.e., 1.5 cm above the clay layer). Once steady state flow was reached, the head was increased by 1 cm and the system was allowed to reach equilibrium. If no undercutting was observed, this process was repeated until a sufficient head was reached that was capable of propagating an undercut (Figure 3.7). Each experiment with a given set of soil and hydraulic controls was carried out in duplicate. Since the head was increased in 1 cm increments, a

minimum and a maximum were used to define the critical head, with the minimum value being the head before undercutting occurred and the maximum value when undercutting propagated. The critical gradient was determined by dividing the critical head, H_{cr}, which was measured using the three-dimensional soil block set-up of Chu-Agor et al. (2008a), by the length of the soil block.

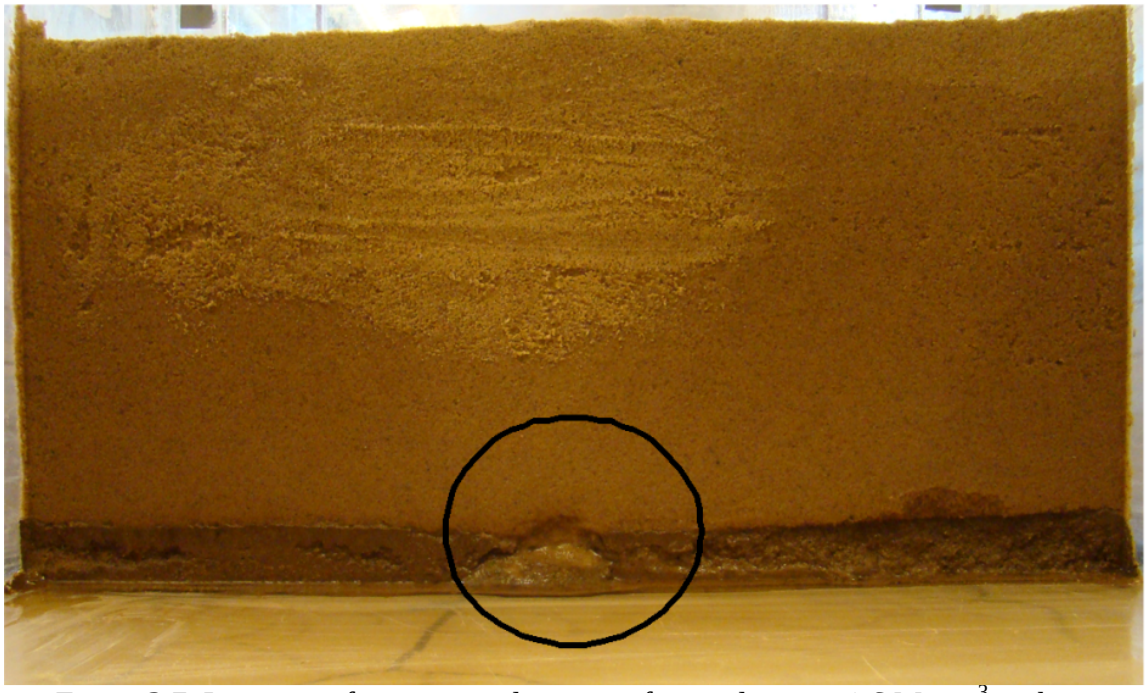

Figure 3.7 Initiation of seepage undercutting for sand at ρ_b = 1.6 Mg m^{-3} with an imposed gradient of 0.30. The imposed gradient was capable of propagating an undercut.

3.3.4 Function Development

Experiments conducted by Chu-Agor et al. (2008a) that experienced seepage undercutting were divided into two groups. Two-thirds of the experiments (34 independent experiments) were used for function development (Table 3.2) and the remaining one-third (18 independent experiments) for function evaluation (Table 3.3). The groups were chosen randomly based on a random number generator. Each experiment consisted of one or more scanned images representing the evolution of the

undercut before mass wasting occurred. Thus, each experiment contained measurements of d_u at different times during the experiment (i.e., 93 observations for function development and 40 observations for evaluation).

Table 3.2 Soil, hydrologic, and bank characteristics of function development data sets (i.e., approximately two-thirds of the soil block experiments).

Soil Type	ρ_b (Mg m^{-3})	α' (^{o})	H (cm)	Number of Experiments (Number of Scans in each Experiment)
Sand	1.60	90	15	2 (3, 4)
	1.60	75	15	1 (3)
	1.60	60	15	1 (3)
	1.60	90	25	2 (3, 5)
	1.60	75	25	2 (5, 3)
	1.60	60	25	1 (2)
	1.60	75	35	2 (4, 1)
	1.60	60	35	2 (3, 3)
	1.45	90	15	1 (2)
	1.45	75	15	1 (2)
	1.45	90	25	2 (2, 3)
	1.45	60	25	1 (4)
	1.45	90	35	1 (2)
	1.45	75	35	2 (2, 2)
	1.45	60	35	1 (3)
Loamy Sand	1.60	90	15	1 (2)
	1.60	90	25	1 (3)
	1.70	90	15	1 (3)
	1.70	90	25	1 (1)
	1.60	75	15	1 (6)
	1.60	75	25	1 (3)
	1.70	75	15	1 (2)
	1.70	75	25	1 (1)
	1.70	75	35	1 (3)
	1.60	60	25	1 (1)
	1.70	60	15	1 (4)
	1.70	60	25	1 (1)

Table 3.3 Soil, hydrologic, and bank characteristics of function evaluation data sets (i.e., approximately one-third of the soil block experiments).

Soil Type	ρ_b (Mg m^{-3})	α' (^{o})	H (cm)	Number of Experiments (Number of Scans in each Experiment)
Sand	1.45	60	15	1 (5)
	1.45	60	25	1 (4)
	1.45	75	15	1 (3)
	1.45	75	25	1 (3)
	1.45	90	15	1 (2)
	1.45	90	35	1 (2)
	1.6	60	25	1 (2)
	1.6	75	15	1 (1)
	1.6	90	35	1 (4)
Loamy Sand	1.6	60	15	1 (4)
	1.6	60	35	1 (1)
	1.6	75	35	1 (4)
	1.6	90	35	1 (1)
	1.7	60	35	1 (2)
	1.7	90	35	1 (2)

From the laboratory experiments, the observed erosion rate, E_{rs}, was computed by dividing the ratio of the eroded volume to the area of the undercut, V_u/A_u, by the observed time and multiplying by ρ_b. The average value of i_{cr} was used with the soil properties for the specific type and packing. A nonlinear regression of E_{rs} versus i-i_{cr} was fit to all 34 experiments with varying soil type, ρ_b, H, and bank angles. A limitation of the proposed sediment transport function is that it assumes laminar flow conditions. Therefore, the equation is only valid for i_{cr} less than a maximum gradient at which turbulent flow occurs. Laminar flow conditions should be prevalent in the field except under cases of macropore or pipe flow (Wilson, 2009). Also, for function development, relationships were derived between V_u/A_u and d_u. Geometric relationships between the undercut

distance and height (d_u and σ_y) for the experiments in the function development data set were also defined.

3.3.5 Function Evaluation

The function was evaluated by comparing the predicted time using the relationships discussed previously to the observed time for a given d_u. First, a value of d_u as measured during the function evaluation experiment was selected. The ratio V_u/A_u was then computed using the relationship between V_u/A_u and d_u obtained during function development. The gradient, i, was computed as a function of the selected d_u using equation (3.19). The critical gradient, i_{cr} was determined based on the measured critical head, H_{cr}, using equation (3.18). Next, the erosion rate, E_{rs}, was calculated using the empirical equation derived from the function development dataset (i.e., equation 3.16). The time required for a given d_u to develop was then calculated as:

$$t_p = \frac{V_u / A_u}{E_{rs} / \rho_b} \tag{3.20}$$

Finally, a linear regression analysis was performed between the observed time to reach the specific, d_u, to the predicted time, t_p, calculated using the seepage erosion sediment transport function and the geometrical undercut relationships.

3.3.6 Estimating the Undercut Dimensions

From knowledge of d_u and σ_y, the five-parameter Gaussian function can be simplified to approximate the height (h) (and if necessary the width, w) of the undercut at different distances along d_u. For example, at the bank face, one can solve for h_{bf} (i.e., height of the undercut at the bank face, respectively) when z is reasonably close to zero (i.e., $z = \varepsilon$). To solve for the h_{bf}, simply substitute $x = 0$ with $x_o = 0$ and $y_o = 0$ into equation (3.14) and solve for $y = h_{bf}/2$. The following equation is derived:

$$h_{bf} = 2\sigma_y \sqrt{-\ln\left(\frac{\varepsilon}{d_u}\right)} \tag{3.21}$$

Similarly, solving for the h at any z, where $z < d_u$, results in the following equation that allows prediction of the undercut shape height:

$$h(z) = 2\sigma_y \sqrt{-\ln\left(\frac{z}{d_u}\right)} \tag{3.22}$$

In order to compute h_{bf} using equation (3.21), it was first assumed that ε was equal to the average particle diameter or the median particle size, d_{50}, of the particle size distribution since an undercut cannot be formed until at least one particle is dislodged from the bank. The values of σ_y were computed using the Gaussian function for a given d_u. Next, a calibrated ε was derived using the function evaluation data set based on minimizing the root mean squared error (RMSE) between the dimensions of the undercut (h_{bf}) measured from the scanned images to the dimensions computed using equation (3.21).

3.4 RESULTS AND DISCUSSION

3.4.1 Function Development and Evaluation

Prior to deriving the sediment transport function, the critical gradient, i_{cr}, was determined by measuring the critical head, H_{cr}, for the coarse and loamy sand using the three-dimensional soil block set-up of Chu-Agor et al. (2008a) (Table 3.1). Recall that the value of H_{cr} used in computing i_{cr} was the average of the minimum and the maximum values (Table 3.1). Using H_{cr}, the relationship between i_{cr} and effective cohesion, c', was established (Figure 3.8). Soil cohesion adds an extra force that has to be exceeded, in addition to gravity and water forces, before liquefaction could occur. According to Dunne

(1990), for soil with some amount of cohesion, an extra force is acting on the soil mass resisting the separation of the mass. He added that i_{cr} depended on the thickness of the volume that eventually separated. Cohesion therefore is a parameter which can also be used to estimate i_{cr}. Regardless of soil type and packing condition, i_{cr} and c' followed a logarithmic relationship (Figure 3.8).

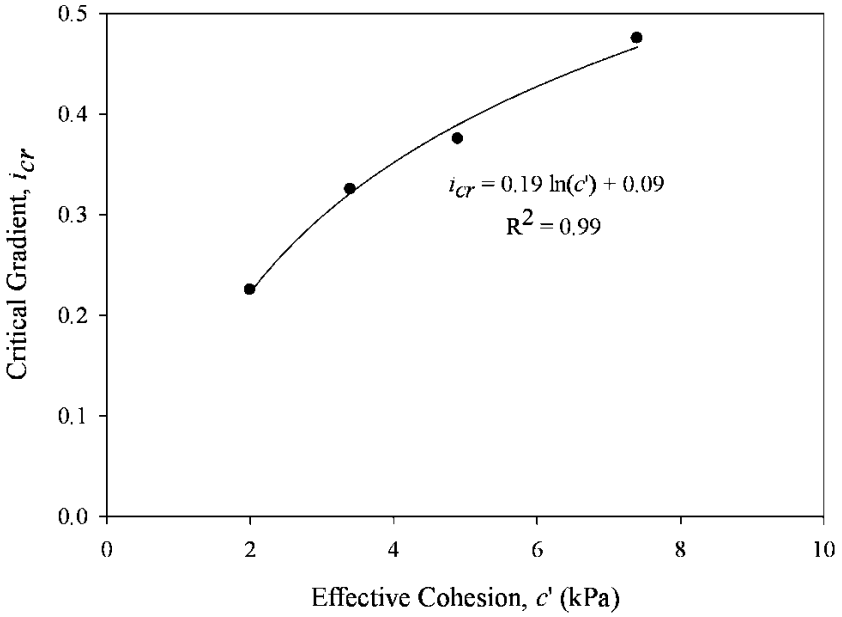

Figure 3.8 Relationship between the critical gradient, i_{cr}, and effective cohesion, c'. The critical gradient was computed by dividing the critical head, H_{cr}, which was measured in the laboratory, by the length of the soil block. This relationship applies to sand and loamy sand at different bulk densities.

Results of the non-linear regression between experimental data on E_{rs} versus i-i_{cr} for all the 34 experiments with varying soil type, ρ_b, H, and bank angles resulted in k_{ds} = 0.04 kg/m^2/s and a = 1.2, respectively, with a coefficient of regression, R^2, of 0.54 (Figure 3.9). This function covered a wide range of variability (i.e., different hydraulic

controls, different packing conditions, and two soil types) as well as the three-dimensional nature of the seepage erosion.

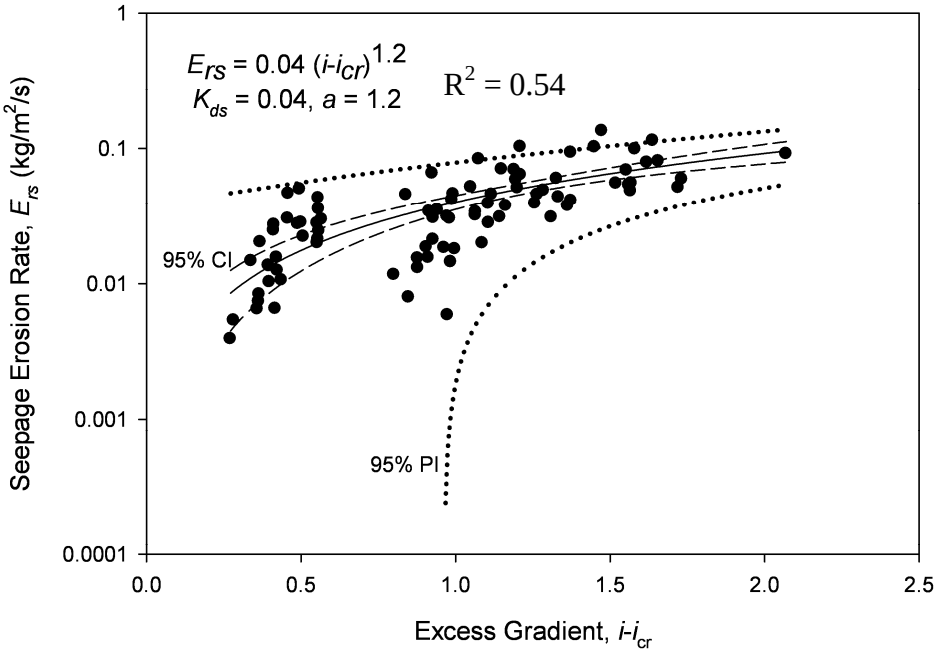

Figure 3.9 Relationship between seepage erosion rate (E_{rs}) and excess gradient (i-i_{cr}) using data from function development studies consisting of data from both soil types (coarse sand and loamy sand) and across a range of several different bulk densities (1.3 to 1.7 Mg m^{-3}), heads (15 to 35 cm), and bank angles (60 to 90 degrees). The inner band is the 95% confidence interval while the outer band is the 95% prediction interval.

The sediment transport function was derived from sand and loamy sand experiments where banks experienced undercutting. Based on the results from Chu-Agor et al. (2008a), undercutting occurred when the bank's shear strength was great enough to resist initial tension until liquefaction initiated particle mobilization. They further showed that this mechanism is largely controlled by the soil's ρ_b, which in turn controlled the hydraulic and geotechnical properties of the soil. In their experiments, seepage undercutting occurred when the ρ_b for sand and loamy sand was greater than 1.3 Mg m^{-3}

and 1.5 Mg m^{-3}, respectively. For other soil types, the limiting ρ_b for seepage undercutting to occur was hypothesized to increase as the clay content increased and hence, could be greater than 1.5 Mg m^{-3}. This means that these soil types may not experience seepage undercutting in the field, but rather may collapse due to the force of the ground water seepage gradient alone (i.e., without undercutting), as described by Chu-Agor et al. (2008a). These other soil types have to have a higher ρ_b than typically observed in the field in order for the soil mass to hold the initial tension until undercutting initiates. Since sand and loamy sand have a lower ρ_b threshold, they are more vulnerable to seepage undercutting in the field than other soil types that experience mass failure without first developing an undercut.

Since the function considers the three-dimensional nature of seepage erosion, the geometry of the undercut has to be defined. Mathematically, a linear relationship is expected between d_u and V_u/A_u when using the Gaussian function. For the function development data sets, a linear relationship with slope of 0.3 between V_u/A_u and d_u was observed (Figure 3.10). This relationship provided the link between d_u with the average distance of undercut, V_u/A_u, and E_{rs}. Future research should be devoted to investigating other multiple dimensional shapes for the seepage undercuts, such as elliptic paraboloids, to see if stronger relationships can be derived.

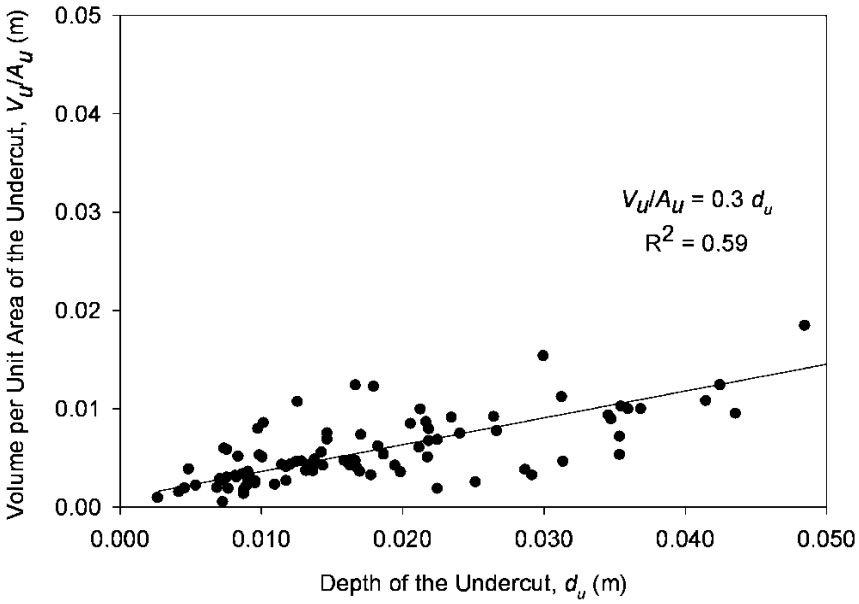

Figure 3.10 Relationship between seepage erosion maximum distance of undercut, d_u, and volume per unit area (V_u/A_u) using data from function development studies consisting of data from both soil types (coarse sand and loamy sand) and across a range of several different bulk densities (1.3 to 1.7 Mg m^{-3}), heads (15 to 35 cm), and bank angles (60 to 90 degrees).

The function was evaluated using the remaining 18 experiments by comparing the observed time with the predicted time for which a chosen d_u developed. The linear regression analysis between the predicted time and the observed time resulted in an R^2 of 0.79 (Figure 3.11). The function was found to slightly under predict the time to develop a given d_u at large time. Larger observed times corresponded to experiments performed on stable banks (i.e., lower α' and H, and higher ρ_b).

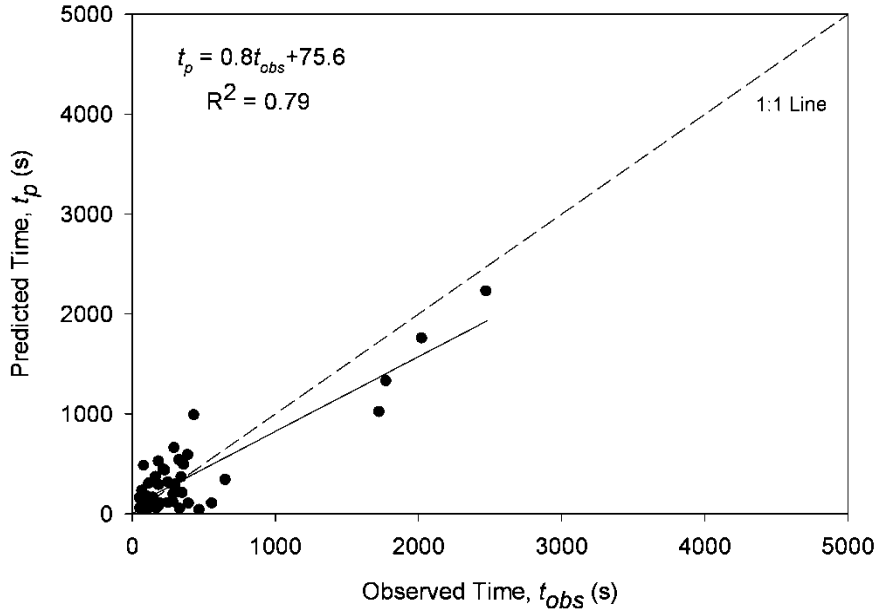

Figure 3.11 Linear regression between predicted time (t_p) and observed time (t_{obs}) calculated using the seepage erosion sediment transport function and geometrical undercut relationships to obtain the observed maximum distance of undercut (d_u) for the function evaluation studies.

3.4.2 Dimensions of the Undercut

From a prediction of d_u, Chu-Agor et al. (2008a) and this research documented the appropriateness of a Gaussian distribution, from which predictions of σ_y of the undercut could be made (Figure 3.12). Once σ_y is known, h_{bf} can be computed using equation (3.21). When assuming ε equal to d_{50} or using a calibrated ε equal to $2d_{50}$, linear regression analysis between the measured and computed h_{bf} yielded an R^2 of 0.84 for h_{bf} (Figure 3.13). The calibrated ε resulted in slightly lower RMSE for h_{bf} for the loamy sand and approximately equivalent RMSE for the sand. The latter should be used since little difference was observed in the RMSE between the calibrated ε and ε equal to d_{50}.

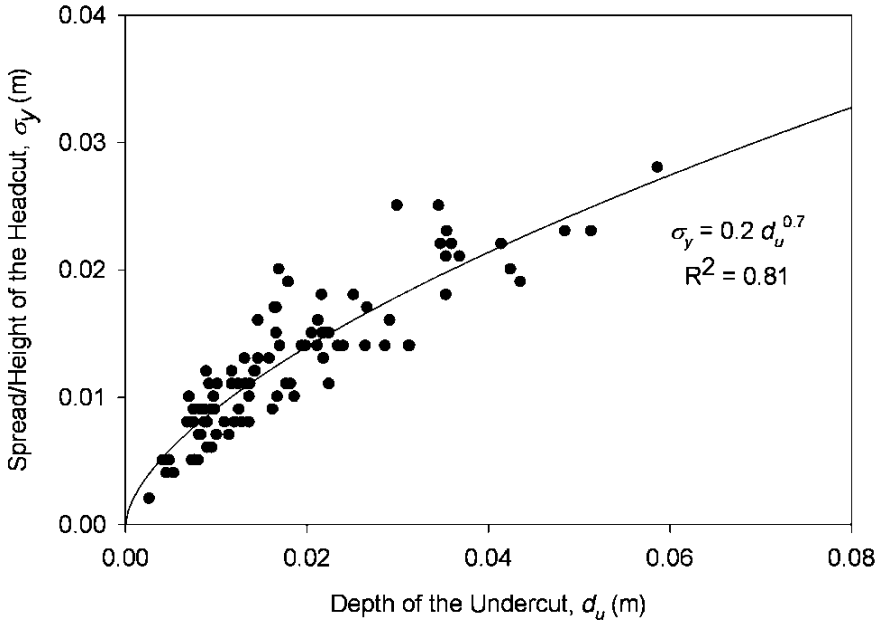

Figure 3.12 Observed relationship between the maximum distance (d_u) of the undercut and the height as quantified by the spread (σ_y) for the sand and loamy sand soils within the function development data sets.

It was noted from the regression analysis that the equation for h_{bf} derived from the Gaussian function overestimated the measured values when h_{bf} was greater than 5 to 10 cm. This can result in unrealistic values for larger undercuts. Therefore, the use of the Gaussian function in estimating h_{bf} should be limited to the dimensions of undercuts used in the linear regression analysis, i.e., h_{bf} should be less than 10 cm. These dimensions correspond to d_u of approximately 10 cm. Results from Chu-Agor et al. (2008b) showed that a d_u of approximately 3 to 5 cm is sufficient for an initially stable bank to reach a probability of failure equal to 100%. Therefore, the range of dimensions which the function can predict is sufficient to cause bank instability and failure.

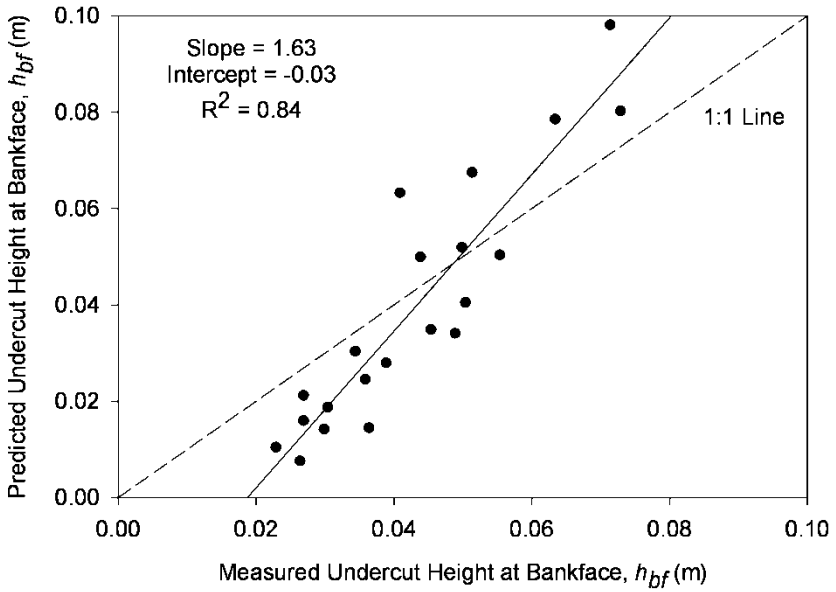

Figure 3.13 Linear regression analysis between the measured and computed undercut height (h_{bf}) for the function evaluation data set.

3.4.3 Use of the Sediment Transport Function

With the above sediment transport functions and relationships between d_u and geometry of the undercut, knowledge of the ground water velocity exfiltrating from the streambank can be used to predict the bank geometry resulting from seepage erosion undercutting. The empirical approach used in this research lends itself to being incorporated into a bank stability model with limited information needing to be input by the user.

First, users will need to input the cohesion of the streambank seepage layer to derive a critical gradient. Second, users need to have an estimate of hydraulic gradients over time. The average gradient based on measured or modeled ground water table elevations in the adjacent streambank can be used to compute the erosion rate at every time step using the derived sediment transport function (i.e., equation 3.16) and the

distance of undercut from the previous time step (i.e., an explicit formulation). A negative erosion rate (i.e., $i < i_{cr}$) signifies no transport for that particular time step. For the entire simulated time, the cumulative E_{rs} can be obtained if the user specifies the layer's ρ_b. From the computed E_{rs}, the V_u/A_u can be estimated. For a two-dimensional bank stability model, only the height of the undercut at the bank face, h_{bf}, is needed, which can be determined using equation (3.21).

3.5 SUMMARY AND CONCLUSIONS

An empirical sediment transport function that accounts for soil cohesion and the three-dimensional nature of undercut formation was developed and evaluated based on soil block experiments of seepage erosion undercutting. Most seepage analyses are focused only on the critical gradient to create liquefaction and/or the critical gradient to cause noncohesive bank failure. This research presents the first development and evaluation of a methodology for simulating seepage erosion undercutting. The transport function was represented by an excess gradient function wherein the rate of erosion was related to the difference between the flow gradient and a critical gradient. The former was estimated from Darcy's Law with an adjustment to take into account the distance of seepage undercutting. Mechanistically, the critical gradient should be a function of the soil cohesion, and in this research, the critical gradient was related to the effective cohesion through a logarithmic relationship. The relationship between the eroded volume per bank face area and d_u was also derived based on an assumed Gaussian function for the undercut shape. Future research should investigate additional three-dimensional functions that may better represent the undercut shape. The sediment transport function together with the derived relationships between the dimensions of the undercut and its

geometry can be used to incorporate the effects of seepage erosion undercutting into bank stability analysis with integrated groundwater flow and stability models. Users only need to input the seepage layer's cohesion, bulk density, and the hydraulic gradient over time in the near bank ground water system.

CHAPTER 4

Incorporating Seepage Processes to Streambank Stability Model[4]

4.1 ABSTRACT

Seepage processes are usually neglected in bank stability analyses although they can become a prominent failure mechanism under certain field conditions. This study incorporated the effects of seepage (i.e., seepage gradient forces and seepage erosion undercutting) into the Bank Stability and Toe Erosion Model (BSTEM) and evaluated the importance of the seepage mechanisms on bank stability. The effects of the seepage force were incorporated into BSTEM by modifying the force balance. Seepage erosion undercutting was simulated using a recently proposed sediment transport function. The modified BSTEM was then used to evaluate the stability of a streambank along Little Topashaw Creek under different scenarios: (1) without seepage forces and undercutting, (2) with seepage forces only, (3) with seepage undercutting only, and (4) with both seepage forces and undercutting. For a condition where the bank was fully saturated, the factor of safety (*FS*) decreased by as much as 66% (i.e., *FS* decreased from 2.68 to 0.91)

[4] Conference paper at the 2009 ASABE Annual International Meeting, Reno, Nevada
Chu-Agor, M.L., G.A. Fox, and G.V. Wilson. 2009. Incorporating Seepage Processes into a Streambank Stability Model. *ASABE Paper No. 095936*, St. Joseph, Mich.: ASABE.

from that of a dry condition due to the decrease in the frictional strength of the soil as the pore-water pressure increased. Incorporating the effects of the seepage force resulted in an average decrease in *FS* of approximately 30 to 50% for all water table depths. Seepage erosion undercutting reduced the *FS* by approximately 6% for a 5 cm undercut (i.e., 2% of bank height) and 11% for a 10 cm undercut (i.e., 3.3% of bank height) due to the loss of supporting material in the conductive layer. Seepage erosion undercutting required 15 to 20 cm of seepage undercut to become the dominant failure mechanism over seepage forces and pore-water pressure effects. The cumulative effects of seepage reduced this streambank's *FS* by up to 63% when the water table reached the entire bank height. The development of a bank stability model capable of simulating seepage processes was necessary in order to better understand site-specific failure mechanisms.

4.2 INTRODUCTION

Seepage in soil affects stability primarily in three ways: (1) by reducing soil strength, (2) by exerting seepage forces, and (3) by seepage erosion undercutting. Seepage produces pore-water pressure which reduces the frictional strength of the soil and thus its shear strength. It can alter the structure of the soil which in turn can reduce or eliminate cohesive strength. It also produces a seepage force. As water flows through the soil, it loses energy. Since energy is neither created nor destroyed, this lost energy is transferred to the soil skeleton in the form of the seepage force (Reddi, 2003). According to Reddi (2003), the magnitude of the seepage force is often significant enough to disturb the force balance and destabilize soils. In the case of streambanks, the seepage force is exerted on the soil skeleton as water flows out of the bank or as it infiltrates deeper into the soil.

Another effect of seepage on stability is seepage erosion undercutting (Fox et al., 2007; Wilson et al., 2007). For example, a perched water table can develop due to high infiltration rates in a conductive soil underlain by an impermeable layer. Water upon reaching the restricting layer will be forced to flow horizontally. At the point where water exits the bank, erosion can occur producing cave-like features called seepage undercuts (Figure 4.1). As these undercuts become larger, supporting material is lost which can lead to cantilever failures. This process has been noted to occur in numerous geographical locations (Fox et al.; 2007, Wilson et al. 2007) and its importance on stability has been highlighted in recent research (Cancienne et al., 2008; Chu-Agor et al., 2008b).

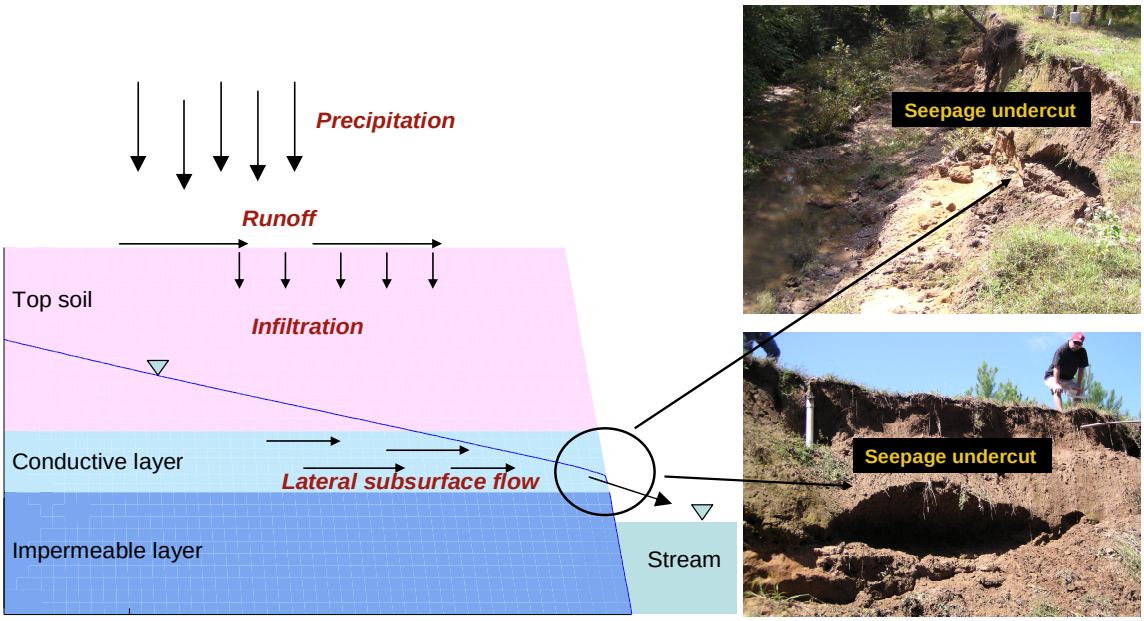

Figure 4.1 Streambank seepage and erosion due to infiltrating water (after Fox et al., 2006) and example of seepage erosion undercutting along Goodwin Creek in northern Mississippi.

Most bank stability models account for the effects of seepage by considering changes in soil pore-water pressure on the shear strength of the bank. Integrated codes

like SEEP/W and SLOPE/W (Geo-Slope International, Ltd.) are used to link groundwater flow and slope stability models where pore-water pressure simulated from the groundwater model is used as input to the bank stability model. However, the change in the geometry of the bank face due to seepage erosion undercutting as well as the effects of seepage force are not dynamically simulated in any existing bank stability models. Although several authors have attempted to predict bank instability and failure due to seepage (Howard and McLane, 1988; Dunne, 1990; Budhu and Gobin, 1996; Lobskovsky et al., 2004; Fox et al., 2006; and Chu-Agor et al., 2008a,b), no stability models exist that incorporate all of these seepage mechanisms.

4.2.1 Bank Stability and Toe Erosion Model (BSTEM)

The Bank Stability and Toe Erosion Model (BSTEM) was developed by United States Deparment of Agriculture's Agricultural Research Service (USDA-ARS) as a tool to evaluate streambank stability for river management, stabilization and restoration. It is an Excel-based program that evaluates bank stability and estimates fluvial erosion due to surface flow. It considers up to five distinct material layers, the effects of saturated and unsaturated pore-water pressure, the confining pressure from the river, as well the reinforcement and surcharge effects of vegetation on top of the bank. The model evaluates stability by computing the factor of safety (*FS*) using limit equilibrium theorem of a planar shear failure plane. It is capable of evaluating streambank stability due to the combined effects of changes in pore-water pressure, presence of vegetation, and fluvial erosion. Cancienne et al. (2008) and Wilson et al. (2007) used BSTEM to evaluate the effects of seepage erosion on bank stability by manually adjusting the geometry of the soil profile.

The user can specify the location of the ground water table or the vertical pore-water pressure distribution. If the user defines the water table depth, BSTEM assumes hydrostatic conditions below the water table, and linearly interpolates the matric suction above the water table. The latest version of BSTEM (version 4.1) does not address the reduction in the soil strength due to seepage induced forces nor does it consider the change in the geometry of the domain due to seepage erosion undercutting.

4.2.2 Objectives

The objective of this study was to incorporate seepage effects (i.e., seepage erosion and seepage forces) into BSTEM and to evaluate the importance of these mechanisms on stability. The near bank ground water gradient was simulated using SEEP/W. The seepage force was computed and incorporated into the computed *FS*. Also, the geometry of the simulated seepage layer was updated based on a seepage hydrograph predicted by the ground water flow model and a recently proposed seepage erosion sediment transport function (Chu-Agor et al., 2009).

4.3 MATERIALS AND METHODS

4.3.1 Seepage Force

Incorporating the seepage force, *SF*, into BSTEM involved a force balance analysis where the components of the force were included in the computation of *FS*. In the latest version of BSTEM, the forces considered acting on a soil mass (Figure 4.2) included the gravity force, *W*, the pore-water pressure, *U*, the confining pressure from the stream, *P*, and the soil shear strength, τ .

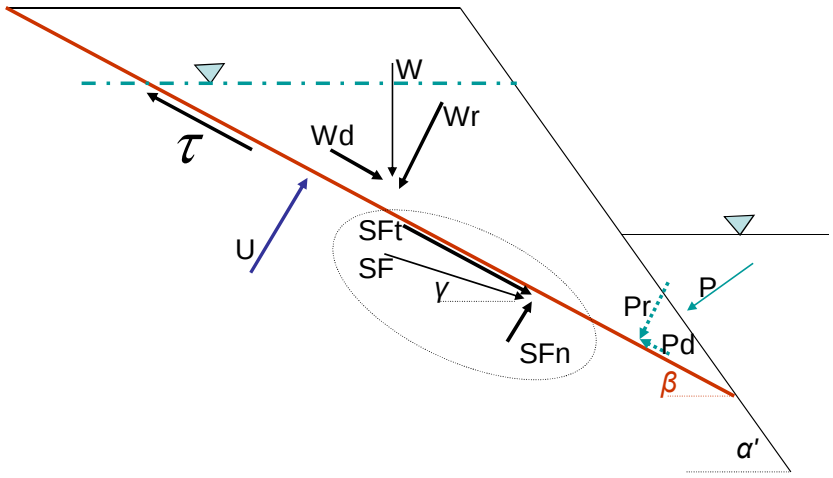

Figure 4.2 Free body diagram of the failure plane in the modified BSTEM. The forces (and their components) acting on the failure mass are: (1) the weight of the soil mass, *W*, (2) the confining pressure, *P*, (3) the pore-water pressure, *U*, (4) the soil shear strength, τ, and (5) the seepage force, *SF* at an angle γ with the horizontal. Angles β and α' are the shear plane and bank angles, respectively.

If one takes the entire failure mass as a free body, the *FS* (ratio of resisting forces to driving forces) without *SF*, can be written as:

$$FS = \frac{\tau}{W_d - P_d} \tag{4.1}$$

For an unsaturated soil, τ is given by Fredlund and Rahardjo (1993) as:

$$\tau = c' + (\sigma - U_a)\tan\phi' + (U_a - U)\tan\phi^b \tag{4.2}$$

where *c'* is the effective cohesion, ϕ' is the effective angle of friction, ϕ^b is the rate of increase in shear strength relative to the matric suction, (U_a-U), σ is the total normal stress, and U_a is the pore-air pressure. As water approaches saturation, U approaches U_a, the matric suction goes to zero and equation (4.2) becomes the equation for saturated soil:

$$\tau = c' + (\sigma - U)\tan\phi' \tag{4.3}$$

In the case of a saturated soil mass (Figure 4.2) without seepage, σ is defined as:

$$\sigma = W_r + P_r \tag{4.4}$$

The *FS* for a saturated soil mass can be then written as:

$$FS = \frac{c' + [(W_r + P_r) - U]\tan\phi'}{W_d - P_d} \tag{4.5}$$

The magnitude of *SF* acting on a given mass can be written as:

$$SF = \gamma_w i \tag{4.6}$$

where i is the hydraulic gradient, and γ_w is the unit weight of water. The location and direction (i.e., γ) of *SF* can be approximated based on the center of gravity of the flow region and the mean direction of flow in that region (Reddi, 2003).

For a given layer or slice, i can be imported from an external groundwater flow model. For this study, i was simulated using SEEP/W. Since i varied in every slice/layer within the failure mass, the value at the centroid of the slice/layer was considered. In other words, the magnitude was approximated at the mid-point of each layer along the failure plane. The direction of *SF* was taken from the direction of the flow vector. The components of *SF* were then incorporated in the force balance analysis in BSTEM.

When *SF* was included in the mass balance, it affected the resisting as well as the driving forces. In the case of a saturated soil mass, *FS* was written as:

$$FS = \frac{c' + [(W_r + P_r \pm SF_n) - U]\tan\phi'}{W_d + SF_t - P_d} \tag{4.7}$$

where SF_n and SF_t are the normal and tangential components of *SF*, respectively, with respect to the failure plane angle, β (Figure 4.2). The effect of the *SF* on σ and thus on the resisting forces was not always the same. It depended on the value of γ with respect to

β. If γ was greater than β, SF_n has a stabilizing effect on *FS* and otherwise a destabilizing effect if γ was less than β.

4.3.2 Seepage Erosion

Seepage undercutting was incorporated into BSTEM using the sediment transport function developed by Chu-Agor et al. (2009). The sediment transport function was given as:

$$E_{rs} = 0.04(i - i_{cr})^{1.2} \tag{4.8}$$

where E_{rs} is the seepage erosion rate (i.e., mass of sediment, *M*, per bank face area of the undercut, A_u, per time, *t*, kg/m^2/s), *i* is the hydraulic gradient based on the groundwater steady-state velocity, and i_{cr} is the critical gradient. The hydraulic gradient at the bank face of the seeping layer was determined from SEEP/W and imported into BSTEM. The critical gradient was found to be a function of the soil cohesion by Chu-Agor et al. (2009):

$$i_{cr} = 0.19\ln(c') + 0.09 \tag{4.9}$$

where *c'* is the effective cohesion in kPa.

In this study, SEEP/W was used to simulate the average velocity of the seepage layer at the bank face, from which *i* was determined using Darcy's law as follows:

$$i = \frac{vn}{K_s} \tag{4.10}$$

where *v* is the velocity, *n* is the porosity, and K_s is the saturated hydraulic conductivity. The erosion rate was then computed at each time step using the derived sediment transport function, i.e., equation (4.8). A negative erosion rate (i.e., *i* less than i_{cr})

signified no transport before that particular time step. For the entire simulated time, a plot showing the distribution of E_{rs} in time can be obtained (Figure 4.3).

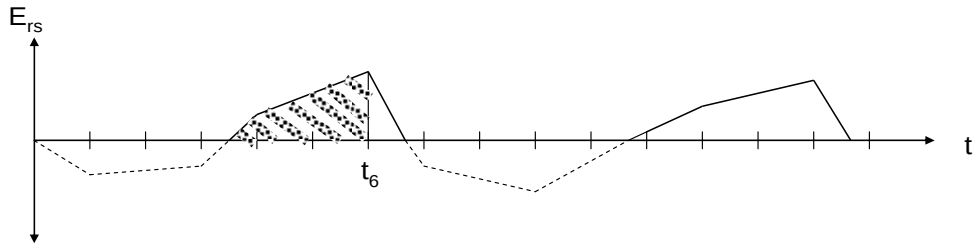

Figure 4.3 Example of the seepage erosion rate, E_{rs}, distributed in time, t. For example, if a user was interested in determining stability between $t = 0$ and $t = t_6$, the cumulative positive E_{rs} between $t = 0$ and $t = t_6$ (shaded area) would be used to determine the total eroded mass, M.

From the computed E_{rs}, the total eroded mass per unit area of seepage undercut, M/A_u, was determined. Note that M/A_u was the product of E_{rs} and t, or the total area of the positive (shaded) region in Figure 4.3 prior to the time step in consideration. From the computed M/A_u, the ratio V_u/A_u, where V_u is the eroded volume, was computed and related to the maximum depth of undercut, d_u, by the following empirical relationship (Chu-Agor et al., 2009):

$$V_u/A_u = 0.3d_u \tag{4.11}$$

Using this relationship, d_u was predicted from E_{rs} at a given time.

Since BSTEM is a two-dimensional stability model, the height of the undercut at the bank face, h_{bf}, was also needed. This was determined using the geometric relationship between the dimensions of the undercut from experiments conducted by Chu-Agor et al. (2009) as follows:

$$h_{bf} = 2\sigma_y \sqrt{-\ln\left(\frac{\varepsilon}{d_u}\right)} \tag{4.12}$$

where ε is average particle size (d_{50}), and σ_y is the spread of the undercut at a given point. For the maximum undercut, σ_y was predicted using the following relationship:

$$\sigma_y = 0.21 d_u^{0.7} \tag{4.13}$$

Once d_u and h_{bf} were computed for the first time step, they were used to update the geometry of the streambank face. The updated profile was then used as the initial profile for the next time step (i.e., an explicit formulation). The parameters of the sediment transport function, i.e., equation (4.8), were determined using this updated profile. Once the time series of seepage erosion undercutting was predicted, the coordinates of the seepage layer were updated in BSTEM and the *FS* at a given time was computed.

4.3.3 Model Application

The modified BSTEM was used to evaluate the stability of a streambank along Little Topashaw Creek (LTC) in Northern Mississippi (Wilson et al., 2007). The LTC has contrasting soil types and layering and hydraulic/hydrologic conditions which are ideal for seepage to occur. Wilson et al. (2007) documented the first *in situ* seepage measurements at LTC. They identified eight seeps which were predominantly characterized as seepage through a conductive layer overlying a water restricting layer. The K_s decreased by two orders of magnitude between these layers and was sufficient to result in seepage flow (Wilson et al., 2007). A typical profile of LTC consists of a thick silt loam (SiL) top layer (1.5 m) underlain by a higher conductive loamy sand (LS) layer

(0.5 m) and a restrictive clay loam (CL) layer (1.0) at the bottom of the profile (Figure 4.4).

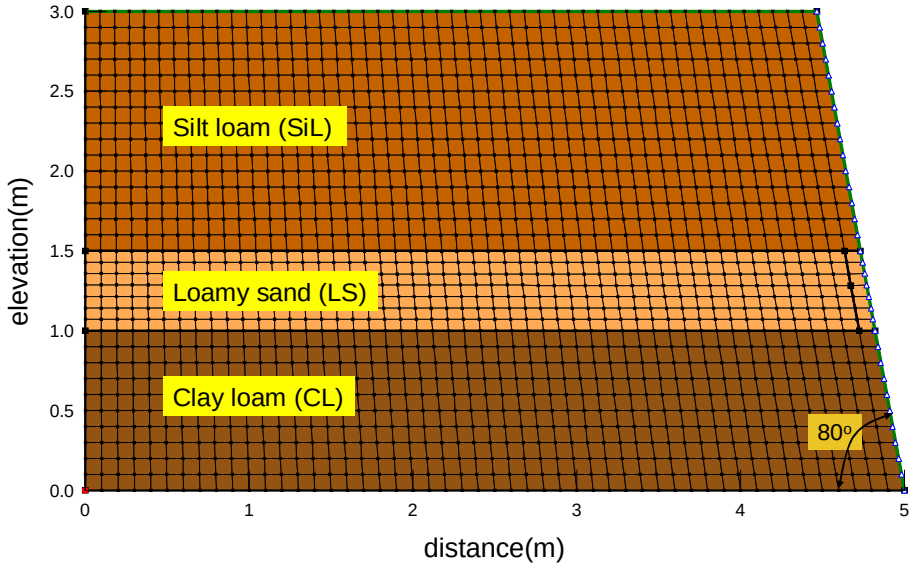

Figure 4.4 Bank profile of LTC used in SEEP/W. The domain was divided into 0.10 m^2 finite elements. A constant head was maintained at the left boundary and free drainage at the bank face (right boundary). No confining pressure from the stream was considered.

The average velocity of the seepage layer was first simulated using SEEP/W using the hydraulic properties measured by Wilson et al. (2007) (Table 4.1). A constant head boundary was imposed at the left side of the domain with a head that varied from 0% of the bank height (*BH*) to 100% of *BH*. The appropriate interval of the time steps was selected by trial and error. Selecting the proper time step was important in simulating seepage erosion undercutting. Erosion did not take place until *i* was exceeded, but once erosion initiated, the process accelerated in time. If the interval between time steps was large, fewer time steps were needed for erosion to initiate; however, the range over which the sediment transport function was applicable may not be captured within the time step. Choosing a small interval on the other hand resulted in longer simulations. Stability was

evaluated using BSTEM by computing the *FS* under different scenarios: (1) without seepage forces and undercutting, (2) with seepage forces only, (3) with seepage undercutting only, and (4) with both seepage force and undercutting. All scenarios included pore-water pressure effects due to the location of the water table.

Table 4.1 Soil hydraulic properties of LTC (after Wilson et al., 2007)

				van Genuchten Parameters	
Soil Type	ρ_b (Mg m^{-3})	K_s (cm/d)	θ_s (cm^{3}cm^{-3})	α (1/cm)	n
SiL	1.39	63.9	0.39	0.006	1.6
LS	1.50	1453.1	0.40	0.012	2.0
CL	1.61	5.4	0.44	0.009	1.7

4.4 RESULTS AND DISCUSSION

BSTEM was first used to compute the *FS* without considering the presence of seepage erosion undercutting or seepage forces. The groundwater table depth was input into BSTEM and duplicated the boundary conditions used in SEEP/W. The depths of the water table assigned to the model were 0, 25, 50, 75, and 100% of *BH*. As the water table increased from 0% of *BH* to 25% of *BH*, *FS* decreased by 19% due to the reduced frictional resistance (i.e., increased pore-water pressure) and increased saturated weight of the soil (i.e., a driving force). The *FS* continued to decrease by 29% as the water table increased from 75% of *BH* to 100% of *BH* (Figure 4.5). For a condition where the bank is totally saturated, *FS* can decrease by as much as 66% from that of a dry condition (i.e., 0% of *BH*).

4.4.1 Stability with Seepage Forces

Incorporating *SF* resulted in an average decrease in the *FS* of approximately 25 to 35% for all water table depths except for 100% of *BH*, which decreased the FS by 55% for a case without seepage erosion (Figure 4.5). The decrease in the *FS* was due to the decrease in the frictional strength of the soil due to SF_n and/or the increase in the driving force due to SF_t. It should be recalled that depending on the seepage angle, γ, relative to β, SF_n could increase the frictional strength of the soil. However, this increase was not as important as the decrease in the driving forces due to SF_t since only a fraction of SF_n (i.e., $SF_n \tan\phi$) contributed to the resisting forces. The large decrease in *FS* for *WT* = 100% of *BH* was due to both SF_n decreasing the frictional strength of the soil and SF_t increasing the driving forces.

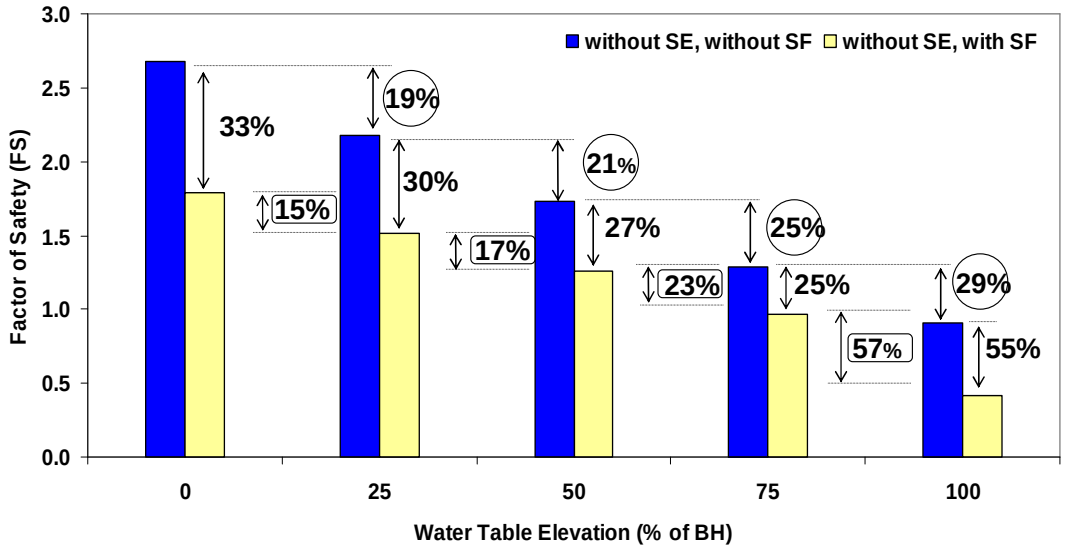

Figure 4.5 Factor of safety, *FS*, with and without the seepage force, *SF*, and the corresponding decrease in *FS*. Percentages inside the circle are the decrease in *FS* due the rise in the water table elevation without *SF*. Percentages inside the rectangle are the decrease in *FS* due to the rise in the water table elevation with *SF*. No seepage erosion undercutting, *SE*, was considered.

Raising the water table from 75% of *BH* to 100% of *BH* decreased the *FS* by 57% as opposed to only 29% when the *SF* was not considered. On the other hand, the rest of the water depths showed less decrease in the *FS* when the *SF* was considered. The reason was the stabilizing effect of SF_n for γ greater than β.

Although the water table was below the failure plane (i.e., *H* = 0% of *BH*, 25% of *BH*, and 50% of *BH*) in some simulations, the *FS* decreased. With the water table positioned below the failure plane, the horizontal-gradient was negligible but the vertical-gradient increased, indicating some vertical flow through the failure mass. This vertical flow was water draining from the top soil due to the conductive layer underneath. Neglecting the effects of the downward drainage in the topsoil resulted in an over estimation of the *FS* by 30 to 50%.

4.4.2 Stability with Seepage Erosion Undercutting

The maximum velocity in the seepage layer at the bank face was simulated using SEEP/W and the hydraulic gradient was computed. The time step chosen for flow the simulation varied with the water table depth. The most convenient time step intervals were 60 s, 30 s, and 15 s at *WT* = 100%, 75%, and 50% of *BH*, respectively. These time steps were able to capture the gradual evolution of seepage erosion in time. A perched water table developed when the head, *H*, imposed at the left side of the domain reached the top of the CL layer. For this reason, E_{rs} was computed only for *H* = 50%, 75% and 100% of *BH*.

Seepage erosion was observed to initiate (i.e., *i* greater than i_{cr}) when *v* was approximately 3.0×10^{-5} m/s with the initiation time inversely proportional to *H*. The dimensions of the seepage undercut were computed every time step using the sediment

transport function developed by Chu-Agor et al. (2009). However, the applicability of the sediment transport function was limited to approximately d_u = 10 cm. Therefore, bank stability analyses with seepage erosion were limited to this maximum undercut dimension. The *FS* calculations were reported for only d_u = 5 cm, the depth at the middle of the allowed range, and d_u = 10 cm, the maximum depth allowed by the sediment transport function.

The coordinates defining the bank face of the LS layer in BSTEM were modified in order to account for the undercut dimensions before the *FS* was computed. It was found that the *FS* decreased by approximately 6% for d_u = 5 cm and 11% for d_u = 10 cm (Figure 4.6) due to the removal of supporting material in the LS layer. The decrease in the *FS* may seem small but it should be recalled that the bank profile was 3.0 m tall. The larger d_u was relative to the bank height, the higher the decrease in the *FS*. In fact, Chu-Agor et al. (2008b) reported a decrease in *FS* for a d_u = 5 cm (6.25% of *BH*) in their experiments of approximately 39%. A d_u = *10* cm (12.5% of *BH*) in their experiments was reported to decrease *FS* by around 63%. The decrease in the *FS* due to the rise in the water table depth when the undercut was in place remained unchanged.

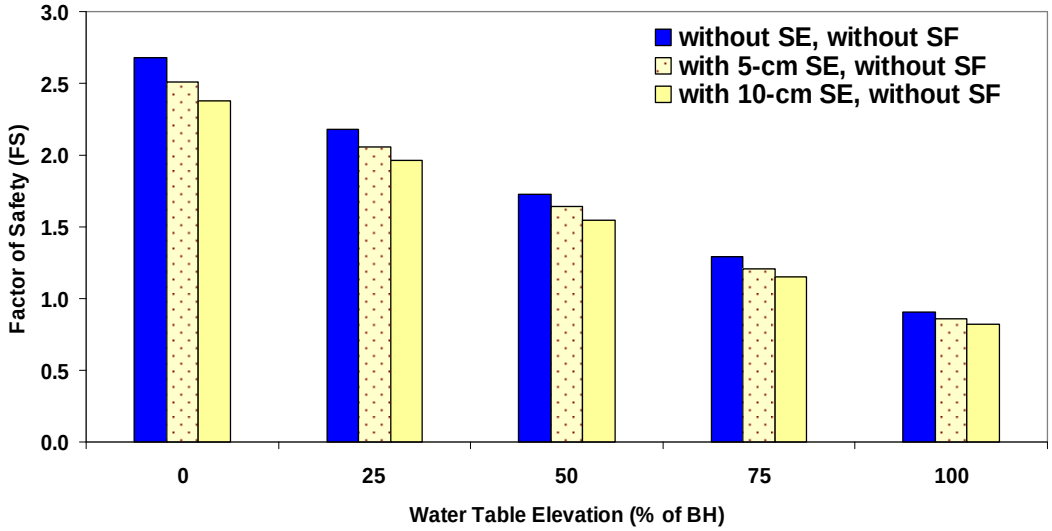

Figure 4.6 Factor of safety, *FS*, due to seepage erosion, *SE*. The presence of the seepage undercut did not affect the decrease in *FS* due to the rise of the water table elevation. No seepage force, *SF*, was considered

4.4.3 Stability with seepage erosion and seepage force

The combined effects of *SE* and *SF* reduced the *FS* from 33 to 40% and approached 63% when the WT reached 100% of *BH* (Figure 4.7). In this study, the *SF* was the more important seepage failure mechanism. Its contribution was more than twice that of *SE* and the rise in groundwater table elevation when the *WT* reached 100% of *BH*. This was expected because of the thick layer of top soil above the conductive layer along the failure plane. This resulted in a large volume of soil on which the *SF* was acting. A d_u of approximately 6% of *BH* (i.e., 18 cm) for the LTC bank was sufficient for *SE* to become a more important failure mechanism than the combined *SF* and increased groundwater table elevation.

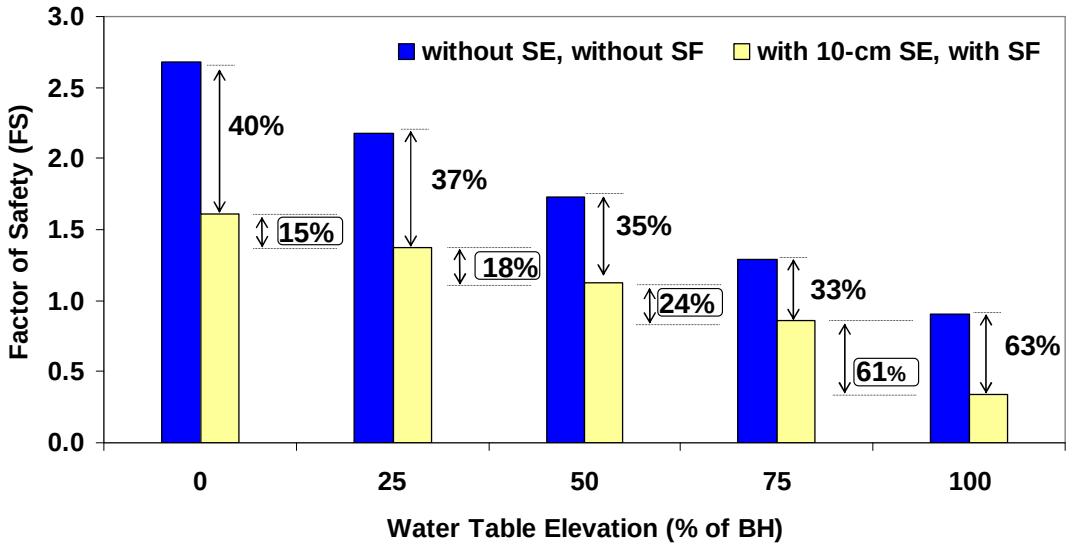

Figure 4.7 Factor of safety, *FS*, due to seepage erosion, *SE* and seepage force *SF*. Percentages inside the rectangle are the decrease in *FS* due to the rise in the water table elevation with both *SE* and *SF*.

4.5 SUMMARY AND CONCLUSION

This study incorporated the effects of seepage into BSTEM and evaluated the importance of this phenomenon on bank stability. Groundwater effects in BSTEM were simulated using a user defined groundwater table depth. The effects of the seepage force were incorporated into BSTEM by modifying the force balance. Seepage erosion undercutting was simulated using the sediment transport function developed by Chu-Agor et al. (2009). The function computed the dimensions of the seepage erosion undercut in time, which were then used to modify the bank profile in BSTEM. Stability of a streambank along Little Topashaw Creek was evaluated under different scenarios: (1) without seepage forces and undercutting, (2) with seepage forces only, (3) with seepage undercutting only, and (4) with both seepage force and undercutting. For a condition where the bank is totally saturated, the *FS* can decrease by as much as 66%

from that of a dry condition due to the decrease in the frictional strength of the soil as the pore-water pressure increased. Incorporating the effects of the seepage force resulted in an average decrease in *FS* of approximately 30 to 50% for all water table depths. Seepage erosion undercutting reduced the *FS* by approximately 6% for a 5 cm undercut (i.e., 2% of *BH*) and 11% for a 10 cm undercut (i.e., 3.3% of *BH*) due to the loss in supporting material in the conductive layer. Seepage erosion undercutting required 15 to 20 cm of seepage undercut to become the dominant failure mechanism over seepage forces and pore-water pressure effects. The cumulative effects of seepage reduced this streambank's *FS* by up to 63% when the WT reached the entire bank height. Seepage effects were significant to warrant the development of a model capable of simulating seepage processes. Such a model provides the capability to perform more comprehensive bank stability analyses to better understand site-specific failure mechanisms.

CHAPTER 5

Summary and Conclusion of Dissertation

The overall objectives of this research were to better understand the mechanisms of bank erosion and failure by ground water seepage and to incorporate seepage processes (i.e., seepage erosion undercutting and seepage forces) into bank stability analyses. Seepage processes (i.e., seepage forces and seepage erosion) were not being considered when evaluating the stability of streambanks either for design or investigation purposes. This was due to the complexity of measuring seepage in the field, simulating the processes in the laboratory, and in understanding the failure mechanisms due to seepage. This study showed that streambanks subjected to seepage processes could fail without manifesting prior visible warning when soil strength was exceeded by the combined effects of gravity and seepage forces. Furthermore, streambanks with contrasting soil types and layering under high infiltration may result in soil mobilization and undercutting at the point where water exfiltrates the bank. As the undercut becomes bigger, the bank could fail due to the loss in supporting material. The rate at which seepage erosion occurred (i.e., the eroded mass per time) was predicted in this study using the hydraulic gradient and effective cohesion. The shape of the seepage undercut was represented by a known three-dimensional function which was used to translate the eroded volume into dimensions. The dimensions of the seepage undercut were then used to define the bank profile in a bank stability model. This study demonstrated that seepage processes were important streambank failure mechanisms and in some cases can be more

important than the effects of groundwater level. Neglecting these processes in bank stability analyses can result in overestimating the stability of streambanks by as much as 50 to 60%.

5.1 SPECIFIC CONCLUSIONS IN REGARD TO EACH DISSERTATION CHAPTER

The study was divided into four independent but interrelated sections. Specific conclusions for each section are discussed in the following sections. The first part demonstrated a procedure for incorporating seepage particle mobilization and undercutting into bank stability models using data from two-dimensional soil lysimeter experiments of layered streambanks. Seepage erosion undercutting was simulated by manually changing the geometry of the seeping layer based on the measured dimensions and timing of the undercutting. Changes in soil-water pressure were simulated using SEEP/W, a variably saturated numerical flow model, while bank stability was analyzed using SLOPE/W based on limit equilibrium. The mean factor of safety, *Fs*, was used as an index of bank stability for all experiments. The following results were obtained:

- Changes in pore-water pressure did not sufficiently contribute to bank instability.
- The loss of supporting material brought about by seepage particle mobilization and undercutting decreased the mean *Fs* in the range of 42 to 91% depending on the initial stability of the bank.
- Regardless of the initial stability of the bank, instability converged as undercutting progressed. This means that a stable bank can quickly become unstable when seepage undercutting is considered.

- For stable banks, the probability of failure reached 100% when the depth of the undercutting reached approximately 30 to 50 mm for these experimental conditions.
- Bank height and bank slope controlled the initial stability of the bank while the established constant head controlled the depth of undercutting and the mean *Fs* as undercutting progressed.
- Based on the results of the lysimeter experiments, the mean *Fs* is exponentially related to the depth of undercutting.

The second part of this study investigated the mechanisms of bank failure due to seepage using three-dimensional soil block experiments. The three-dimensional soil block two compartments, a water reservoir with a focused water inlet at the bottom and a soil compartment which simulated a single layered streambank with varying bank angles. Two different soil textures were used for these experiments: sand and loamy sand. Each soil type was packed in the box at various bulk densities and three different hydraulic heads were maintained in the water reservoir. Water was allowed to flow from the inflow reservoir to the bank face until failure occurred. Changes in the bank face during the experiment were monitored using a three-dimensional digital laser scanner. The following results were obtained:

- Bank failure mechanisms due to seepage manifested as: (1) tension or “pop-out” failure when the seepage forces are greater than the soil resistance as well as reduced shear strength from increased soil pore-water pressure, and (2) particle mobilization (i.e., entrainment in seepage flow) and bank undercutting when the seepage force gradient was less than the resisting force of the soil block with

eventual bank collapse due to the combined forces from seepage undercutting, seepage forces, and the buildup of pore-water pressure.

- Within a specific soil type, the occurrence of these mechanisms was controlled by the soil's bulk density, which directly influenced the hydraulic conductivity, effective cohesion, internal angle of friction, and critical shear stress.
- Seepage erosion undercutting initiated as either unimodal (i.e., a focused undercut at one place) or multimodal headcuts. The slope of the bank predominately influenced the undercutting formation. Eventually, multimodal undercuts converged into unimodal undercuta sometime before bank failure, the time of convergence being controlled largely by the hydraulic gradient and the bulk density.
- The shape of the seepage erosion undercut can be represented by a five-parameter Gaussian function.
- The generalized relationships between the dimensions of the undercut could be used to predict the width and height of the undercut based on a priori knowledge of the depth
- A power law relationship was observed between the depth and height of the seepage undercut which is nearly the same for both soils.
- Differences in soil type were more prevalent in the relationships between amplitude and width. While the differences (i.e., on the order of cm) between soil types were statistically significant, it is hypothesized that they would not be significant from a stability perspective.

Using the data from the three-dimensional soil-block experiments, an empirical sediment transport function which accounts for soil cohesion was developed and evaluated based on the three-dimensional nature of the seepage undercut. The function was developed using two-thirds of the total number of experiments and was evaluated using the remaining one-third. The following conclusions were obtained:

- The transport function was represented by an excess gradient function wherein the rate of erosion was related (power relationship) to the difference between the flow gradient and a critical gradient.
- The flow gradient was estimated from Darcy's Law with an adjustment to take into account the distance of seepage undercutting.
- The critical gradient was related to the soil cohesion, and in this research, a logarithmic relationship was derived between the critical gradient and the effective cohesion.
- Using the Gaussian function, the relationship between the eroded volume per bank face area and d_u as well as the relationship between d_u and h_{bf} were derived.
- The sediment transport function together with the derived relationships between the dimensions of the undercut and its geometry can be used to incorporate the effects of seepage erosion undercutting into bank stability analysis with integrated groundwater flow and stability models.
- Using the seepage layer's cohesion, bulk density, and the hydraulic gradient over time as input parameters, the dimensions of the seepage erosion undercut can be predicted in time.

Finally, seepage processes (i.e., seepage erosion and seepage forces) were incorporated into BSTEM. Also, the importance of this phenomenon on bank stability along Little Topashaw Creek was evaluated under different scenarios: (1) without seepage forces and seepage erosion, (2) with seepage forces only, (3) with seepage erosion only, and (4) with both seepage forces and seepage erosion. Groundwater effects in BSTEM were simulated using a user defined groundwater table depth. The effects of the seepage force were incorporated into BSTEM by modifying the force balance. Seepage erosion undercutting was simulated using the sediment transport function developed. The function computed the dimensions of the seepage erosion undercut in time, which were then used to modify the bank profile in BSTEM. Stability was evaluated by computing the factor of safety, *FS*. The following results were obtained:

- For a condition where the bank is totally saturated, the *FS* can decrease by as much as 66% from that of a dry condition due to the decrease in the frictional strength of the soil as the pore-water pressure increased.
- Incorporating the effects of the seepage force resulted in an average decrease in *FS* of approximately 30 to 50% for all water table depths.
- Seepage erosion undercutting reduced the *FS* by approximately 6% for a 5 cm undercut (i.e., 2% of BH) and 11% for a 10 cm undercut (i.e., 3.3% of BH) due to the loss in supporting material in the conductive layer.
- Seepage erosion undercutting required 15 to 20 cm of seepage undercut to become the dominant failure mechanism over seepage forces and pore-water pressure effects.

- The cumulative effects of seepage reduced this streambank's *FS* by up to 63% when the WT reached the entire bank height.
- Seepage effects were significant to warrant the development of a model capable of simulating seepage processes in order to provide a more comprehensive bank stability analyses to better understand site-specific failure mechanisms.

5.2 FUTURE RESEARCH

Additional research advances are required, especially in understanding the link between fluvial erosion and seepage processes. Fluvial erosion is commonly modeled with excess shear stress formulations based on an erodibility coefficient. However, it is unknown how ground water forces impact soil erodibility when acted upon by multiple forces simultaneously. Also, much work remains in improving the proposed sediment transport function. Other three-dimensional functions which can represent the shape of the seepage undercut better should be investigated. The limitation in the range of the applicability of the function is a very important constraint since with taller banks the allowed undercut may underestimate the impact of seepage erosion on stability. It is recommended therefore to conduct more experiments using larger streambank prototypes of different bank height in order to widen the range of applicability of the function. This study showed the importance of cohesion in the erodibilty of particles. However, it was assumed that cohesion did not change during the experiment. Since seepage can change the structure (i.e., the orientation and distribution of particles and contact forces) of the soil, cohesion can also change during flow as soil particles are rearranged, deposited, and experience stress. A study that will evaluate the effect of seepage on cohesion is also recommended.

CHAPTER 6

References

Abam, T.K.S. (1993). Factors affecting distribution of instability of river banks in the Niger delta. *Eng. Geo*, 35, 123-133.

ASCE Task Committee on Hydraulics, Bank Mechanics, and Modeling of River Width Adjustment. 1998. River width adjustment. I: Processes and mechanisms. *J. Hydraul. Eng-ASCE* 124(9), 881-902.

Bradford, J.M., and R.F. Piest. 1977. Gully wall stability in loess derived alluvium. *Soil Sci. Soc. Am. J.* 41(1), 115-122.

Bryan, R.B., and J.A.A. Jones. 1997. The significance of soil piping processes: inventory and prospect. *Geomorphology*, 20, 209-218.

Budhu, M., and R. Gobin. 1996. Slope instability from groundwater seepage. *J. Hydraul. Eng- ASCE* 122, 415-417.

Burgi, P.H., and S. Karaki. 1971. Seepage effect on channel bank stability. *J. Irrig. Drain. E-ASCE* 97, 59-72.

Cancienne, R., G.A. Fox, A. Simon. 2008. Influence of seepage undercutting on the root reinforcement of streambanks. *Earth Surf. Proc. Land*. (11), 1769-1787.

Caviness, K., G.A. Fox, and P.N. Deliman. 2006. Modeling the Big Black River: Comparison of water quality models. *J. Am. Water Resour. As.* 42(3), 617-627.

Chu-Agor, M.L., G.A. Fox, R. Cancienne, G.V. Wilson. 2008a. Seepage caused tension failures and erosion undercutting of hillslopes. *J. Hydrol*. 359, 247-259.

Chu-Agor, M.L. , G.A. Fox, and G.V. Wilson. 2009. Sediment transport function predicting seepage erosion undercutting for bank failure prediction. *J. Hydrol*. (In Review).

Chu-Agor, M.L., G.V. Wilson, and G.A. Fox. 2008b. Numerical modeling of bank stability by seepage erosion. *J. Hydrol. Eng.*13 (12), 1133-1145.

Crosta, G., and C. di Prisco. 1999. On slope instability induced by seepage erosion. *Can. J. Geotech.*, 36, 1056-1073.Dapporto, S., M. Rinaldi, N. Casagli, and P. Vannoci. 2003. Mechanisms of riverbank failure along the Arno River, Central Italy. *Earth Surf. Proc. Land.* 28, 1303-1323.

Darby, S.E., D. Gessler, and C.R. Thorne. 2000. Computer program for stability of steep cohesive riverbanks. *Earth Surf. Proc. Land.* 25, 175-190.

Darby, S.E., and C.R. Thorne 1996. Numerical simulation of widening and bed deformation of straight sand-bed rivers. I. Model development. *J. Hydraul. Eng-ASCE*, 122, 184-193.

Duncan, J.M., and S.G. Wright. 1980. The accuracy of equilibrium methods of slope stability analysis. *Eng. Geol.* 16, 5-17.

Dunne, T., 1990. Hydrology, mechanics, and geomorphic implications of erosion by subsurface flow, *Geol. Soc. Am. Bull*., Special Paper 252.

Edil, T.B., and L.E. Vallejo. 1980. Mechanics of coastal landslides and the influence of slope parameters. *Eng. Geol.* 16, 83-96.

Evans, D.J., C.E. Gibson, and R.S. Rossell. 2006. Sediment loads and sources in heavily modified Irish catchments: A move towards informed management strategies. *Geomorphology*, 79(1-2), 93-113.

Faulkner, H., 2006. Piping hazard on collapsible and dispersive soils in Europe. In: Soil Erosion in Europe. J. Boardman and J. Poesen (eds.), John Wiley and Sons, Inc.: West Sussex, England.

Fredlund, D.G., and H. Rahardjo. 1993. Soil mechanics for unsaturated soils. John Wiley and Sons, New York.

Fox, G.A., M.L. Chu-Agor, and G.V. Wilson. 2007b. Erosion of noncohesive sediment by groundwater seepage flow: Experiments and numerical modeling. *Soil Sci. Soc. Am. J.* 71(6), 1822-1830.

Fox, G.A., G.V. Wilson, R.K. Periketi, and R.F. Cullum. 2006. Sediment transport model for seepage erosion of streambank sediment. *J. Hydrol. Eng.* 11(6), 603-611.

Fox, G.A., G.V Wilson, A. Simon, E. Langendoen, O. Akay, and J.W. Fuchs. 2007a. Measuring streambank erosion due to ground water seepage: Correlation to bank pore water pressure, precipitation, and stream stage. *Earth Surf. Proc. Land.* 32(10), 1558-1573.

Hardy, R.J. 2006. Fluvial geomorphology. *Prog. Phys. Geog.* 30(4), 553-567.

Hagerty, D.J., M.F. Spoor, and C.R. Ullrich. 1981. Bank failure and erosion on the Ohio River. *Eng. Geol.* 17, 141-158.

Hagerty, D.J. 1991. Piping/sapping erosion. 1. Basic considerations. *J. Hydraul. Eng-ASCE.* 117(8), 991-1008.

Hooke, J.M. 1979. An analysis of the processes of river bank erosion. *J. Hydrol*. 42, 39-62.

Hinds, M.A., and G.A. Milliken. 1987. Statistical methods for using nonlinear models to compare silage treatments. *Biometrical J.* 29(7), 825-834.

Howard, A.D., and C.F McLane III. 1988. Erosion of cohesionless sediment by ground water seepage. *Water Resour. Res.* 24 (10), 1659-1674.

Huang, C., and J.M. Laflen. 1996. Seepage and soil erosion for a clay loam soil. *Soil Sci. Soc. Am. J.* 60(2), 408-416.

Krahn, J. 2004a. Seepage modeling with SEEP/W: An engineering methodology. GEO-SLOPE International Ltd. Calgary, Alberta, Canada.

Krahn, J. 2004b. Stability modeling with SLOPE/W: An engineering methodology. GEO-SLOPE/W International Ltd. Calgary, Alberta, Canada.

Kusabe, O., Y. Okumura, and A. Nakase. 1987. Centrifuge modeling of river bank failures. *Proceedings of International Symposium on Flood Frequency and Risk Analysis*, 399-408.

Lawler, D. 2005. The importance of high-resolution monitoring in erosion and deposition dynamics studies: examples from estuarine and fluvial systems. *Geomorphology,* 64, 1-23.

Lindow, N. 2007. Channel Evolution of a Restored Low Gradient, Sand Bed Stream. Ph.D. Dissertation, North Carolina State University, Raleigh, NC.

Lobkovsky, A.E., B. Jensen, A. Kudrolli., and D.H Rothman. 2004. Threshold phenomena in erosion driven by subsurface flow. *J. Geophys. Res.* 109(F4), Art. No. F04010.

Lourenco, S.D.N., K, Sassa, and H. Fukuoka. 2006. Failure process and hydrologic response of a two layer physical model: Implications for rainfall-induced landslides. *Geomorphology*, 73, 115-130.

McWhorter, D.B., and D.K. Sunada. 1977. Ground-Water Hydrology and Hydraulics. Water Resources Publications, Highland Park, Colorado.

Morgenstern, N.R., and V.E. Price. 1965. The analysis of the stability of general slip surfaces. *Geotechnique*, 15, 79-93.

Owoputi, L.O., and W.J. Stolte. 2001. The role of seepage in erodibility. *Hydrol. Process.* 15(1), 13-22.

Periketi, R. (2005). Analysis of Seepage Erosion with Lysimeter Experiments and Numerical Modeling. M.S. Thesis, Department of Civil Engineering, University of Mississippi, University, MS.

Reddi, L. N. 2003. Seepage in Soils. Hoboken, New Jersey: John Wiley and Sons, Inc.

Rinaldi M., and N. Casagli. 1999. Stability of streambanks formed in partially saturated soils and effects of negative pore water pressures: The Siene River (Italy). *Geomorphology*, 26, 253-277.

Rinaldi, M, N. Casagli, S. Dapporto, and A Gargini. 2003. Monitoring and modeling of pore water pressure changes and riverbank stability during flow events. *Earth Surf. Proc. Land.* 29, 237-254.

Rockwell, D.L. 2002. The influence of groundwater on surface flow erosion processes. *Earth Surf. Proc. Land.* 27(5), 495-514.

Simon A., and S.E. Darby. 1997. Disturbance, channel evolution and erosion rates: Hotophia creek, Mississippi. *Proceedings: Conference on Management of Landscapes Disturbed by Channel Incision.* Wang SSY, Langendoen EJ, and Shields FD (eds.), ISBN 0-937099-05-8, 476-481.

Simon A., A. Curini, S.E. Darby, and E.J. Langendoen. 1999. Streambank mechanics and the role of bank and near-bank processes in incised channels. In *Incised River Channels*, Darby SE, Simon A (Eds), John Wiley and Sons, Chichester, UK, pp. 193-217.

Sidorchuk, A., 2005. Stochastic modeling of erosion and deposition in cohesive soils. *Hydrol. Process*. 19, 1399-1417.

Sultan N., P. Cochonat, M. Canals, A. Cattaneo, B. Dennielou, H. Haflidason, J.S. Laberg, D. Long, J. Mienert, F. Trincardi, R. Urgeles, T.O. Vorren, and C. Wilson. 2004. Triggering mechanisms of slope instability processes and sediment failures on continental margins: a geotechnical approach. *Mar. Geol.* 213, 291-321.

van Genuchten, M.T. 1980. A closed-form equation for predicting the hydraulic conductivity of unsaturated soils. *Soil Sci. Soc. Am. J.*, 44(5), 892-898.

Weisstein, E.W. 1999. Gaussian function. In: CRC Concise Encyclopedia of Mathematics. CRC Press, New York, pp. 716-717.

Whitlow, R., 1983. Basic Soil Mechanics. Construction Press, New York.

Wilson G.V., R.K. Periketi, G.A. Fox, S.M. Dabney, F.D. Shields, and R.F. Cullum. 2007. Seepage erosion properties contributing to streambank failure. *Earth Surf. Proc. Land.* 32(3), 447-459.

VITA

Ma. Librada Chu-Agor

Candidate for the Degree of

Doctor of Philosophy

Dissertation: INCORPORATING SEEPAGE PROCESSES INTO BANK STABILITY ANALYSES

Major Field: Biosystems Engineering

Biographical:

Personal Data:
Phone: (405)762-0904
e-mail: malibradachu@yahoo.com

Education:
Completed the requirements for the degree of Doctor of Philosophy in Biosystems Engineering at Oklahoma State University, Stillwater, Oklahoma in July, 2009.

Completed the requirements for the degree of Master of Science in Hydrology and Water Resources at UNESCO-IHE, Delft, The Netherlands in February, 2003.

Completed the requirements for the degree of Master of Arts in College Teaching (major in Civil Engineering) at University of Mindanao, Davao City, Philippines in October, 1996.

Completed the requirements for the degree of Bachelor of Science in Civil Engineering at Western Institute of Technology, Iloilo City, Philippines in March, 1989.

Professional Memberships: American Society of Agricultural and Biological Engineers (ASABE)

Name: Ma. Librada Chu-Agor Date of Degree: July, 2009

Institution: Oklahoma State University Location: OKC or Stillwater, Oklahoma

Title of Study: INCORPORATING SEEPAGE PROCESSES INTO BANK STABILITY ANALYSES

Pages in Study: 130 Candidate for the Degree of Doctor of Philosophy

Major Field: Biosystems Engineering

Scope and Method of Study: The overall objectives of this research were to better understand the mechanisms of bank erosion and failure by ground water seepage and to incorporate seepage processes (i.e., seepage erosion undercutting and seepage forces) into bank stability analyses. Seepage processes (i.e., seepage forces and seepage erosion) were not being considered when evaluating the stability of streambanks either for design or investigation purposes. This was due to the complexity of measuring seepage in the field, simulating the processes in the laboratory, and in understanding the failure mechanisms due to seepage. The study was divided into four independent but interrelated sections consisting of laboratory experiments simulating seepage as well as numerical modeling.

Findings and Conclusions: This study showed that streambanks subjected to seepage processes could fail without manifesting prior visible warning when soil strength was exceeded by the combined effects of gravity and seepage forces. Furthermore, streambanks with contrasting soil types and layering under high infiltration may result in soil mobilization and undercutting at the point where water exfiltrates the bank. As the undercut becomes bigger, the bank could fail due to the loss in supporting material. The rate at which seepage erosion occurred (i.e., the eroded mass per time) was predicted in this study using the hydraulic gradient and effective cohesion. The shape of the seepage undercut was represented by a known three-dimensional function which was used to translate the eroded volume into dimensions. The dimensions of the seepage undercut were then used to define the bank profile in a bank stability model. This study demonstrated that seepage processes were important streambank failure mechanisms and in some cases can be more important than the effects of groundwater level. Neglecting these processes in bank stability analyses can result in overestimating the stability of streambanks by as much as 50 to 60%.

ADVISER'S APPROVAL: Dr. Garey A. Fox